THE UNIVERSITY *of* EDINBURGH

Angular analysis of the decay $B^0 \to \phi K^*(892)^0$

Dean Lambert

A thesis submitted in fulfilment of the requirements
for the degree of Doctor of Philosophy
to the
University of Edinburgh
2014

Abstract

The LHCb experiment is a single-arm forward spectrometer situated at the Large Hadron Collider, CERN. LHCb is optimised for the precision study of beauty and charm flavoured hadrons and in 2011 collected $1\,\text{fb}^{-1}$ of proton-proton collision data at a centre-of-mass energy of 7 TeV. The aim of LHCb is to search for rare decays and make precise measurements of Charge-Parity (CP) violation in the beauty and charm sectors. In the Standard Model the decay $B^0 \to \phi K^*(892)^0$ is described by a loop mediated process, providing a sensitive test for new physics. In this decay, signs of CP violation could indicate the presence of physics beyond the Standard Model. This thesis presents a study of the flavour eigenstate $B^0 \to \phi(\to K^+K^-)K^*(892)^0(\to K^+\pi^-)$ and its charge conjugate $\overline{B}^0$-decay. The decay products form an admixture of CP-even and CP-odd eigenstates, which can have longitudinal or transverse polarisation. An angular analysis is performed to disentangle these different contributions and the polarisation amplitudes and strong phases are measured. No difference is observed between B^0 and $\overline{B}^0$ amplitudes, supporting the hypothesis that CP is conserved in this decay. In addition, the Triple Product Asymmetries (TPAs) are determined from the products of the polarisation amplitudes and strong phases. *True* TPAs are zero in the event that CP symmetry is conserved, while *fake* TPAs can arise due to final-state interactions. Although the measured true TPAs are consistent with zero, several significant fake TPAs are observed.

Lay abstract

For the Universe to appear as it does today, a process which favours matter over antimatter must exist. This process is called *CP* violation and is well described by current theory. Previous experiments have confirmed the existence of *CP* violation, although not in the amounts expected in the early Universe. LHCb is an experiment at the Large Hadron Collider which is specifically designed to search for new sources of *CP* violation. This thesis describes an analysis of the decay $B^0 \to \phi K^*(892)^0$. Observation of *CP* violation in this decay would be in contradiction to current predictions and would need to be described by new physics models. The results show no evidence of *CP* violation in this decay, supporting current theoretical predictions.

Declaration

Except where otherwise stated, the research undertaken in this thesis was the unaided work of the author. Where the work was done in collaboration with others, a significant contribution was made by the author.

D. Lambert
March 2015

Acknowledgements

I would like to thank the members of the Edinburgh PPE group for such an intellectually stimulating and rewarding four years. It has been a pleasure working with everyone. I would like to thank my supervisor Steve Playfer for guiding me through my studies and for his invaluable physics insight. A special thanks must be made to Matt Needham for always being available to help with my analysis, despite how busy he is. Greig Cowan and Pete Clarke have also contributed hugely to my analysis and I extend my thanks to them. Working with Stephan Eisenhardt and Thierry Gys in my first few years was memorable and rewarding and I thank them for making it so. A massive 'thank you' also goes to the PPE students who easily rival the best textbooks with their collective knowledge. Rob Currie deserves a special mention for answering all of my RapidFit related questions over the years and is owed many beers in return. For the last year of my PhD much of my work was done in collaboration with Antonio Romero Vidal, in particular he did much of the work presented here on the direct *CP* asymmetry. I thank him for an enjoyable and successful collaboration and for answering my many questions. To my parents, I am eternally grateful for your love and unquestioning support and I dedicate this work to you. Lastly, thank you to my partner Laura, for your patience and understanding, your love and your compassion, your support and your kindness. It means everything to me.

Contents

List of Figures

List of Tables

Chapter 1

Introduction

1.1 Motivation

Around 14 billion years ago the Universe spontaneously came into existence in the process known as the Big Bang [1]. All of the energy in the Universe was created at this point; ordinary matter, dark matter and dark energy, which exist in approximately the ratio 1:5:14 [2]. Everything we see today, from the furthest stars to life on Earth, is a remnant of this distant process.

In the time it takes to read these opening sentences, the Universe changed from being a hot quark-gluon plasma to being cool enough for the first protons and neutrons to form [3]. After a few minutes these combined with electrons to form the first hydrogen atoms. Later, in a process known as *primordial nucleosynthesis*, other light elements such as helium were formed. Interestingly, at this stage there is a distinct lack of antinuclei.

It is assumed that at the beginning of the Universe an equal number of quarks and antiquarks were created. As the Universe cooled new quark-antiquark pairs stopped being produced and those remaining annihilated with each other. Surprisingly, more quarks than antiquarks remained. Although the process by which this asymmetry formed, known as *baryogenesis*, is not understood, it is the first in a series of requirements for matter and antimatter to be produced at different rates. These are known as the 'Sakharov conditions' [4]:

- A baryon number violating interaction must exist (baryogenesis).
- Charge (C) and Charge-Parity (CP) violating interactions exist.

- These interactions must occur out of thermal equilibrium.

The first of these is clearly needed to produce more particles than antiparticles. The second condition ensures that a process which produces more particles than antiparticles is not compensated by a process which produces more antiparticles than particles; the *CP* operator is discussed in detail in Section 1.4. Lastly, the process must occur out of thermal equilibrium since any reaction $X \to Y + B$, where X and Y have baryon number zero and B has a baryon number greater than zero, would be compensated by the inverse reaction $Y + B \to X$. These processes would otherwise have identical rates resulting in no net baryon asymmetry.

Antimatter was proposed in 1931 as an explanation for the negative energy solution of the Dirac equation [5, 6]. The first antiparticle, the antielectron or *positron*, was discovered by Anderson soon after in 1933 [7].

It took more than thirty years from the discovery of the positron until the first observation of a *CP*-violating reaction [8]. Since this discovery more *CP* violation has been uncovered, though not in the amounts expected in the early Universe. The amount of *CP* violation in the Standard Model (see Sec. 1.2) is $\approx 10^{10}$ times too small to explain the current baryon to photon ratio of the Universe [9]. Therefore, additional sources of *CP* violation are sought which will provide a greater insight into the first moments of the Universe.

The remainder of this Chapter will discuss the fundamental forces of particle physics and *CP* violation. Chapter 2 describes the LHCb detector, which was specifically designed to explore sources of *CP* violation. Chapter 3 motivates the study of the decay $B^0 \to \phi K^*(892)^0$ and Chapter 4 describes the analysis procedure for this decay at LHCb. The results of this analysis, using data collected by LHCb in 2011, are discussed in Chapter 5. The final chapter will present a study of the expected sensitivity LHCb can achieve with a dataset approximately three times as large as the one collected in 2011.

1.2 The Standard Model

Even in ancient times it was proposed that all matter was constructed from some basic unit too small to be observed by the naked eye. This was named the atom: meaning "uncuttable" or "indivisible". Experimental evidence for the atom came in the 19$^{\text{th}}$ century with the observation of Brownian motion and development of

the periodic table.

It was, however, not until the tail end of the 19$^{\text{th}}$ century – with the discovery of the electron by J.J. Thomson – that the field of particle physics started to take shape. An entire zoo of particles was discovered over the next century, along with the laws governing their interactions. These laws would go on to become what is now known as the *Standard Model* of particle physics. The Standard Model describes the strong, weak and electromagnetic forces and is one of the most successful scientific theories of the 20$^{\text{th}}$ century. The Standard Model is a significant step towards a unified theory, which attempts to unite the forces described by the Standard Model with gravity.

1.2.1 Particle content of the Standard Model

The particles of the Standard Model can be split into matter particles and force carrying particles. The former are spin-$\frac{1}{2}$ fermions and the latter are integer spin bosons. Figure 1.1 shows the particles of the Standard Model with information on their masses, spin and electric charge.

There are 12 fermions in total, or 24 if antiparticles are included, which can be subdivided into quarks and leptons. Quarks and leptons differ in several fundamental ways. Quarks carry colour charge (see Sec. 1.2.3) while leptons do not. Quarks have electric charge $2/3$ or $-1/3$, while leptons carry 0 or -1 and leptons can propagate freely but quarks are bound into hadrons.

There are two types of hadron: mesons, which are formed from quark-antiquark pairs ($q\overline{q}$), and baryons which contain three bound quarks (qqq). The antimatter version of baryons, antibaryons, are composed of three anti-quarks ($\overline{qqq}$). A quantum number B, known as baryon number, can be assigned to quarks (antiquarks) such that baryons (antibaryons) have $B = 1$ (-1) and mesons have $B = 0$.

Fermions belong to one of three generations. The first generation consists of the up quark (u), down quark (d) and electron (e) which have electric charges $2/3, -1/3$ and -1, respectively. The up and down quarks are the constituent components of the proton (uud) and neutron (udd) and together with the electron make up all observable matter in the Universe. The second generation contains the charm quark (c), strange quark (s) and muon (μ) which are heavier versions of the u-quark, d-quark and electron, respectively. The third generation contains

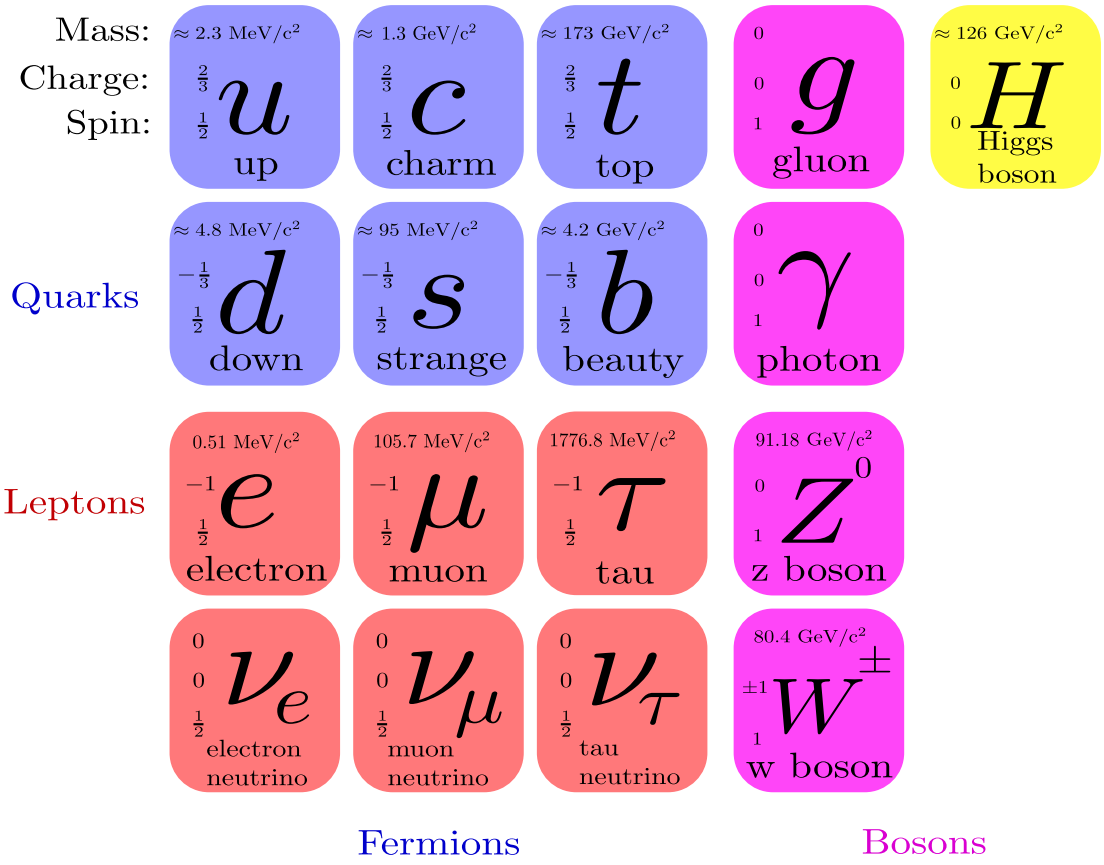

Figure 1.1: Standard Model particles with spin, electric charge and approximate mass shown. The electric charge has been normalised to the magnitude of the electron charge.

the top (t) and bottom (b) quarks together with the tau (τ) and are heavier again. Each generation also comes with a weakly interacting particle known as a neutrino which has the same flavour as the charged lepton *i.e.* ν_e, ν_μ and ν_τ. Neutrinos have zero electric charge and mass in the Standard Model[1].

With the exception of the weak interaction (see Sec. 1.2.2), the three families interact identically in the Standard Model and only vary in their masses and some quantum numbers. The Standard Model contains no theoretical reason for the number of quark generations to be the same as the number of lepton generations. Additionally, it is not known why there are three generations of quarks and leptons in the Standard Model, although measurements of the Z^0 boson width

[1]Measurements of neutrino flavour oscillation have proven that neutrinos have non-zero mass. Although the neutrino mass has not been measured directly, the mass differences can be calculated from the oscillation parameters [10].

have proven this to be the case for lepton masses below $45\,\mathrm{GeV}/c^2$ [11–13].

Four gauge bosons mediate the forces of the Standard Model and these will be discussed in the sections below. Table 1.1 shows a summary of the range, relative strength and force carriers of each fundamental force. Additionally there is one spin-0 boson which is responsible for electroweak symmetry breaking [14]. The Higgs boson is such a candidate and was recently observed by the CMS and ATLAS collaborations [15, 16]. In total the Standard Model contains 30 particles including antiparticle partners.

Force	Boson (s)	Range (m)	Relative strength
Strong	gluon	10^{-15}	1
Electromagnetic	photon	∞	10^{-2}
Weak	$W^{\pm}$ and Z^0	10^{-18}	10^{-12}
Gravity	graviton	∞	10^{-38}

Table 1.1: Relative strength, range and gauge bosons of the fundamental forces at low energy. At present the graviton is a hypothetical particle; no experimentally verified quantum theory of gravity exists.

1.2.2 Electroweak force

The electromagnetic force is propagated by the photon and felt by all particles with non-zero electric charge. As its influence is felt at the macroscopic level it is arguably the most recognisable force, being responsible for the structure of ordinary matter.

A typical electromagnetic interaction can be represented using a Feynman diagram as shown in Figure 1.2. In this diagram an electron is used as an example however this could be substituted with any charged fermion. In words this diagram says that an electron came in, emitted a photon and then continued its journey. This is the basic structure of the electromagnetic interaction and more complex interactions can be depicted by attaching several of these vertices together. Figure 1.3 shows the combination of two primitive vertices, this represents Coulomb repulsion of two like-sign charges.

Quantum Electrodynamics (QED) is the relativistic quantum field theory describing electromagnetism. It was developed during the mid 20^{th} century and

has been extremely successful. Measurements of the fine structure constant, α, agree with theoretical predictions to better than 10 parts per billion [17, 18].

Using QED it is possible to calculate the probability of interaction between particles. The cross section for some interaction $\sigma(X \rightarrow Y)$ is proportional to $|\mathcal{M}(X \rightarrow Y)|^2$ where $\mathcal{M}(X \rightarrow Y)$ is given by the product of the vertex and propagator terms as described by the Feynman rules. According to these rules each vertex contributes a factor of fermion charge Q, multiplied by the strength of the electromagnetic force $\sqrt{\alpha} = \sqrt{e^2/4\pi\epsilon_0\hbar c}$. Each photon propagator contributes $1/q^2$, where q is the four-momentum transfer.

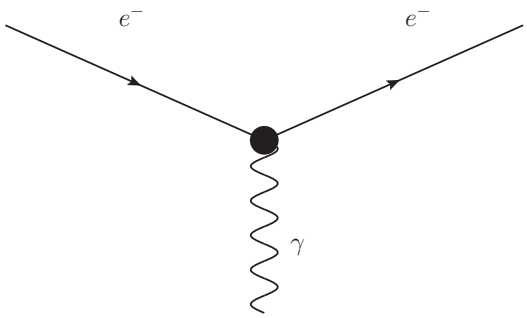

Figure 1.2: Feynman diagram showing a single photon-electron vertex. Time flows from left to right.

The Feynman rules dictate that energy and momentum must be conserved at each vertex and thus for a whole process [19]. Therefore, in the absence of an external electromagnetic field, it is clear that the interaction vertex shown in Figure 1.2 is forbidden as it violates energy conservation. Particles which violate energy and momentum conservation are called *virtual* and can only exist as internal lines on a Feynman diagram.

The amount of time a virtual particle can exist is inversely proportional to the amount of energy that it needs to 'borrow'. This is described by the Heisenberg uncertainty principle

$$\Delta E \Delta t \geq \frac{\hbar}{2} \,. \tag{1.1}$$

Since the photon is massless there is no lower limit on the amount of energy needed to create a virtual photon, as a result the range of the electromagnetic force is infinite.

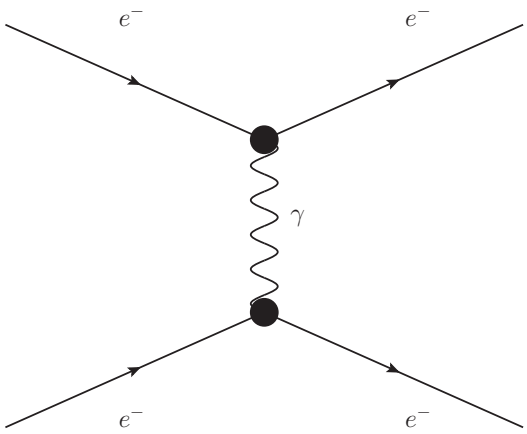

Figure 1.3: Feynman diagram showing Coulomb repulsion.

The weak interaction describes decays via $W^{\pm}$ and Z^0 bosons. The weak interaction is felt by all particles with a non-zero value of the quantum number weak isospin. This includes all particles and force carriers with the exception of the photon and gluon. Specifically, the $W^{\pm}$ couples to weak isospin while the Z^0 couples to a combination of weak isospin (T) and weak hypercharge (Y_W), where the latter is a combination of electric charge (Q) and the third component of weak isospin (T_3)

$$Y_W = 2(Q - T_3) \; . \tag{1.2}$$

The decay of the $W^{\pm}$, also known as a charged-current interaction, is unique in that it can change the flavour of quarks from an up-type to a down-type or vice-versa, as seen in Figure 1.4.

The range of the weak force can be estimated using Equation 1.1. As the mass of the $W^{\pm}$ and Z^0 bosons is large, the range of the weak force is limited to $\sim 10^{-18}$m. The masses of the gauge bosons are also responsible for the 'weakness' of the force.

The propagator term of the weak interaction is given by $1/(q^2 - M_{W,Z}^2)$ where $M_{W,Z}$ is the $W^{\pm}$ or Z^0 boson mass. For a lepton decay the vertex term is simply g_w, the weak coupling constant, which is related to the Fermi constant by

$$G_{\mathrm{F}} = \frac{\sqrt{2}}{8}\frac{g_w^2}{M_W^2} \; . \tag{1.3}$$

Consider the decay $\tau^- \to e^- \overline{\nu}_e \nu_\tau$ with matrix element

$$|\mathcal{M}(\tau^- \to e^- \overline{\nu}_e \nu_\tau)|^2 \propto g_w^2/(q^2 - M_W^2)^2 \ , \tag{1.4}$$

which at low energies is approximately $g_w^2/(M_W^4)$, where $g_w \approx 0.66$. Therefore, the weak interaction is not intrinsically weak and only appears this way due to the large masses of the $W^\pm$ and Z^0 bosons.

At low energies the electromagnetic and weak interactions appear to be quite different. However, work started in the 1960s by Weinberg, Salam and Glashow suggested that the weak and electromagnetic forces are different manifestations of a unified electroweak force. The theory states that at energies above $\sim 100\,\text{GeV}$ the electromagnetic and weak forces are symmetrically described by the $W^\pm$, W^0 and B^0 gauge bosons of the electroweak force. The $W^\pm$ and W^0 bosons couple to weak isospin with coupling strength g_W while the B^0 boson couples to weak hypercharge with coupling g'.

As a result of spontaneous symmetry breaking at the electroweak scale the W^0 and B^0 mix to form the Z^0 and photon with mixing angle θ_W, known as the Weinberg angle,

$$\begin{pmatrix} \gamma \\ Z^0 \end{pmatrix} = \begin{pmatrix} \cos\theta_W & \sin\theta_W \\ -\sin\theta_W & \cos\theta_W \end{pmatrix} \begin{pmatrix} B^0 \\ W^0 \end{pmatrix} \ . \tag{1.5}$$

The coupling strengths are related to the electromagnetic coupling strength by

$$e = g_w \sin\theta_W = g' \cos\theta_W \ , \tag{1.6}$$

and

$$g_z = \frac{e}{\sin\theta_W \cos\theta_W} \ , \tag{1.7}$$

where g_z is the neutrino neutral-current counterpart of g_w.

The electroweak theory was experimentally verified at CERN with the discovery of neutral-current interactions in 1973 [20]. This resulted in a Nobel prize for Weinberg, Salam and Glashow in 1979. The $W^\pm$ and Z^0 bosons were directly detected in 1983 by the UA1 and UA2 experiments at CERN [21,22]. For the advances in accelerator technology needed to make this discovery possible,

Carlo Rubbia and Simon van der Meer received Nobel prize awards shortly after.

The ratio of the masses of the $W^{\pm}$ and Z^0 bosons can be used to determine the Weinberg angle [19]

$$\cos\theta_W = \frac{M_W}{M_Z} \, . \tag{1.8}$$

Precise mass measurements of the $W^{\pm}$ and Z^0 bosons reveal [10]

$$\sin^2\theta_W = 0.23126 \pm 0.00005 \, . \tag{1.9}$$

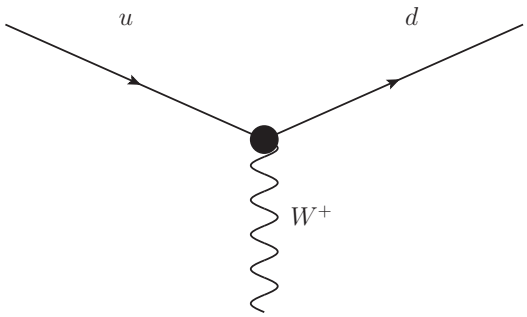

Figure 1.4: Feynman diagram showing the quark flavour-changing process $u \to W^+ d$.

1.2.3 Strong force

With the discovery that the nucleus contains a mixture of protons and neutrons came the need for a new force to describe their interaction. Clearly this new force needed to be strong enough to overcome the electromagnetic repulsion between protons but it also needed to be short range to account for its absence at the macroscopic level.

The strong force is the fundamental force responsible for both binding quarks together in hadrons and holding nucleons together in the nucleus. A simple interaction involving the strong force is shown in Figure 1.5, this is analogous to the basic QED vertex shown in Figure 1.2. A more complex diagram can be used to illustrate quarks held together in a hadron, as seen in Figure 1.6.

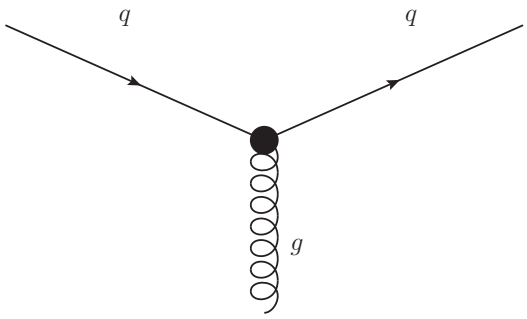

Figure 1.5: The basic vertex of the strong interaction. Usually the 'g' is not written as a curly line always represents a gluon.

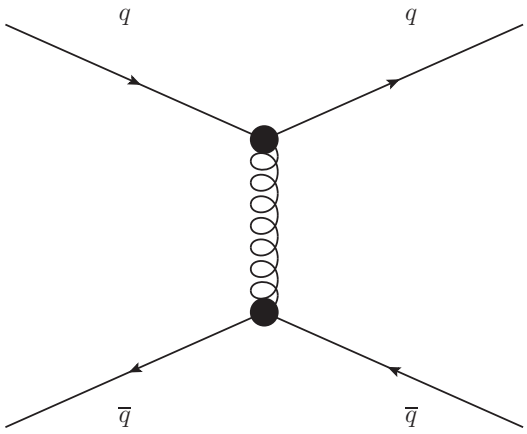

Figure 1.6: Feynman diagram showing an interaction between a quark and an antiquark mediated by a gluon.

The strong force acts on particles with colour charge. This is somewhat akin to the electric charge in QED and both are conserved quantities. There are, however, three types of colour charge rather than the single type of electrical charge. These three types are known as red, blue and green. These are simply labels and refer to the fact that the combination of a red quark, a green quark and a blue quark create a colour-neutral baryon, formally known as a colour singlet. Similarly, a colour-anticolour combination forms a colour-neutral meson. All observed particles are colour singlets. In analogy to quantum electrodynamics, the theory of the strong force is known as Quantum Chromodynamics (QCD).

Colour was originally proposed to explain certain baryons which would

otherwise be in violation of the Pauli exclusion principle. For example, the Δ^{++} baryon has quark content uuu and spin 3/2, thus requiring three identical quarks. In order to explain this observation it was postulated that each quark carry a different colour charge, creating a colour-neutral Δ^{++}. Crucially, the colour wavefunction of a baryon

$$|\Psi_C(qqq)\rangle = |\frac{1}{\sqrt{6}}[(rb - br)g + (bg - gb)r + (gr - rg)b]\rangle \ , \tag{1.10}$$

is antisymmetric under colour exchange and so obeys the Pauli exclusion principle. The corresponding wavefunction for a meson is given by

$$|\Psi_C(q\bar{q})\rangle = |\frac{1}{\sqrt{3}}(r\bar{r} + b\bar{b} + g\bar{g})\rangle \ , \tag{1.11}$$

and is colour symmetric, however for mesons the flavour wavefunction is not symmetric.

Although the gluon is massless the range of the strong force is limited to the nuclear radius. This is because hadrons have no net colour charge and so cannot couple to single gluons. Despite this, it is the strong force which keeps nucleons together in the nucleus. This is known as the nuclear force and is explained by pion exchange between nucleons. The strength of the force is described by the Yukawa potential with a short range repulsive component. Using Eqn. 1.1 the pion mass limits the range of the nuclear force to

$$r \simeq \frac{\hbar}{2M_\pi c} \simeq 1\,\text{fm} \ . \tag{1.12}$$

Despite some similarities, there are several important differences between QED and QCD. In QED the photon acts on electrically charged particles but is itself charge neutral. In QCD the gluons carry colour charge and so take part in the strong interaction, including self-interactions, as shown in Figure 1.7. Since quarks of different colours can interact, gluons must carry away the difference as seen in Figure 1.8. Gluons therefore do not carry a single colour but a colour and an anticolour.

One might naively expect that there are nine possible gluons, carrying colours $r\bar{r}$, $g\bar{g}$, $b\bar{b}$, $r\bar{g}$, $r\bar{b}$, $g\bar{r}$, $g\bar{b}$, $b\bar{r}$ and $b\bar{g}$. If this was the case it would be possible to create the superposition $(r\bar{r} + g\bar{g} + b\bar{b})/\sqrt{3}$. Which as mentioned previously, is a

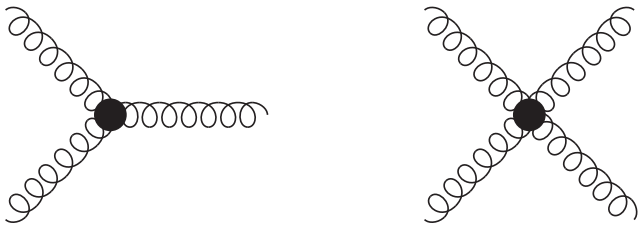

Figure 1.7: Gluon self-interaction vertices. These are possible because gluons carry colour charges.

colour singlet and thus cannot transmit the strong force. One of the combinations must therefore be removed. The remaining terms are reorganised into eight linearly independent combinations [23]

$$r\bar{b}\ , r\bar{g}\ , b\bar{g}\ , b\bar{r}\ , g\bar{r}\ , g\bar{b}\ , \frac{r\bar{r}-b\bar{b}}{\sqrt{2}}\ , \frac{r\bar{r}+b\bar{b}-2g\bar{g}}{\sqrt{6}}, \tag{1.13}$$

where the factors of $\sqrt{2}$ and $\sqrt{6}$ are simply for normalisation.

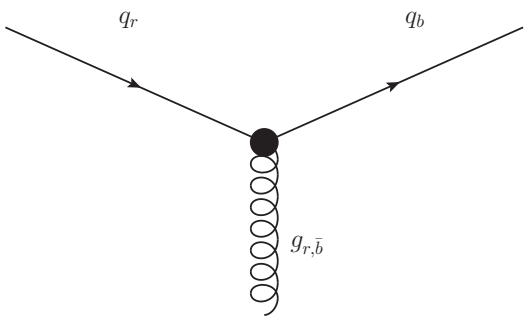

Figure 1.8: Feynman diagram showing colour conservation in the strong interaction. The quark changes colour and the gluon carries away the difference. The subscript represents colour charge.

Another major difference between QED and QCD is the strength of the strong coupling α_s, which is close to one. This is approximately two orders of magnitude greater than α, the coupling constant of the electromagnetic interaction, and initially created problems for theorists. Feynman diagrams with large numbers of vertices contributed to cross section calculations more than very basic diagrams, meaning that higher order terms could not be safely ignored. It was therefore a great relief when it was realised that the strength of α_s is dependent on the

distance between the interacting particles. Although at large distances α_s appears large, at short ranges its strength quickly diminishes. This is known as a *running coupling*. The low strength of α_s at short range means that within hadrons the quarks are not tightly bound together but are free to move around. However at distances of $\sim 1\,\text{fm}$ the strength of the force is much greater, preventing hadrons from falling apart. The quarks are said to have *asymptotic freedom*. Experimental measurements of α_s at different energies, hence different distances, are shown in Figure 1.9 and support this hypothesis.

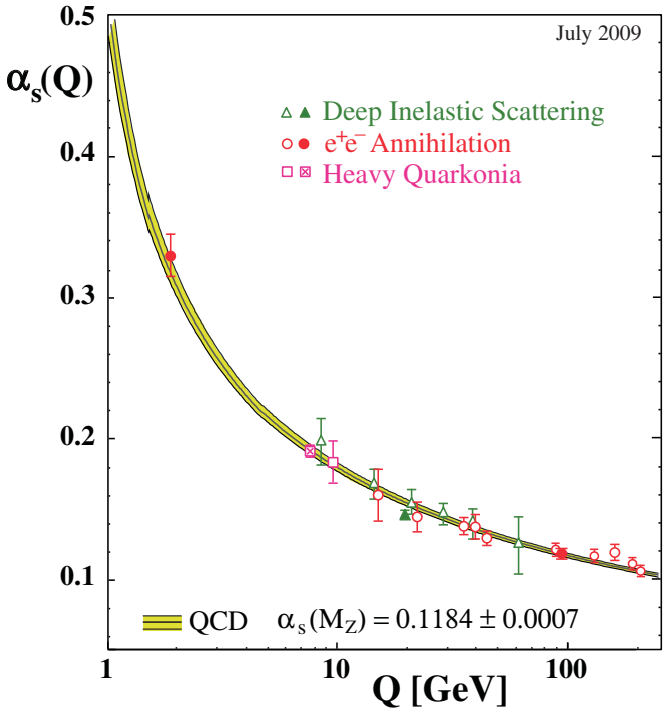

Figure 1.9: Measurements of the strong coupling constant, α_s, as a function of energy scale Q [24]. The yellow line is the predicted running of the coupling relative to the measured strength at $Q = M_Z$.

Since the quark model was postulated in the early 1960s, efforts to observe individual quarks have failed. Supporters of the theory suggested that quarks were 'confined' into hadrons, however no formal theory was constructed to explain this. Colour provides an explanation for this behaviour. It can be said that a colour field exists between quarks in close proximity to one another, this is similar to the electric field between two charged particles. As the quark separation increases the gluon self-interactions pull the colour field lines into narrow 'tubes'.

The force between the quarks therefore increases linearly with distance. It soon becomes more energetically favourable to create a new quark-antiquark pair than to increase the separation. For example, in a particle collision such as those at the LHC, large streams of long-lived particles known as jets are seen in the detector after pairs of quarks are pulled apart. Figure 1.10 shows an ATLAS event display with several jets resulting from a proton-proton collision.

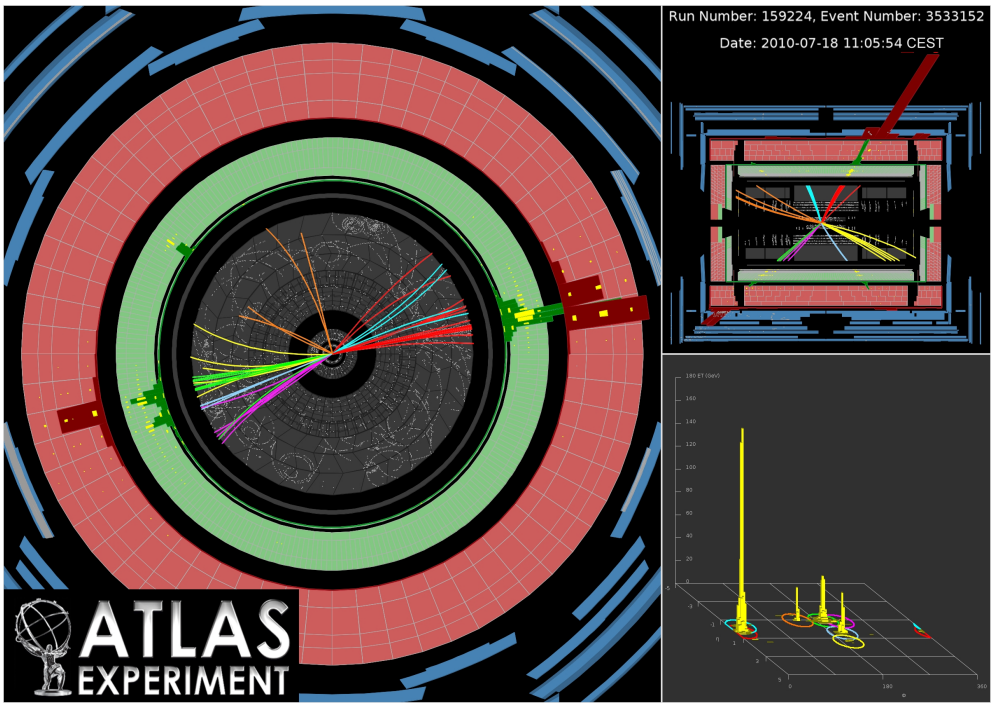

Figure 1.10: ATLAS event display showing several jets, each represented by a different colour, resulting from a 7 TeV proton-proton collision at the LHC. ATLAS Experiment © 2013 CERN.

1.3 Quark flavour mixing

During the development of weak interaction theory it was not understood why certain decays were suppressed with respect to others. When weak decays of strange quarks were observed – which had not been expected – they exhibited a suppression with respect to $u \to d$ transitions. Taking the ratio of matrix

elements between a $s \to u$ transition and a $u \to d$ transition gives

$$\frac{|\mathcal{M}(K^+ \to \mu^+\nu_\mu)|^2}{|\mathcal{M}(\pi^+ \to \mu^+\nu_\mu)|^2} \sim \frac{1}{20} \,. \tag{1.14}$$

A new approach to the theory was needed. This was provided in 1963 by Nicola Cabibbo and involved introducing a new parameter, now known as the Cabibbo angle θ_c [25].

Although the quark model was not established at the time, Cabibbo's work explained that the $W^\pm$ boson does not couple directly to the down and strange quarks but to a pair of rotated d' and s' states which are linear combinations of d and s

$$\begin{bmatrix} d' \\ s' \end{bmatrix} = \begin{bmatrix} \cos\theta_c & \sin\theta_c \\ -\sin\theta_c & \cos\theta_c \end{bmatrix} \begin{bmatrix} d \\ s \end{bmatrix} \,, \tag{1.15}$$

where d, s are the mass eigenstates and d', s' are the weak eigenstates.

Thus $u \to d$ and $s \to u$ transitions now occur with the couplings $g_w \cos\theta_c$ and $g_w \sin\theta_c$ respectively. This interpretation maintains the universal coupling, g_w, between weak eigenstates, which are rotated by θ_c from the physical mass eigenstates. This phenomenon is known as quark flavour mixing.

Cabibbo created a theory which allows quarks to change flavour within their own family ($u \to d$) and between families ($s \to u$). In doing so he provided a method to suppress decays which change strangeness, the quantum number associated with the strange quark, which were shown to occur at a lower rate experimentally.

The next major contribution to weak theory was the prediction of the charm quark by Glashow, Iliopoulos and Maiani via the GIM mechanism [26]. The charm quark is the up-type partner of the strange quark and was needed to explain the decay rate of $K^0_{\mathrm{L}} \to \mu^+\mu^-$, which was several orders of magnitude lower than expected. This new up-type quark introduces an additional Feynman diagram, as seen in Figure 1.11, which negatively interferes with the first, thus lowering the overall decay rate. The GIM mechanism also prevents flavour-changing neutral-currents at tree level, which had been ruled out experimentally [27].

Experimental discoveries again forced theory to adapt in the early 1970s. The discovery of *CP* violation in the kaon system (see Section 1.4.3) meant that

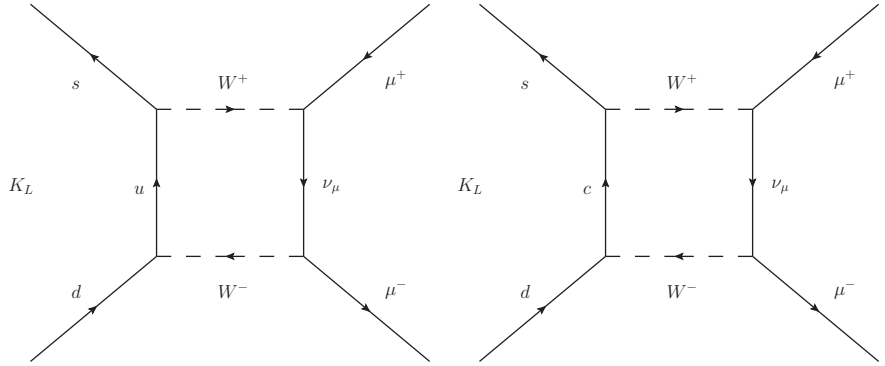

Figure 1.11: Feynman diagrams for the process $K^0_{\mathrm{L}} \rightarrow \mu^+\mu^-$. The vertex terms calculated for the diagram on the left are proportional to $\cos\theta_c \sin\theta_c$ while those given by the right diagram are proportional to $-\cos\theta_c \sin\theta_c$. These almost cancel and thus highly suppress this decay.

quark mixing could no longer be explained by a single parameter. To describe this, Kobayashi and Maskawa expanded the GIM mechanism to include two additional quark flavours and the quark mixing matrix was expanded from a 2×2 to a 3×3 matrix [28]. The resultant matrix, known as the CKM (Cabibbo-Kobayashi-Maskawa) matrix, can be defined by three angles and a single complex phase [23] and can be written

$$\begin{pmatrix} C_1 & C_3 S_1 & S_1 S_3 \\ -C_2 S_1 & C_1 C_2 C_3 - S_2 S_3 e^{i\delta} & C_1 C_2 S_3 + C_3 S_2 e^{i\delta} \\ S_1 S_2 & -C_1 C_3 S_2 - C_2 S_3 e^{i\delta} & -C_1 S_2 S_3 + C_2 C_3 e^{i\delta} \end{pmatrix} , \tag{1.16}$$

where $C_i = \cos\theta_i$ and $S_i = \sin\theta_i$ for $i = 1, 2, 3$. The CKM matrix is usually written in terms of the quark transition probabilities $|V_{ab}|$, where $g_{ab} = g_w V_{ab}$ in analogy with the Cabibbo angle. Writing Equation 1.15 for three generations gives

$$\begin{bmatrix} d' \\ s' \\ b' \end{bmatrix} = \begin{bmatrix} V_{ud} & V_{us} & V_{ub} \\ V_{cd} & V_{cs} & V_{cb} \\ V_{td} & V_{ts} & V_{tb} \end{bmatrix} \begin{bmatrix} d \\ s \\ b \end{bmatrix} . \tag{1.17}$$

In the CKM matrix, unitarity constrains the sum of quark transition probabilities for each flavour to one. This means the CKM matrix can be completely described by four parameters, as seen in Eqn. 1.16. There are three

angles, which are related to the quark transition probabilities, and one phase which allows *CP* violation in the Standard Model (see Section 1.4.3). Another notable feature is that all diagonal elements are approximately equal to one, reflecting the fact that it is much more likely for a quark to transition between members of the same family than between different families.

Following the prediction by Kobayashi and Maskawa, the bottom and top quarks were discovered in 1977 and 1995, respectively [29–31].

1.4 Charge, parity and CP operators

Symmetries play a huge role in modern physics, so much so that entire theories are based upon them. The importance of symmetries was formalised in 1918 when Emmy Noether provided a proof that symmetries of nature lead to conservation laws [32]. For example, the laws of physics can be shown to be invariant under a spatial translation, *i.e.* it does not matter where we perform an experiment. Assuming the initial conditions are identical, the outcome will be the same. This leads to the conservation of linear momentum. Similarly, the invariance of the laws of physics with respect to time leads to conservation of energy.

1.4.1 Parity

Parity symmetry (P) is the invariance of physical laws under a transformation which changes the sign of the space coordinates

$$P|\psi(\vec{x})\rangle = |\psi(-\vec{x})\rangle \ , \tag{1.18}$$

corresponding to a mirroring of each axis through the origin. For this reason parity symmetry is sometimes called mirror symmetry. The parity operation changes the handedness of a system, thus a left-handed system becomes right-handed and vice versa. In quantum physics, parity is an intrinsic property of a state and is usually written in conjunction with angular momentum as J^P.

It is reasonable to assume that the laws of physics are invariant under a parity operation. As the parity operation changes the handedness of a system and choosing either one of these is a convention, one would expect the physics to be the same in either coordinate system. This is indeed true in many cases.

Consider angular momentum

$$\vec{J} = \vec{r} \times \vec{p}\,, \tag{1.19}$$

where the position vector $\vec{r}$ and momentum vector $\vec{p}$ both change sign under parity. The net result is that angular momentum is invariant under the parity operation. It can be shown that a range of classical theories, such as Newtonian dynamics and electromagnetism, are also invariant under parity.

In the 1950s it was assumed that parity was always conserved. This had been experimentally proven in electromagnetic and strong interactions, but was unchallenged in weak decays. The so-called '$\tau - \Theta$ problem' prompted further investigation of the subject.

The τ^+ was a particle which decayed to $\pi^+\pi^0$ while the Θ^+ decayed to $\pi^+\pi^-\pi^+$. This was interesting because measurements had shown that the τ^+ and Θ^+ had the same mass and lifetime, making it highly likely they were the same particle. The 'problem' was that the final-states had opposite parity, $+1$ for $\pi^+\pi^0$ and -1 for $\pi^+\pi^-\pi^+$. This prompted theorists Yang and Lee to suggest that parity is not conserved in weak decays and that the τ^+ and Θ^+ were one and the same (now known as the K^+) [33]. A colleague of Lee, C.S. Wu, later carried out an experimental test of parity conservation in beta decays of cobalt-60 [34]. The result was clear evidence of parity violation in weak decays.

Another experiment which played an important role in the understanding of parity symmetry in the weak interaction was the measurement of neutrino helicity in 1958 [35], one year after the experiment by Wu. This pivotal measurement confirmed that all neutrinos are left-handed: they have -1 helicity. Conversely, all antineutrinos are right-handed.

Applying the parity operator to a left-handed neutrino

$$P|\nu_L\rangle = |\nu_R\rangle\ , \tag{1.20}$$

produces a right-handed neutrino, however the latter is not observed in nature. Similarly acting on an antineutrino with parity produces a left-handed antineutrino

$$P|\overline{\nu}_R\rangle = |\overline{\nu}_L\rangle\ , \tag{1.21}$$

which is also unobserved. Parity, therefore, is maximally violated in the weak sector.

1.4.2 Charge-conjugation

Charge-conjugation symmetry states that particles and antiparticles behave in the same way. The charge-conjugation operator (C) changes a particle into its antiparticle partner

$$C|e^-\rangle = |e^+\rangle. \tag{1.22}$$

Considering the example of neutrino helicity, it is easy to see that charge-conjugation symmetry is not universal and is violated in weak decays. Applying the charge-conjugation operator to a left-handed neutrino

$$C|\nu_L\rangle = |\overline{\nu}_L\rangle \ , \tag{1.23}$$

produces a particle which is not observed in nature.

In response to the $\tau - \Theta$ problem, Landau predicted that although C and P may be violated individually, the combined operation of charge-conjugation and parity (CP) is a true symmetry [36]. Extending the neutrino example, acting on a neutrino with CP

$$CP|\nu_L\rangle = |\overline{\nu}_R\rangle \ , \tag{1.24}$$

transforms a left-handed neutrino into a right-handed antineutrino. For a short while order had been restored to the weak sector.

1.4.3 CP violation

The discovery that CP symmetry was violated came only a few years after the resolution of the $\tau - \Theta$ problem; again through the study of kaon decays [8].

Two weak eigenstates exist in the neutral kaon system K^0_{L} (K-long) and K^0_{S} (K-short). These are eigenstates of the weak interaction because they have definite lifetimes, with K^0_{L} living approximately 1000 times longer than K^0_{S}. It was observed that K^0_{L} decayed mainly to three pions, whereas K^0_{S} decayed mostly

to two pions. This created the impression that $K^0_{\rm L}$ was *CP*-odd and $K^0_{\rm S}$ was *CP*-even.

An experiment by Cronin, Fitch *et al.* aimed at studying $K^0_{\rm L}$ found a small number (0.2%) which decayed to the two pion final state; this unambiguously announced that *CP* asymmetry was broken in the weak sector. Interpreting these results it can be said that although $K^0_{\rm S}$ and $K^0_{\rm L}$ are weak eigenstates they are not *CP* eigenstates. The weak eigenstates are actually superpositions of *CP* eigenstates K_1 and K_2

$$|K^0_{\rm S}\rangle = \frac{1}{(1+|\epsilon|^2)^{1/2}}(|K_1\rangle - \epsilon|K_2\rangle) \,, \tag{1.25}$$

$$|K^0_{\rm L}\rangle = \frac{1}{(1+|\epsilon|^2)^{1/2}}(|K_2\rangle + \epsilon|K_1\rangle) \,, \tag{1.26}$$

where ϵ is some small complex number. Thus, $K^0_{\rm S}$ can decay to a three pion final-state with some small probability. Similarly $K^0_{\rm L}$ can decay to a two pion state. The *CP* eigenstates can also be related to the flavour eigenstates through the following relation

$$|K_1\rangle = \frac{1}{\sqrt{2}}(|K^0\rangle - |\overline{K}^0\rangle) \,, \tag{1.27}$$

$$|K_2\rangle = \frac{1}{\sqrt{2}}(|K^0\rangle + |\overline{K}^0\rangle) \,. \tag{1.28}$$

Since this discovery, *CP* violation has also been observed in the beauty sector. In 2011 evidence was presented for *CP* violation in the charm system [37], however a more precise search in 2013 found no *CP* violation [38].

1.5 CP violation in the B system

The concept of *CP* violation was introduced in Section 1.4.3 using an example from the kaon system. This is one way in which *CP* violation can manifest itself; further methods will be discussed in this section.

Neutral B mesons are capable of oscillating between their particle and antiparticle versions, this is known as neutral meson mixing and is shown in Figure 1.12.

The B^0 mesons which are observed are described in terms of heavy ($B_{\rm H}$) and

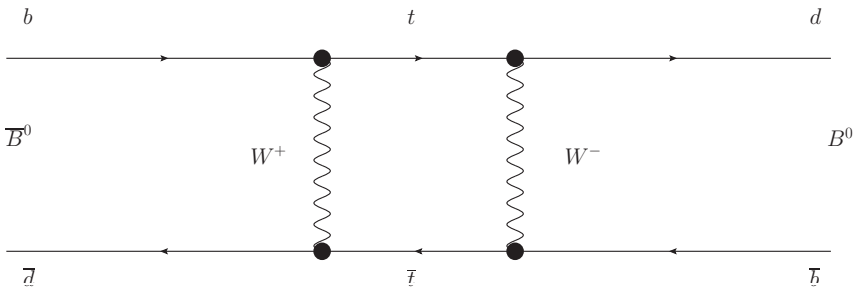

Figure 1.12: Feynman diagram showing mixing in the B^0 system.

light ($B_{\rm L}$) mass eigenstates

$$|B_{\rm H}\rangle = p|B^0\rangle - q|\overline{B}^0\rangle \,, \tag{1.29}$$

$$|B_{\rm L}\rangle = p|B^0\rangle + q|\overline{B}^0\rangle \,, \tag{1.30}$$

where p and q are complex numbers normalised such that $|p|^2 + |q|^2 = 1$.

Given the decays $B \to f$ and $\overline{B} \to f$, where f is a *CP* eigenstate which can be reached via B or $\overline{B}$ decays, the following amplitudes can be defined

$$A_f \equiv \langle f|\mathcal{H}|B\rangle \,, \tag{1.31}$$

$$\overline{A}_f \equiv \langle f|\mathcal{H}|\overline{B}\rangle \,, \tag{1.32}$$

where $\mathcal{H}$ is the Hamiltonian for weak interactions. As physics must be invariant under an arbitrary phase change γ_f, the phase of the final state can be rotated such that

$$|f\rangle \to e^{i\gamma_f}|f\rangle \,. \tag{1.33}$$

This has the following effect

$$A_f \to e^{i(\gamma-\gamma_f)}A_f \,, \tag{1.34}$$

$$\overline{A}_f \to e^{i(\overline{\gamma}-\gamma_f)}\overline{A}_f \,, \tag{1.35}$$

$$\frac{q}{p} \to e^{i(\gamma-\overline{\gamma})}\frac{q}{p} \,, \tag{1.36}$$

where γ and $\overline{\gamma}$ is the initial phases. From this it can be seen that the quantities

which are invariant under such a phase change, and thus observable, are

$$|A_f| \, , |\overline{A}_f| \, , \frac{|q|}{|p|} \, , \tag{1.37}$$

and the complex parameter

$$\lambda \equiv \frac{q}{p}\frac{\overline{A}_f}{A_f} \, . \tag{1.38}$$

These variables are important when describing *CP* violation and will be used in the following sections.

1.5.1 Direct CP violation

Direct *CP* violation requires that there are at least two processes which contribute to the decay amplitude, each with different strong and weak phases. Due to conservation of electric charge, this is the only type of *CP* violation possible in charged particles.

Considering the decays $B \to f$ and $\overline{B} \to \overline{f}$, with amplitudes A_f and $\overline{A}_{\overline{f}}$ respectively, it is possible to write down two decay amplitudes [39]

$$A_f = |A_1|e^{i(\delta_1+\gamma_1)} + |A_2|e^{i(\delta_2+\gamma_2)} \, , \tag{1.39}$$

$$\overline{A}_{\overline{f}} = |A_1|e^{i(\delta_1-\gamma_1)} + |A_2|e^{i(\delta_2-\gamma_2)} \, , \tag{1.40}$$

where $\delta_{1,2}$ are the *CP* invariant strong phases and $\gamma_{1,2}$ are *CP*-odd weak (CKM) phases. The decay rates are proportional to the amplitudes squared

$$|A_f|^2 = |A_1|^2 + |A_2|^2 + 2|A_1||A_2|\cos(\delta_1 - \delta_2 + \gamma_1 - \gamma_2) \, , \tag{1.41}$$

$$|\overline{A}_{\overline{f}}|^2 = |A_1|^2 + |A_2|^2 + 2|A_1||A_2|\cos(\delta_1 - \delta_2 + \gamma_2 - \gamma_1) \, . \tag{1.42}$$

The difference between these rates is

$$|A_f|^2 - |\overline{A}_{\overline{f}}|^2 = 4|A_1||A_2|\sin(\delta_1 - \delta_2)\sin(\gamma_1 - \gamma_2) \, . \tag{1.43}$$

Direct *CP* violation occurs when Equation 1.43 is non-zero, *i.e.*

$$\frac{|A_f|}{|\overline{A}_{\overline{f}}|} \neq 1 \, . \tag{1.44}$$

From Equation 1.43 it can be seen that Equation 1.44 is only satisfied when both the weak and strong phase differences are non-zero.

Experimentally this corresponds to a difference in yields between $B \to f$ and $\overline{B} \to \overline{f}$

$$A_{CP}(B \to f) = \frac{N(\overline{B} \to \overline{f}) - N(B \to f)}{N(\overline{B} \to \overline{f}) + N(B \to f)} \, , \tag{1.45}$$

where N are the number of events observed after corrections which take the detector acceptance and production asymmetry into account.

Direct *CP* violation has been observed in the decay $B^0 \to K^+\pi^-$, most recently by the LHCb collaboration [40]. The *CP* asymmetry is measured to be

$$A_{CP}(B^0 \to K^+\pi^-) = -0.080 \pm 0.007 \text{ (stat)} \pm 0.003 \text{ (syst)} \, . \tag{1.46}$$

The LHCb collaboration has also shown the first observation of *CP* violation in the B_s^0 system using the decay $B_s^0 \to K^-\pi^+$ [40], measuring

$$A_{CP}(B_s^0 \to K^-\pi^+) = -0.27 \pm 0.04 \text{ (stat)} \pm 0.01 \text{ (syst)} \, . \tag{1.47}$$

1.5.2 Indirect CP violation

Indirect *CP* violation is sometimes called '*CP* violation in mixing' because it occurs when

$$\frac{|q|}{|p|} \neq 1 \, , \tag{1.48}$$

where q and p are defined in Equation 1.30. This corresponds to a difference in probability

$$P(B \to \overline{B}) \neq P(\overline{B} \to B) \, , \tag{1.49}$$

where $P(B \to \overline{B})$ is the probability of oscillation from a B meson to a $\overline{B}$ meson and $P(\overline{B} \to B)$ is the probability for the opposite process.

Experimentally this type of CP violation is measured by comparing the number of B mesons produced which decay as $\overline{B}$ and vice-versa. The flavour of the B meson at decay is typically determined from the charge of the B decay products while the flavour at production is determined from the opposite B meson; as in the measurement made by LHCb in the mode $B_s^0 \to D_s^+ \mu^- \overline{\nu}_\mu$ [41]

$$a_{\rm sl}^s \equiv \frac{N(\overline{B} \to f) - N(B \to \overline{f})}{N(\overline{B} \to f) + N(B \to \overline{f})} \tag{1.50}$$

$$= (-0.06 \pm 0.50 \pm 0.36)\% \; . \tag{1.51}$$

This is in agreement with the Standard Model, which predicts only a small amount of CP violation in B-mixing [42].

In a similar measurement, the same-sign dimuon asymmetry presented by the D0 collaboration includes contributions from B^0 and B_s^0 mesons [43]

$$A_{\rm sl}^b = C_d a_{\rm sl}^d + C_s a_{\rm sl}^s \; , \tag{1.52}$$

$$= (-0.496 \pm 0.153 \pm 0.072) \times 10^{-2} \; , \tag{1.53}$$

where the $C_{d,s}$ parameters include the effects of B^0 and B_s^0 meson flavour oscillation and the difference in production rates of these mesons. In contrast to the LHCb results, this measurement differs from the Standard Model prediction by 2.8 standard deviations.

1.5.3 CP violation in interference

If a final state is accessible from both B and $\overline{B}$ states there can be CP violation even if both $|A_f|/|\overline{A}_{\overline{f}}| = 1$ and $|q|/|p| = 1$. This is possible because of the interference between states which oscillate before decay, $B \to \overline{B} \to f$, and those which do not, $B \to f$. The following statement needs to be true for CP symmetry to be broken in this way:

$$\mathcal{I}m(\lambda) \neq 0 \; , \tag{1.54}$$

where λ is defined in Equation 1.38.

The angle β is the phase of a ratio of CKM elements and measuring it with high precision was one of the main goals of the B-factories. The angle arises from interference between mixing and decay and is defined as

$$\beta = \arg\left[\frac{V_{cb}^* V_{cd}}{V_{tb}^* V_{td}}\right] . \tag{1.55}$$

This angle is determined from a decay-angle and time-dependent fit, typically using the tree-level decay mode $B^0 \to J/\psi K_S^0$ because of its high branching fraction. The world average value is [10]

$$\sin 2\beta = 0.675 \pm 0.020 , \tag{1.56}$$

which is dominated by the B-factory measurements [44, 45].

A complimentary measurement, β_{eff}, can be made using the decay mode $B^0 \to \phi K_S^0$. The value of β_{eff} is expected to differ slightly from β as $B^0 \to \phi K_S^0$ must proceed via a loop diagram and so has a different decay amplitude; this also makes it an excellent probe of new physics. The BaBar collaboration have made a measurement using this channel and found

$$\beta_{\text{eff}} = 0.22 \pm 0.27 \pm 0.12 , \tag{1.57}$$

where the first uncertainty is statistical and the second systematic [46].

A similar measurement has been performed by LHCb using the decay mode $B_s^0 \to J/\psi K^+ K^-$. The CP violating phase ϕ_s is the counterpart to β using the B_s^0 system

$$\phi_s = -2\arg\left[\frac{V_{tb}^* V_{ts}}{V_{cb}^* V_{cs}}\right] . \tag{1.58}$$

Again it is extracted via a time and angle dependent fit to give [47]

$$\phi_s = 0.07 \pm 0.09 \text{ (stat)} \pm 0.01 \text{ (syst) rad} , \tag{1.59}$$

which is consistent with the Standard Model expectation of $\phi_s \simeq -0.03$ [48].

The decay $B_s^0 \to \phi\phi$ also proceeds via a loop diagram and can be used to determine the CP violating phase $\phi_s^{\phi\phi}$. This is the $b \to s\bar{s}s$ transition equivalent

of ϕ_s, which uses $b \to s\bar{c}c$ decays. LHCb has measured this phase to be [49]

$$\phi_s^{\phi\phi} = -0.17 \pm 0.15 \text{ (stat)} \pm 0.03 \text{ (syst) rad} , \tag{1.60}$$

which is consistent with the Standard Model expectation of $|\phi_s^{\phi\phi}| < 0.02$ [50–52]. The decay $B_s^0 \to \phi\phi$ is topologically similar to $B^0 \to \phi K^{*0}$, which is discussed in Chapters 3, 4, 5 and 6.

Chapter 2

The LHCb detector

2.1 The Large Hadron Collider

The Large Hadron Collider (LHC) [53] is the largest experiment on Earth. It occupies the 27 km long tunnel originally used by the Large Electron-Positron Collider, and with a design energy of 7 TeV per proton beam is the highest energy particle collider ever built.

The LHC aims to answer the following questions

- Is the Higgs mechanism responsible for electroweak symmetry breaking and therefore the masses of the gauge bosons?
- Is the Standard Model a complete representation of nature, or is it simply a part of a larger design such as Supersymmetry?
- What is the origin of dark matter and dark energy?
- Why is there an abundance of matter and very little antimatter in the Universe?

The first of these questions has already been answered by the ATLAS and CMS collaborations with the discovery of a new boson of mass $\sim 126\,\mathrm{GeV}/c^2$ [15,16]. To answer the remaining questions requires either directly producing new particles or indirectly probing their effects in virtual quantum loops.

The LHC is designed to circulate and collide protons at a centre-of-mass energy of 14 TeV, seven times greater than that of the Tevatron, the previous collider at the energy frontier. The design luminosity of the LHC is $1 \times$

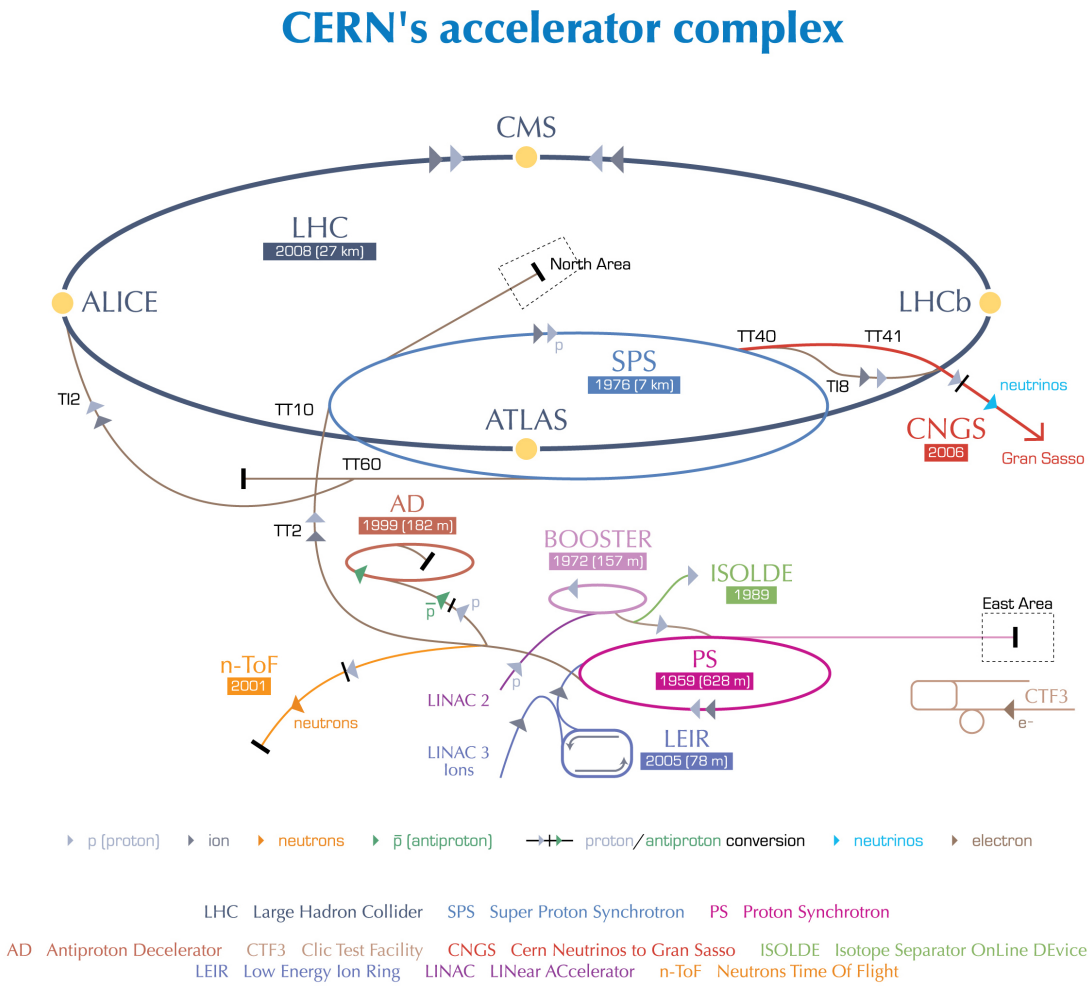

Figure 2.1: The CERN accelerator complex and experimental sites (not to scale) [54].

$10^{34}\text{cm}^{-2}\text{s}^{-1}$ with a maximum bunch crossing rate of 40 MHz. The maximum number of bunches is 2808 and each bunch contains around 100 billion protons. However, as a result of a poorly soldered joint causing a major quench in 2008 [55], the centre-of-mass energy was limited to 7 TeV during 2011. During this time the LHC reached a maximum instantaneous luminosity of $\sim 4 \times 10^{33}\text{cm}^{-2}\text{s}^{-1}$.

The protons which eventually collide inside one of the experiments at the LHC begin as hydrogen molecules. The hydrogen is then heated to produce a plasma after which the electrons are stripped from the protons using a magnetic field. The protons are then injected into the first stage of the LHC acceleration chain, LINAC2. Here they are accelerated to an energy of 50 MeV before passing into the

Proton Synchrotron Booster which accelerates the protons to a further 1.4 GeV. The proton bunches then pass through the Proton Synchrotron (25 GeV) and the Super Proton Synchrotron before being injected into the LHC with an energy of 450 GeV. A diagram of the accelerator chain is shown in Figure 2.1.

The LHC is host to four main experiments. The detectors are split between General Purpose Detectors (GPDs), ATLAS [56] and CMS [57], and more specialised experiments, ALICE [58] and LHCb [59]. The GPDs are built to exploit the unique energy of the LHC and search for new particles directly produced in collisions. ALICE is an experiment designed to study the collision of lead ions, which can be injected into the LHC in the place of protons. Finally, LHCb is built to study particles containing b or c quarks, with an emphasis on rare decays and *CP* violation.

2.2 The LHCb spectrometer

The Large Hadron Collider Beauty (LHCb) experiment is a single-arm forward spectrometer designed to take advantage of the huge beauty and charm cross sections at the LHC. When produced at the LHC, $b\bar{b}$ pairs are primarily formed in gluon-gluon fusion. As the energies involved are much greater than the $b\bar{b}$ rest mass, the resulting b quarks are highly boosted in the direction of the beam axis, as shown in Figure 2.3. The geometry of LHCb is optimised to take advantage of this by covering the angular range 10-300(250) mrad in the bending (non-bending) plane.

The detector is constructed from several sub-detectors with the layout shown in Figure 2.2. The z-axis is along the beam pipe whilst the y-axis is in the vertical direction, the x-axis completes a right-handed coordinate system.

Each aspect of the detector has been optimised for the measurement of *CP* violation and the study of rare decays. The tracking system is composed from the Vertex Locator and tracking stations, and provides precise vertexing of the interaction point. This gives the experiment excellent proper-time and momentum resolution which is vital for the study of the quickly oscillating B_s^0 meson and is useful for rejecting combinatorial background. Precise particle identification is provided by two Ring Imaging Cherenkov (RICH) detectors, allowing LHCb to distinguish between different types of charged hadron in a

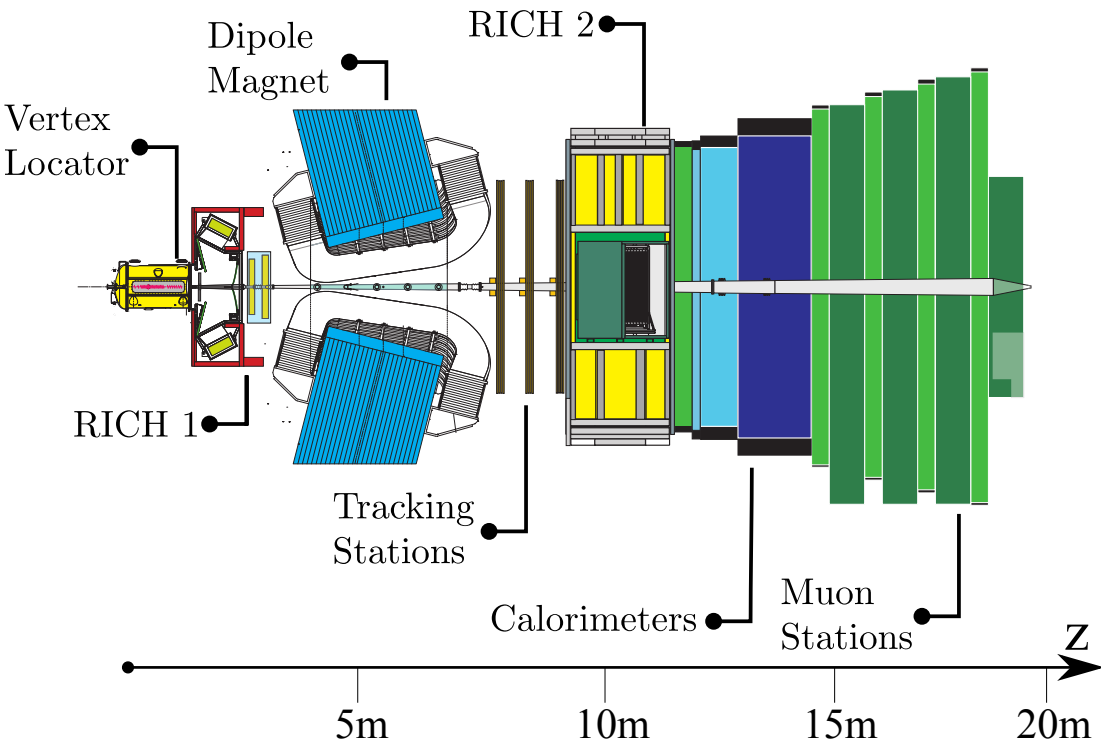

Figure 2.2: Layout of the LHCb detector.

large momentum range (2-100 GeV). The calorimeter system provides energy measurements of electrons, photons and hadrons and is also used in the trigger system. The muon stations identify muons and measure their momentum for use in the trigger. The trigger itself is highly flexible and records both leptonic and hadronic final states of b and c quarks with high efficiency.

The experiment is designed to be optimal when the number of visible interactions per bunch crossing is ~ 1. This makes events easier to analyse and reduces radiation damage to the detector. Low occupancy in the subsystems also reduces the bandwidth required to read out the detector. The experiment was designed to be optimal for a luminosity of $2 \times 10^{32}\text{cm}^{-2}\text{s}^{-1}$, two orders of magnitude below the nominal luminosity of the LHC and the GPDs. However, for much of 2011 and 2012 LHCb recorded data at an instantaneous luminosity of $4 \times 10^{32}\text{cm}^{-2}\text{s}^{-1}$. Achieving lower luminosity at the LHCb interaction point requires the focussing quadrupoles to be further away from the collision point than in the GPDs, and to be of a lower strength. The beams can also be adjusted to have some displacement in the transverse direction while maintaining the same

interaction point. This displacement can be altered during a fill to maintain constant luminosity in LHCb.

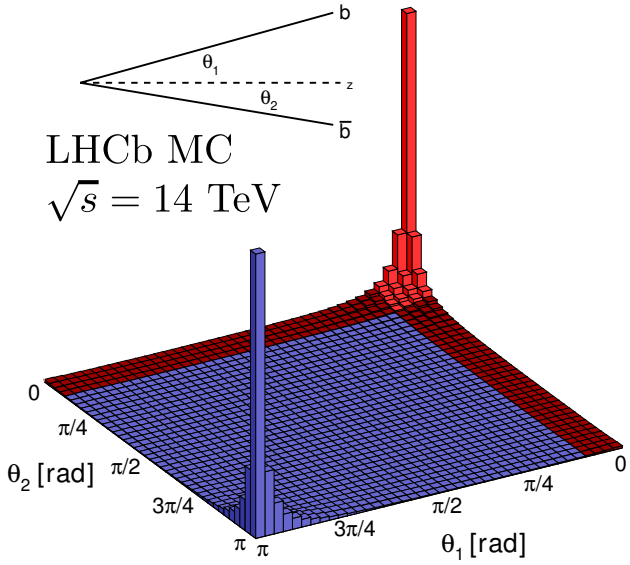

Figure 2.3: Simulation showing the production angles of pairs of b quarks with respect to the beam axis [60]. The angles shown in red are inside the LHCb detector acceptance.

2.3 Tracking system

The tracking system is used to reconstruct the trajectories of charged particles passing through the detector. The tracking system of an experiment dedicated to flavour physics is arguably one of the most important components as this can be used to identify secondary vertices displaced from the primary interaction point. This is a distinctive feature of heavy flavour decays. Combining tracking information taken before and after the magnet allows the momentum of each particle to be determined. The tracking system is comprised of a dipole magnet, the Vertex Locator (VELO) and four tracking stations.

2.3.1 Magnet

A warm dipole magnet is used to deflect charged particles in the x-direction [59, 61]. This allows momentum to be measured based on the curvature of a track. A

superconducting magnet was considered but was excluded based on construction cost and time.

The magnet is formed from a window-frame yolk of steel construction and coils of aluminium as seen in Figure 2.4. The yolk supports the coils and shapes the magnetic field. Two coils are placed symmetrically above and below the beam and are saddle shaped to follow the detector acceptance. This minimises the required current, hence the cost, while generating the required integrated B field. The coils are made from 15 layers of hollow aluminium 'pancakes' with a central volume for water cooling of 25 mm diameter. The total weight of the yolk and coils exceeds 1500 tons.

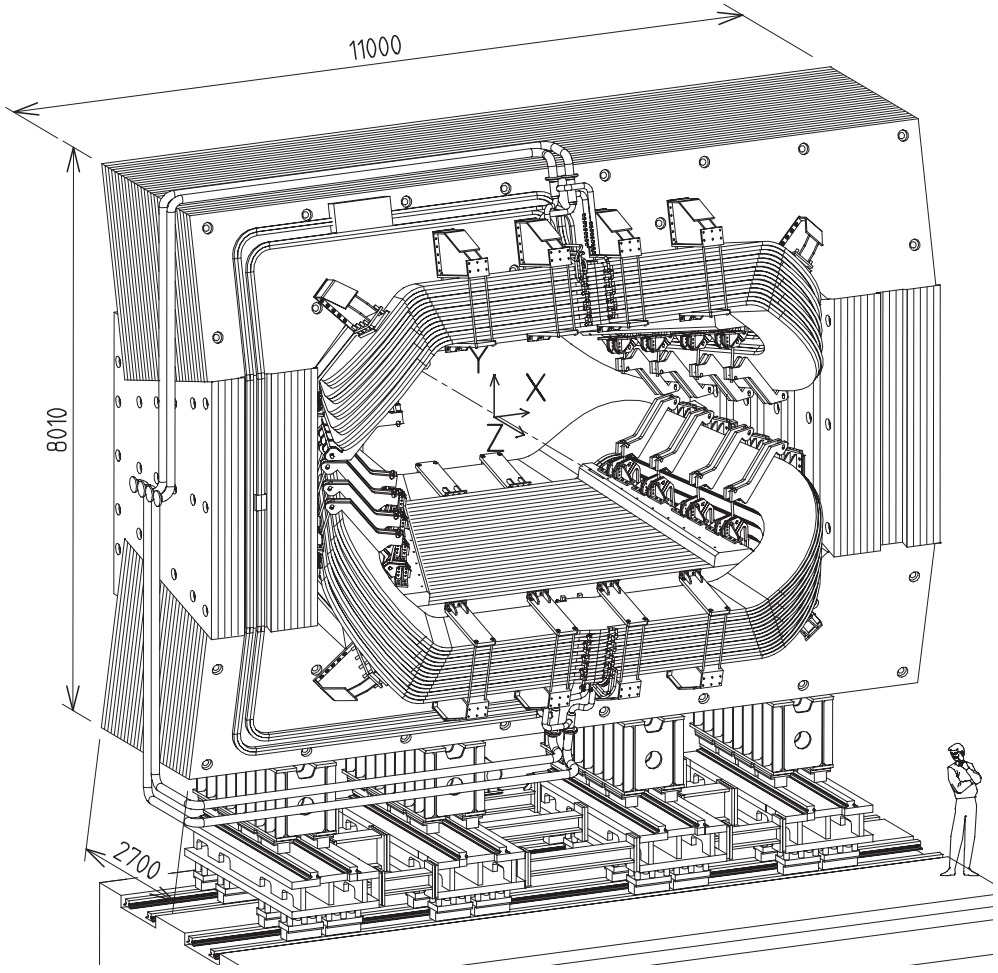

Figure 2.4: LHCb dipole magnet with water and current connections shown (dimensions in mm). The interaction point lies upstream from the magnet which is into the page in this view.

The integrated B field from 0 to 10 m in the z direction is ~ 4 Tm. This is required to achieve the tracking requirements of $\delta p/p = 0.6$ % for momentum (p) up to 200 GeV/c.

2.3.2 Vertex locator

Reconstructing particle decay vertices in a hadronic environment is a challenging but rewarding exercise. Due to the $\sim$ 1.5 ps lifetime of b hadrons and the relativistic boost in the lab frame, decay vertices found 1 cm from the primary interaction point are typical. It is the role of the VELO to reconstruct the primary and secondary vertices using space points from tracks measured around the beam pipe. Without this separation of vertices, accurate measurements of beauty and charm hadron decay times would not be possible.

The VELO is constructed from 21 silicon sensor stations arranged from -18 cm to +80 cm in the z-axis with the detection plane perpendicular to the beam direction, as shown in Figure 2.5. Each station is composed of two silicon strip detectors. One uses a radial strip layout to measure tracks in the ϕ direction and the other uses an azimuthal layout to measure tracks in the R direction. Each VELO sensor has a circular construction where the inner radius of the active area is 8.17 mm and the outer radius is 42 mm. The small inner radius means the distance between the decay vertex and the first hit in the VELO is minimised, improving the resolution. However, this distance is smaller than the aperture required by the LHC during beam injection when the beams are broad. For this reason each VELO sensor is made from two retractable halves. Each half is moved out by 30 mm during injection via a stepper motor system. Both detector halves cover 182° in ϕ allowing full angular coverage and the ability to internally align the detector using tracks. Due to the overlap, each sensor half is displaced by 15 mm in the z direction from its partner.

The R measuring sensors are subdivided into four sections of 512 strips in order to reduce occupancy and improve track reconstruction speed. The strip pitch increases from 40 μm at the inner edge to 101.6 μm at the outer edge. The ϕ measuring sensor is split into an inner and outer region of 683 and 1365 strips respectively also for reasons of occupancy. The pitch is 35.5 (39.3) μm at the inside edge of the inner (outer) region, increasing linearly to 78.3 (96.6) μm at the outside edge of the inner (outer) region. The ϕ strips do not radiate outwards

perpendicular to the centre but at a small angle; one region has a skew of $-10°$ and the other $+20°$. Which region has which skew is alternated between subsequent VELO stations to help associate correct ϕ and R hits in the detector.

In order to protect the LHC vacuum from outgassing of the VELO equipment and to shield the VELO electronics from RF pickup coming from the beam, a secondary vacuum vessel is placed around each half of the VELO detector. It is constructed from 0.3 mm-thick aluminium foil which is doped with magnesium to increase its strength. The foil is corrugated to reduce the amount of material seen by the particles and also to accommodate the overlapping sensor structure. This has the added benefit of increasing the stiffness of the foil.

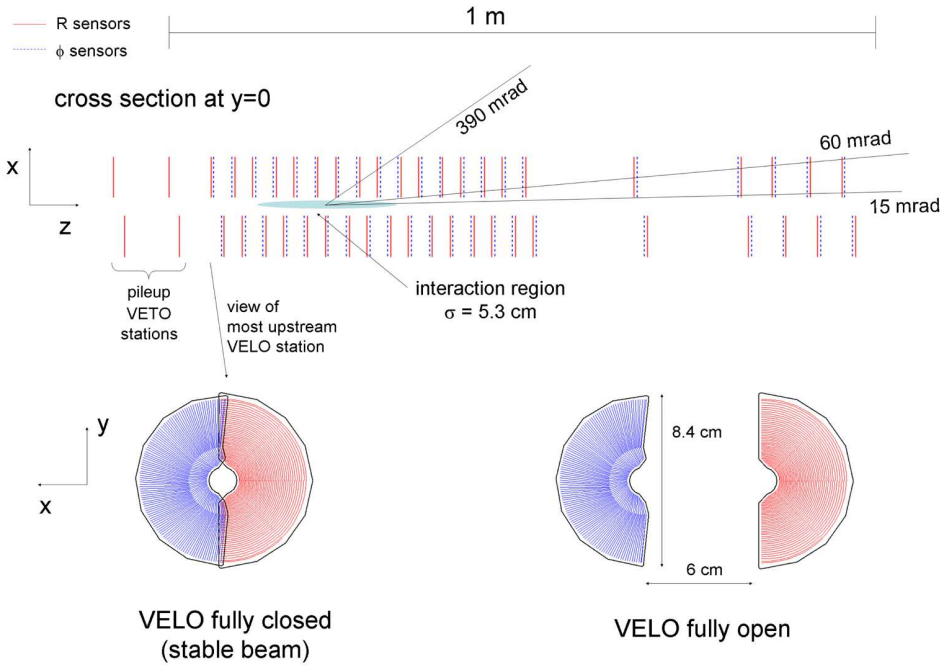

Figure 2.5: VELO sensor location [59] on the beam axis and diagram showing closed (left) and open (right) VELO positions. The pileup VETO stations are not currently used by the experiment.

2.3.3 Tracking stations

Following the VELO, the LHCb tracking stations provide information on particle tracks both up and downstream of the magnet. The Tracker Turicensis (TT),

Inner Tracker (IT) and Outer Tracker (OT) make up the tracking system.

The TT is located immediately downstream of RICH1 before the magnet and covers the entire acceptance. Its primary uses are to improve momentum resolution and to record long-lived tracks such as those from K^0_S mesons, which are electrically neutral and typically decay outside of the VELO acceptance. Three more equidistant tracking stations (T1-T3) are immediately downstream of the magnet. The inner and outer region of each tracking station, known as the IT and OT respectively, use different technologies. The TT and IT both use silicon microstrip technology and are collectively referred to as the Silicon Tracker (ST) project, while the OT is constructed from gaseous straw drift tube detectors.

Each station of the ST has four silicon detector layers. The first and last layers measure hits in the x-direction using vertical strip readouts whereas the second and third layers are rotated by a stereo angle of $+5^\circ$ and -5° allowing sensitivity in the y-direction. In the TT there is a gap of $\sim 30\,\text{cm}$ between the stereo layers in order to improve the momentum resolution at the trigger level. The distance between the corresponding layers in the IT is $\sim 4\,\text{cm}$.

Each IT layer is divided into four detector boxes to cover the areas above, below, left and right of the beam pipe. The sensors must be maintained at less than 5°C to reduce leakage current caused by radiation damage from the beam. Therefore the boxes are thermally, electrically and optically isolated.

The OT uses straw drift tubes to record particle tracks. It uses the same detector layout as the ST with quadrants surrounding the beam pipe making up a single station. Each module consists of two layers of straw tubes staggered by a distance of 5.5 mm. The tubes have an inner diameter of 4.9 mm and are filled with the a mixture of argon and CO_2 in the ratio 70/30 to give a fast drift time while utilising a non-flammable gaseous mixture [59]. Keeping the drift time below 50 ns restricts hits from overlapping events. This improves track reconstruction efficiency and lowers the probability of spurious tracks being created in the detector reconstruction. The layout of the OT tracking stations, including a cross section of a single module, is shown in Figure 2.6.

Using LHCb collision data taken between 2010 and 2012 the average efficiency of all OT modules was measured to be (99.3 ± 0.3) % for hits near the centre of the straws [62]. For hits near the edge of the straw the efficiency is slightly lower, as seen in Figure 2.7. The non-zero efficiency for hits predicted outside

the radius of the straws is due to random hits from other tracks not under study and is proportional to detector occupancy.

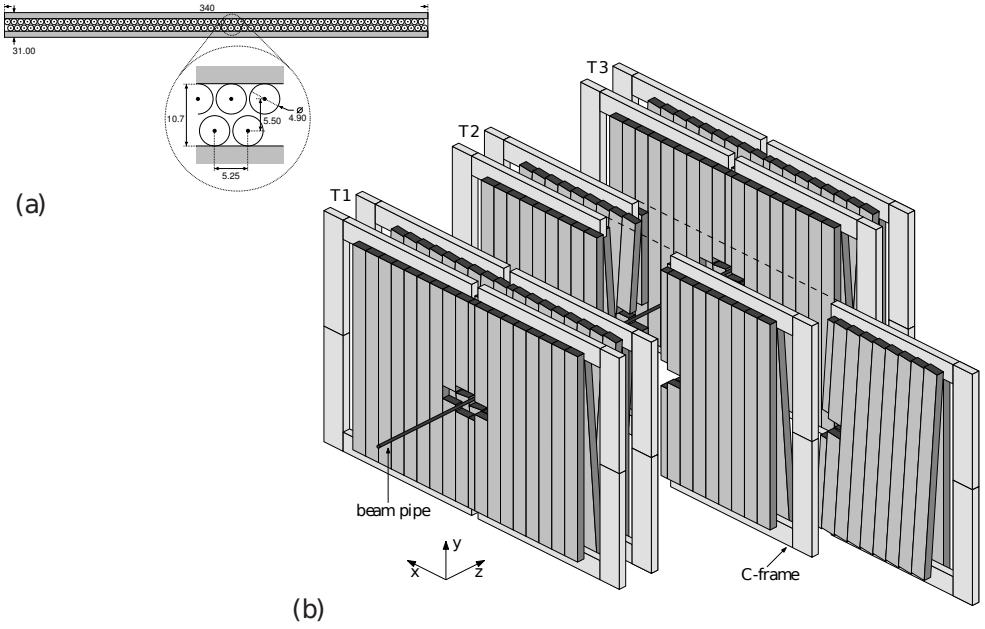

Figure 2.6: (a) OT module cross section. (b) Layout of OT stations and modules in the LHCb detector. The second station (T2) is shown in an exploded view [62].

2.4 Particle identification

The role of particle identification (PID) is to efficiently distinguish between different types of charged particles, specifically electrons, muons, pions, kaons and protons. This is vital for many of the analyses conducted by LHCb, particularly in fully hadronic modes where good PID is needed to separate different final states.

Particle identification is also used in a process called *flavour tagging*, which identifies whether a b hadron is matter or antimatter. This is used in many analyses which cannot infer the decaying b hadron flavour by using its decay products. The *same side tagger* makes a decision on the flavour of b hadrons by identifying the charged kaon which was produced during the hadronisation process [63]. The *opposite side tagger* uses the charged daughters of the other

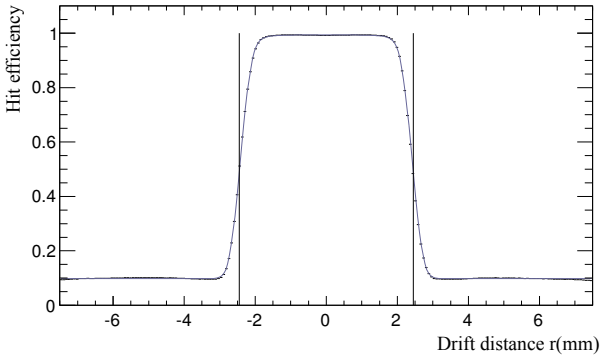

Figure 2.7: Efficiency profile of a typical OT module as a function of the drift distance. The vertical lines signify the edge of the straw tube at $|r| = 2.45\,\text{mm}$ [62].

b decay in the event to make a decision [64]. These methods are not possible without accurate particle identification.

2.4.1 RICH system

LHCb uses Ring Imaging Cherenkov (RICH) detectors to separate charged hadrons. The RICH system is composed of two independent sub-detectors which provide particle identification over different momentum ranges. Situated upstream of the magnet immediately after the VELO, RICH1 covers the full LHCb acceptance. This upstream position allows RICH1 to identify particles which are later swept out of the detector acceptance and minimises the detector area needed to give full angular coverage. The RICH2 detector is placed downstream, situated between the last tracking station and the first muon station. It covers a smaller acceptance of $\pm 15\,\text{mrad}$ to $\pm 120\,\text{mrad}$ ($\pm 100\,\text{mrad}$) in the horizontal (vertical) plane. This is consistent with the polar angle distribution of high momentum tracks coming from b decays in the forward direction.

The RICH detectors make use of the Cherenkov effect. When a charged particle passes through a dielectric medium the atoms inside the material interact with the electromagnetic field and become polarised. These atoms then return to the ground state via photon emission. If the speed of the charged particle is greater than the local phase velocity of light in the medium then these photons interfere constructively. A wavefront is then emitted forming a cone with a

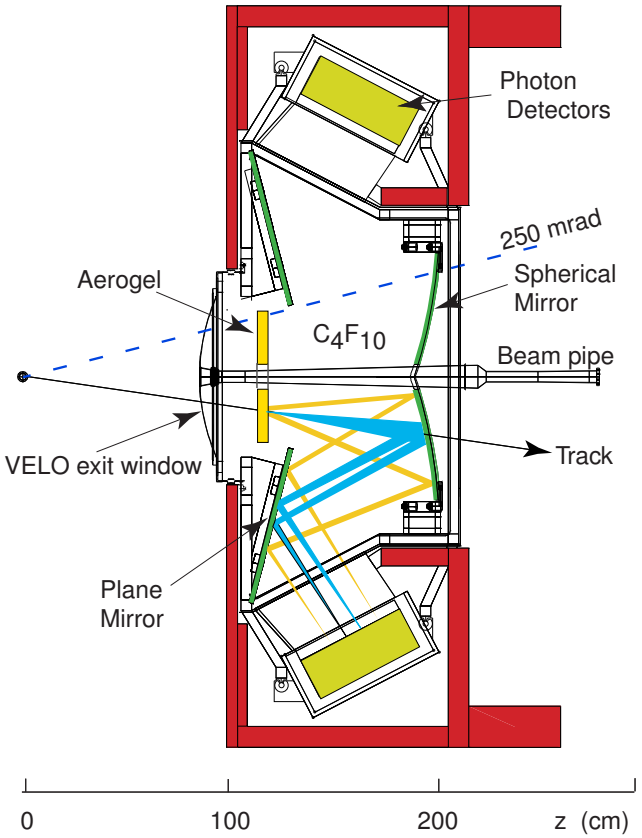

Figure 2.8: Cross section of the RICH1 detector showing the layout of mirrors and photon detector arrays [65].

Cherenkov angle, θ_c, to the particle direction. The Cherenkov angle is related to the speed of the charged particle by the following equation

$$\cos\theta_c = \frac{1}{\beta n}\ , \tag{2.1}$$

where n is the refractive index of the material and $\beta = v/c$ is the ratio of the particle velocity and the speed of light in a vacuum. Therefore if θ_c is measured and n is known, the speed of the particle can be inferred. The particle speed is combined with the momentum measured by the tracking system to determine the particle mass.

Each RICH detector consists of two spherical mirrors, two flat mirrors, two photon detector arrays, and radiator materials. The radiators for RICH1 are a 5 cm-thick slice of aerogel and 85 cm of C_4F_{10} gas. The aerogel has a refractive

index of 1.03 and provides π-K separation below 10 GeV/c while the C_4F_{10} has a refractive index of 1.003 and provides π-K separation up to $\sim$ 50 GeV/c. RICH2 utilises 170 cm of CF_4 gas as a radiator to cover the momentum range $\sim$ 20 $-$ 100 GeV/c.

The radiators are located around the beam pipe. The spherical and flat mirrors focus the Cherenkov light onto the RICH detector planes which are located outside of the LHCb acceptance to reduce the material budget. The RICH1 layout is shown in Fig. 2.8.

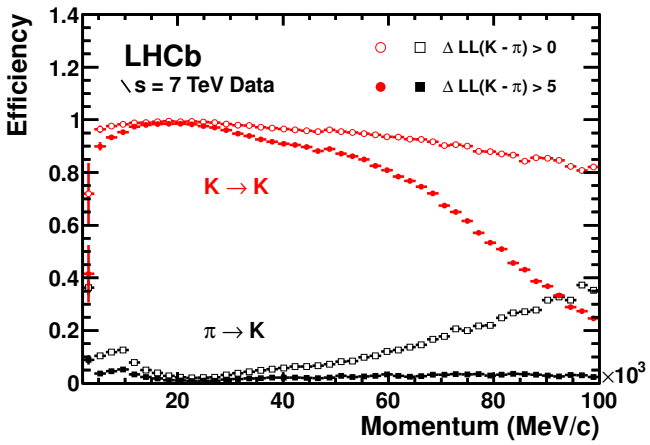

Figure 2.9: Kaon identification efficiency (red) and pion misidentification rate (black) as a function of momentum: calculated using data [66]. The filled and open markers represent different requirements on the likelihood that a particle is a kaon, with the filled markers being the more stringent requirement.

The detector arrays use the Hybrid Photon Detector (HPD) to record the Cherenkov light. The HPDs are an amalgamation of vacuum photocathode and silicon pixel technology with integrated readout electronics. The HPDs have a 7 mm-thick spherical quartz entrance window with a thin multi-alkali photocathode deposited on the inner surface. Photons passing through the window are converted to electrons via the photoelectric effect and accelerated by a $-$20 kV electric field onto the sensor. Additional electrodes provide focussing and demagnification.

The sensor is a 300 µm-thick silicon pixel detector. The chip contains 8192 pixels with dimension 500 $\times$ 62.5 µm each and a logical OR is taken between eight adjacent pixels giving an effective pixel count of 1024, each with dimension

$0.5 \times 0.5\,\text{mm}$. Accounting for the demagnification this gives a 2.5 mm resolution on the quartz entrance window.

Figure 2.9 shows the kaon identification and pion misidentification rate as a function of momentum and Figure 2.10 shows the clear separation of different charged particle species based on Cherenkov angle. Using data the kaon identification efficiency averaged over the momentum range 2-100 GeV/c, was found to be ~ 95 % with 10 % pion misidentification fraction [66]. The data used correspond to $\Delta LL(K - \pi) > 0$ in Figure 2.9. An example of the discrimination provided by the RICH system is shown in Figure 2.11 using $B \to h^+h^-$ decays.

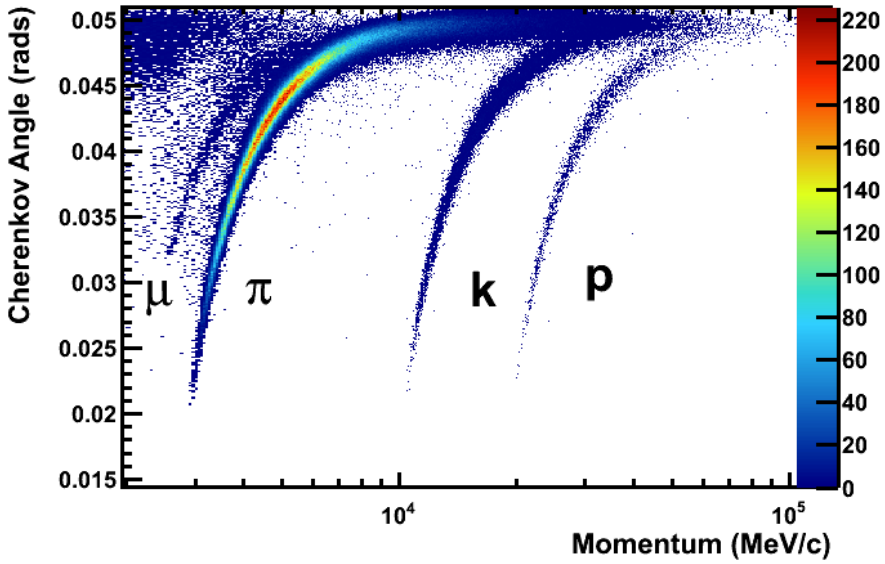

Figure 2.10: Reconstructed Cherenkov angle as a function of particle momentum for the C_4F_{10} radiator. Bands identifying protons, kaons and pions are clearly visible [66].

2.4.2 Calorimeters

The role of the calorimetry system is to identify hadrons, electrons and photons and make measurements of their energy deposition and spatial position. This allows the reconstruction of neutral particles which decay to photons such as π^0 and the tagging of electrons from semileptonic b decays. One of the most important uses of the calorimeter is to trigger on high energy hadrons, allowing LHCb to collect large samples of b mesons and baryons which decay hadronically.

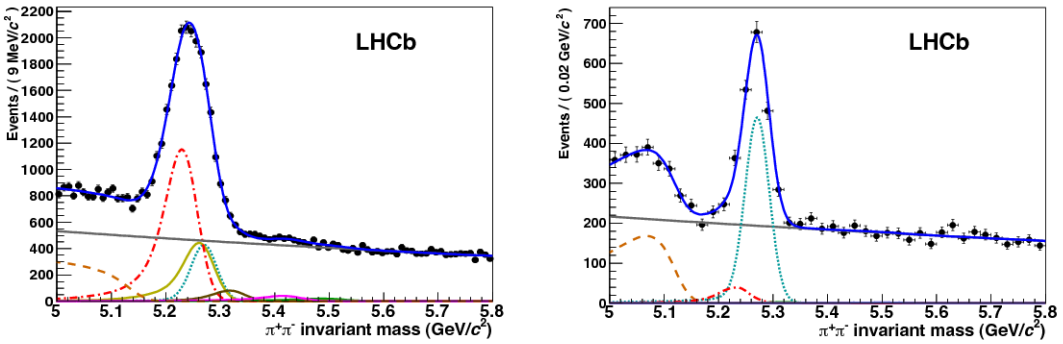

Figure 2.11: Invariant mass distribution for $B \to h^+h'^-$ decays using LHCb data [67] before (left) and after (right) particle identification has been applied by the RICH. The turquoise line represents the signal under study, $B^0 \to \pi^+\pi^-$. Other b-hadron decays are represented by the red dot-dashed line ($B^0 \to K^+\pi^-$), orange dashed line ($B^0 \to$ 3-body), yellow line ($B_s^0 \to K^+K^-$), brown line ($B_s^0 \to K^-\pi^+$), purple line ($\Lambda_b^0 \to pK^-$) and green line ($\Lambda_b^0 \to p\pi^-$). The combinatorial background is represented by the grey line [66].

The calorimeter system is composed of a Scintillating Pad Detector (SPD), Preshower detector (PS), Electromagnetic Calorimeter (ECAL) and a Hadronic Calorimeter (HCAL), allowing energy and position measurements to be made over a range of particle types. Each component of the calorimeter system covers the detector acceptance down to 25 mrad, which prevents radiation damage from particles near the beam pipe.

The SPD is placed immediately downstream of RICH2. It is a 15 mm-thick scintillating pad and uses Wavelength Shifting Fiber (WSF) to collect the scintillation light, which is then transferred to a Multi-Anode Photomultiplier Tube (MAPMT). As only charged particles produce scintillation light, the SPD allows the separation of electron and photon showers collected by the ECAL. The SPD can also be used to estimate track multiplicity and events with a large number of tracks are rejected by the trigger (see Sec. 2.5).

The PS is identical in construction and operation to the SPD. The addition of a 12 mm-thick block of lead between the SPD and the PS allows the PS to be used to separate electron and hadron showers due to the difference in their shower properties.

The ECAL resides downstream from the PS. It is a sampling calorimeter which alternates 4 mm-thick layers of scintillating material and 2 mm-thick layers

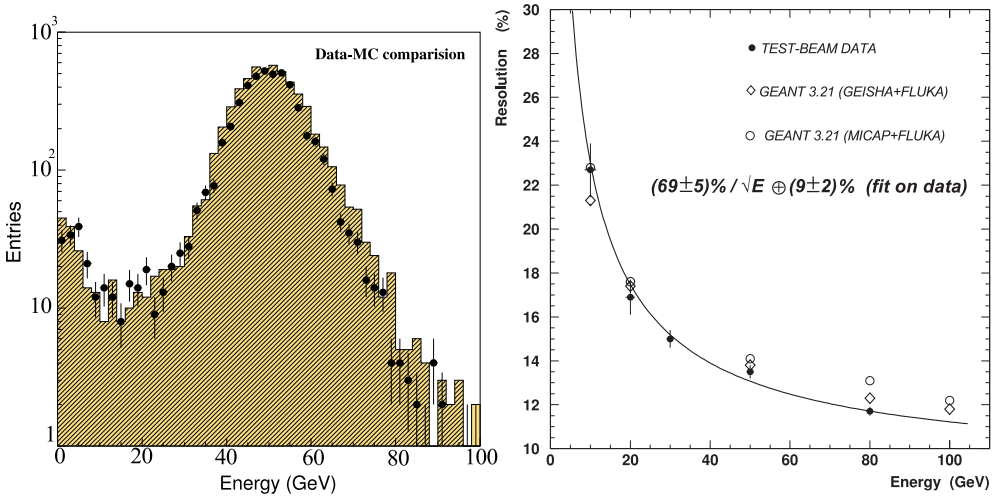

Figure 2.12: Left: Hadronic calorimeter response to 50 GeV pions from test-beam (hatched histogram) and from simulation (dots). Right: HCAL energy resolution in test beam data (filled dots) and different simulation codes (open dots). The curve is a fit to the test-beam data [59].

of lead. The layers are orthogonal to the beam direction and have WSF threaded throughout to collect scintillation light. Each ECAL, SPD and PS scintillator panel is divided into three regions of cell length $\sim 4, 6$ and 12 cm with the most coarse layer being furthest from the beam pipe. This follows the model used by other sub-detectors to optimise resolution and maintain roughly constant hit occupancy throughout the detector. The complete ECAL utilises 66 lead/scintillator layers for a total depth in z of 835 mm, corresponding to a total of 25 radiation lengths (X_0). This ensures that high energy photons are completely absorbed and thus provides optimal energy resolution. The design resolution of the ECAL is $10\%/\sqrt{E} \pm 1$ % [68].

The operating principle of the ECAL and HCAL is similar but the layout of the HCAL within LHCb is rather different. The HCAL is also a sampling calorimeter with scintillating material interspersed with sheets of iron, but unlike the ECAL these layers are parallel to the beam direction. This means the incoming particles have a 'side on' view of the tiles. The iron is 1 cm thick in the lateral direction while in the longitudinal direction the iron and scintillator corresponds to a single hadronic interaction length (λ_I) in steel. As hadronic showers are more collimated than electromagnetic cascades this orientation improves sampling in the $x - y$ plane. The HCAL layers are divided into an inner and outer area of cell width

131.3 mm and 262.6 mm respectively. Limited by the size of the cavern, the complete HCAL corresponds to 5.7 hadronic interaction lengths (λ_I). This is not enough to fully contain hadronic showers and leads to a moderate resolution of $(69 \pm 5)\%/\sqrt{E} \oplus (9 \pm 2)$ % [59]. Figure 2.12 shows the HCAL response to 50 GeV pions from test-beam data. This resolution is sufficient to fulfill the main purpose of the HCAL, which is to trigger on hadronic particles.

2.4.3 Muon stations

Leptons make up around 10% of the total b-hadron branching fraction and several high profile analyses have muons in the final state, making efficient muon identification paramount to the success of the experiment. The muon system provides the ability to trigger on events involving muons with high transverse momentum (p_{T}) and is used together with the calorimeters in the first trigger stage (see Section 2.5.1). To do this the muon system must achieve a time resolution of less than one bunch spacing (25 ns). The second major function of the muon system is to allow offline muon identification with high efficiency and low π misidentification. This is especially important in semileptonic decays of neutral mesons as the charge of the muon provides information on the flavour of the decaying parent meson.

As muons are highly penetrating, the muon system is the furthest sub-detector from the interaction point. It comprises five tracking stations, M1-M5, interleaved with iron shielding. The first of these, M1, is positioned before the calorimeter preshower to allow for a more precise momentum measurement in the muon trigger (see Section 2.5). Further stations are positioned immediately after the hadronic calorimeter interleaved with layers of iron which shields the stations from hadrons. Each chamber consists of four concentric square regions with different logical pad granularity. As the particle flux increases closer to the beam pipe the granularity of the pad also increases, this is illustrated in Figure 2.13. The granularity is greater in the bending plane to improve the precision of the momentum calculation.

Each station is made up from four layers of Multi-Wire Proportional Chamber (MWPC) with two adjacent layers read out using a logical OR. The first station is an exception as it uses two layers of MWPC for the outer region and Gas Electron Multiplier (GEM) technology for the inner region. Reducing the

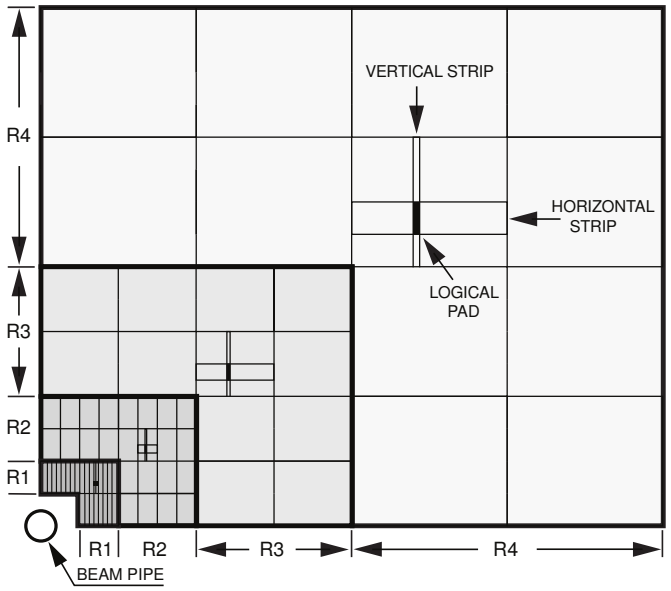

Figure 2.13: Front view of muon station quadrant, corresponding to either M2 or M3, showing regions of different logical pad size [69].

number of layers reduces the material seen by traversing particles before reaching the calorimeters, while GEM technology is used due to the high particle flux in the inner region of the detector.

Both technologies operate in a similar fashion. Charged particles ionise electrons as they traverse the gas inside the chamber and a voltage differential accelerates the electrons to an anode. In MWPCs an electron avalanche near the anode gives a collected charge large enough to be identified above background. The MWPCs use a gas mixture of CO_2, argon and CF_4 with the ratio 55:40:5, resulting in a fast readout time. The anode wires are 30 µm in diameter and constructed from gold-plated tungsten with an inter-wire spacing of 2 mm. The GEM detectors utilise a 50 µm kapton foil sandwiched between copper coils for electron multiplication. The copper has a series of small holes at a frequency of one every 140 µm. The sheets of copper are separated by a large voltage potential, resulting in an extremely high electric field at the holes ($\sim$ 100kV/ cm). The result is electron multiplication of the order 1000 which can be collected and read out.

By utilising a series of control channels, the muon identification efficiency and probability to misidentify a charged particle as a muon have been measured

using pp collision data [69]. The muon identification efficiency was measured to be $> 96\%$ ($> 98\%$) in the momentum region $> 0.8\,\text{GeV}/c$ ($> 1.7\,\text{GeV}/c$), with low hadron misidentification in all regions (see Figure 2.14 for further details). The majority of muon misidentifications come from the decay of pions and kaons in flight, which is why the misidentification probability is higher at low momentum.

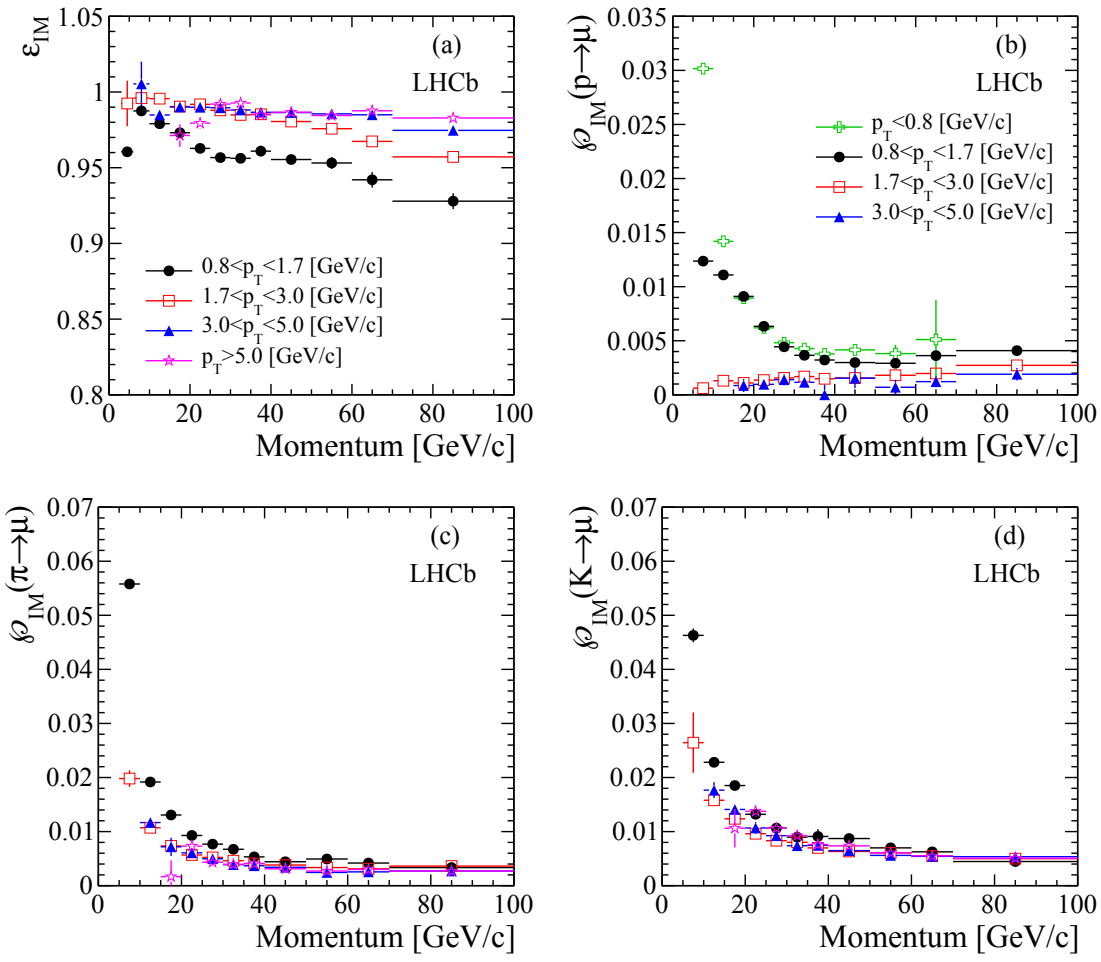

Figure 2.14: Muon identification efficiency (a) and misidentification probabilities for $p \to \mu$ (b), $\pi \to \mu$ (c) and $K \to \mu$ (d) as a function of momentum for different transverse momenta [69].

2.5 Trigger

The LHC is designed to provide a bunch crossing rate of up to 40 MHz. Of this roughly 11 MHz of inelastic collisions enter the LHCb acceptance. Due to bandwidth, CPU and hardware constraints it is impossible to process and record all of this information. The trigger reduces the input data rate to manageable levels whilst retaining interesting physics events with a high efficiency. The first stage of the trigger is hardware based and referred to as the Level-0 (L0) trigger. It operates synchronously with the 40 MHz bunch crossing rate and uses custom electronics to reduce the data rate from 11 MHz to 1 MHz. The High-Level Trigger (HLT) is software based and operates asynchronously from the LHC bunch crossings. The trigger is divided into two stages, HLT1 and HLT2, and further reduces the data rate to $\sim$3 kHz which is read out to storage for later analysis [70].

2.5.1 Hardware trigger

The first stage of the trigger is required to make fast decisions about the quality of an event, deciding if it contains enough interesting information for further processing. The decay products of heavy particles such as b hadrons typically have large transverse energy with respect to the beam axis. The L0 trigger is hardware based and looks for high transverse energy (E_{T}) in the calorimeter or high p_{T} in the muon stations as a sign of potentially important events.

To evaluate the trigger decision, the calorimeter tiles are grouped into 2×2 squares and the energy within summed. This arrangement ensures that most of the energy of a single particle is contained within the group and minimises the overlap with other particles. The energy deposited is associated to hadrons, electrons or photons using the full suite of detectors in the calorimeter system. The candidate with the highest E_{T} from each category (electron, hadron or photon) is then retained or rejected depending on preset energy thresholds. For hadrons the threshold is typically 3.5 GeV while for clusters in the ECAL the threshold is 2.5 GeV [70]. In addition, to preserve bandwidth and processing power the SPD is used to identify and veto events with large charged particle multiplicity. In 2011 events with more than 600 SPD hits were rejected [70].

As many decays involving muons are interesting and their signature in the

detector is rather striking, the muon system is an obvious choice to make up the second part of the L0 trigger. Hits are seeded in the third muon station, M3, and a straight line extrapolation is made to the interaction point. A track is made if hits are found within a customisable field of interest around the expected hit position in each of the muon stations. Hits in the first and second muon station are used to calculate the muon p_{T} to a precision of $\sim 20\%$. The single muon p_{T} threshold is $1.2\,\mathrm{GeV}/c$ while for pairs of muons it is a combined p_{T} of more than $1\,\mathrm{GeV}/c$. The two highest p_{T} muons in each quadrant of the detector are selected and this information along with the clusters from the calorimeters are passed to the L0 Decision Unit (DU).

The L0 DU uses an algorithm to combine information from the calorimeters and muon systems to make a decision on whether an event should be accepted or rejected. This decision is passed to the readout supervisor which also has information on the available buffer size, any calibration triggers which are being run and the minimum bias trigger rate. Depending on the current trigger rate, the readout supervisor can then veto or accept the event.

2.5.2 Software trigger

The LHCb High-Level trigger (HLT) runs on a large computing farm known as the Event Filter Farm which consists of roughly 2000 nodes. The trigger is written in C++ which makes it a powerful and flexible system that can react to changes in physics priority and beam conditions. The HLT makes use of a large part of the total event information to improve the fraction of interesting physics content while reducing the rate coming from the L0 trigger to 3 kHz.

The HLT has two stages. The first stage, HLT1, confirms the L0 trigger decision by reconstructing tracks in the VELO and tracking stations and matching these tracks to clusters in the calorimeter or hits in the muon station. If the cluster comes from a neutral particle such as a photon then HLT1 ensures this cannot be matched to a charged track.

The second stage, HLT2, applies inclusive and exclusive selections to provide highly b- and c-flavour enriched samples. Loose cuts on impact parameter and momentum are used to select tracks which are combined into composite particles such as $J/\psi \to \mu^+\mu^-$ or $\phi \to K^+K^-$. These composite particles are used for all further selections to avoid duplication in the creation of final states. The final

trigger is a logical OR of the inclusive and exclusive selections.

2.6 LHCb software suite

The LHCb software suite is built around the GAUDI framework [71, 72]. It comprises software specialised for each stage of data analysis with individual components detailed below [73]:

- GAUSS - Used for the generation of simulated data. PYTHIA 6.4 [74] is used to generate pp collisions with a specific LHCb configuration [75]. EVTGEN [76] is used to describe the decays of b and c hadrons, while PHOTOS [77] is used to generate final-state radiation. The interaction of the generated particles with the detector and its response are implemented using the GEANT4 toolkit [78] as described in Ref. [79].

- BOOLE - Takes as input simulated data and simulates the detector response and digitisation. Produces data which is in the same form as that from the detector data acquisition and electronics.

- MOORE - Applies the HLT to data or simulated data, also applies the L0 trigger to the latter (see Sec. 2.5).

- BRUNEL - Fully reconstructs data or simulated data by considering hits in the tracking system or muon stations and energy deposits in the calorimeter. It also provides information on particle identification via the RICH and muon systems.

- DAVINCI - Provides offline data selection and analysis; for example, by searching for vertices using BRUNEL tracks and using these tracks, together with energy deposits, to create particles.

Chapter 3

Phenomenology of $B^0 \to \phi K^*(892)^0$

3.1 Motivation

Studies of b-hadron decays provide powerful tests of the validity of the Standard Model. In particular, neutral B-meson flavour oscillations and decays involving loop/box diagrams are sensitive to new particles entering in the loop.

In this chapter the motivation for studying the decay $B^0 \to \phi K^{*0}$ [†] is discussed. The functional form of the angular and mass distributions are also shown. This forms a basis for the angular analysis discussed in Chapter 4. The results of this analysis are presented in Chapter 5 with future prospects discussed in Chapter 6.

3.1.1 CP violation

The total amount of measured *CP* violation is not enough to account for the matter-antimatter asymmetry in the Universe. Therefore, in order to increase our understanding of the Universe it is important to search for new sources of *CP* violation.

Flavour-changing neutral-current (FCNC) transitions such as $\overline{b} \to \overline{s}s\overline{s}$ are forbidden at tree level in the Standard Model and can only proceed via a loop diagram such as in Figure 3.1. Particles suggested by new physics models may be virtually produced in these loops [80]. In such a case the phase or

[†] In this analysis K^{*0} is defined as $K^*(892)^0$, unless otherwise stated.

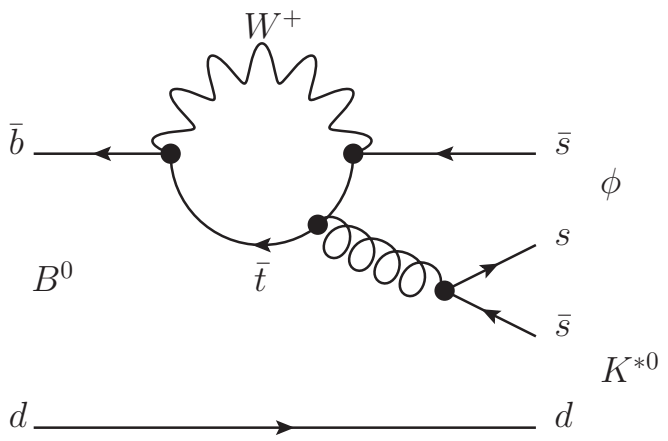

Figure 3.1: Leading order Feynman diagram for the $\bar{b} \to \bar{s}s\bar{s}$ transition $B^0 \to \phi K^{*0}$.

coupling strength at the vertices of the corresponding Feynman diagram would be altered, manifesting itself as a divergence from Standard Model expectations. Examples of observables which could be affected include the branching fraction, the polarisation or the amount of *CP* violation in the decay.

One such decay mode which can be used to investigate $\bar{b} \to \bar{s}s\bar{s}$ transitions is $B^0 \to \phi K^{*0}$. No evidence of *CP* violation has so far been observed in this mode [81–86]. Further details on previous measurements of this decay mode are provided in Section 3.4.

3.1.2 Polarisation puzzle

The decay $B^0 \to \phi K^{*0}$ is a pseudoscalar to vector-vector ($P \to VV$) transition. Therefore, due to angular momentum conservation there are a total of three possible spin configurations for the ϕK^{*0} pair. These are described by the helicity amplitudes H_{+1}, H_0, H_{-1}. It is convenient to write these amplitudes in the transversity basis as the transversity amplitudes have definite *CP* transformations. The following relates the amplitudes in the transversity and

helicity bases

$$A_\perp = \frac{H_{+1} - H_{-1}}{\sqrt{2}}\,, \tag{3.1}$$

$$A_\parallel = \frac{H_{+1} + H_{-1}}{\sqrt{2}}\,, \tag{3.2}$$

$$A_0 = H_0, \tag{3.3}$$

where A_0 and $A_\parallel$ are *CP*-even and $A_\perp$ is *CP*-odd. The polarisations are represented visually in Figure 3.2.

In the Standard Model the W-boson couples only to left-handed particles (or right-handed antiparticles). For $\overline{b} \to \overline{s}$ transitions, such as in $B^0 \to \phi K^{*0}$, this leads to the naive expectation that the $\overline{s}$ quark has helicity $+\frac{1}{2}$. The resulting ϕ meson can have helicity $+1$ or 0, but not -1. Due to helicity conservation in the strong force the $\overline{s}$ quark from the K^{*0} and the s quark from the ϕ must have opposite spin. Additionally, angular momentum conservation states that the ϕ and K^{*0} should have the same helicity. These expectations can be altered as weak decays of heavy quarks can undergo a spin flip, changing from $+\frac{1}{2}$ to $-\frac{1}{2}$ helicity or vice-versa. This is suppressed by $\sim m_s/m_b$ where $m_{s(b)}$ is the mass of the $s(b)$ quark. The previous statements lead to the following naive expectation of the helicity amplitude hierarchy, $H_0 \gg H_{+1} \gg H_{-1}$ or $A_0 \gg A_\perp$ in the transversity basis, where $A_\perp \simeq A_\parallel$ [87]. This hierarchy is evident in tree-dominated $P \to VV$ decays such as $B^0 \to \rho^+\rho^-$ and $B^0 \to D^{*-}\rho^+$ [88, 89]. However, the expectation of dominant longitudinal polarisation is not observed in penguin dominated decay modes such as $B^0 \to \phi K^{*0}$ and $B^0 \to K^{*0}\rho^0$ [83, 86, 90, 91].

This is sometimes known as the "Polarisation Puzzle" and has led to suggestions of new physics by some [92–94], while others have attributed this discrepancy to final-state interaction effects [95–97]. It has been argued that final-state interactions alone cannot reduce the longitudinal fraction to the value seen in data [98] and contributions from penguin annihilation processes, such as those suggested in Ref. [99], must also be included. More recent calculations based on QCD factorisation give polarisation fractions similar to those seen in data, however these suffer from extremely large uncertainties [50, 95].

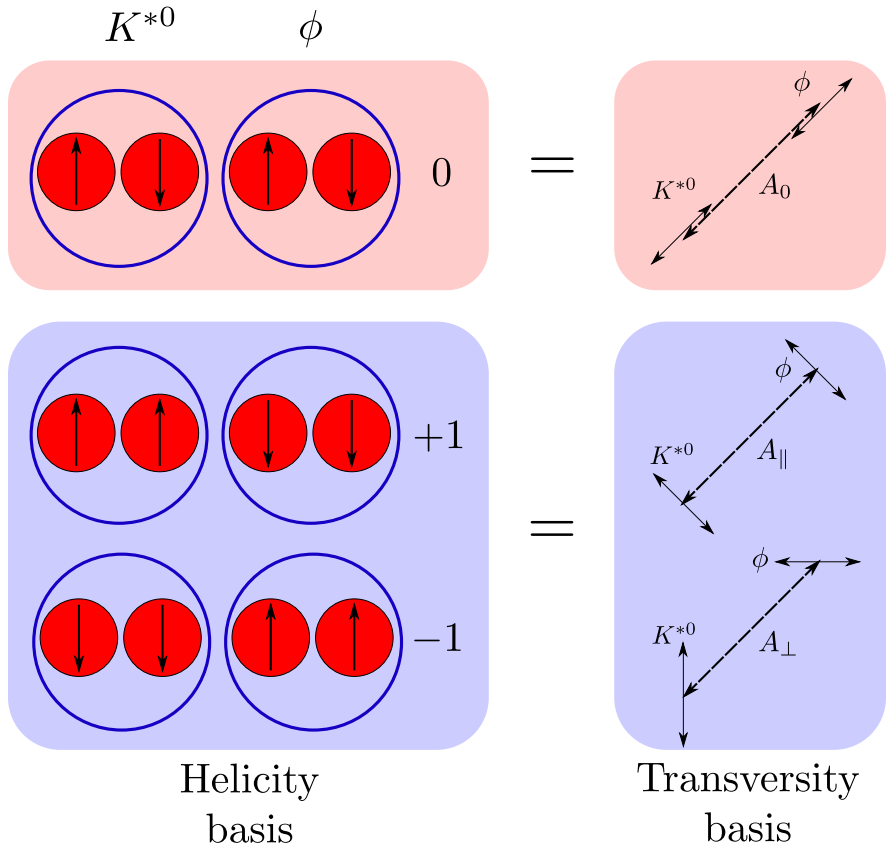

Figure 3.2: Possible spin configurations for $P \to VV$ decays in the helicity and transversity bases. In the helicity basis the arrows represent the relative direction of the quark spin components while in the transversity basis the arrows represent the spin vectors of the K^{*0} and ϕ mesons relative to one another.

3.2 Differential decay rate

In $P \to VV$ decays such as $B^0 \to \phi K^{*0}$ an angular analysis is needed to measure the *CP*-even and *CP*-odd fractions. This is necessary in order to look for *CP* violation in the polarisation amplitudes. Section 3.2.1 discusses the angular distribution of the decay rate while Section 3.2.2 shows the models used to describe the mass distributions.

3.2.1 Angular distributions

Decays involving $P \to VV$ transitions have final states which are a superposition of three spin states. Each of these has a known angular distribution which can

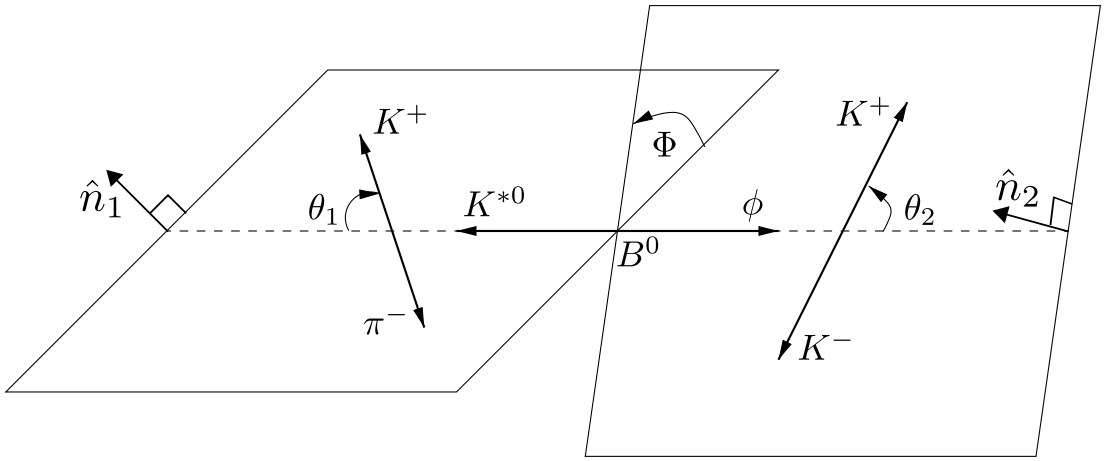

Figure 3.3: Definition of the decay angles for $B^0 \to \phi K^{*0}$ in the helicity basis.

be separated using a statistical analysis. The amplitude for a generic $P \to V_1 V_2$ decay is written [100–102]

$$\mathcal{A}(P \to V_1 V_2) = A_0 \epsilon^{*L}_{V_1} \epsilon^{*L}_{V_2} - \frac{A_\parallel}{\sqrt{2}} \vec{\epsilon^{*T}_{V_1}} \cdot \vec{\epsilon^{*T}_{V_2}} - i \frac{A_\perp}{\sqrt{2}} \vec{\epsilon^{*}_{V_1}} \times \vec{\epsilon^{*}_{V_2}} \cdot \hat{\mathbf{p}} \,, \tag{3.4}$$

where $\vec{\epsilon_{V_i}}$ is the unit polarisation of V_i (for $i = 1, 2$), $\hat{\mathbf{p}}$ is the unit vector along the direction of motion of V_2 in the rest frame of V_1. The longitudinal polarisation vector can be written $\epsilon^{*L}_{V_i} \equiv \vec{\epsilon^{*}_{V_i}} \cdot \hat{\mathbf{p}}$ and the transverse as $\vec{\epsilon^{*T}_{V_i}} \equiv \vec{\epsilon^{*}_{V_i}} - \epsilon^{*L}_{V_i} \hat{\mathbf{p}}$. From this, it is clear that the A_0 polarisation is when both particles have longitudinal polarisation with respect to the momentum vector of V_2. The amplitudes $A_\parallel$ and $A_\perp$ correspond to spin vectors transverse to the momentum vector of V_2, in the former the spin vectors are collinear to one another and in the latter they are orthogonal.

All of the amplitudes are *CP*-even, however the term proportional to $A_\perp$ is *CP*-odd due to the odd power of $\hat{\mathbf{p}}$. Therefore, the overall A_0 and $A_\parallel$ parts are *CP*-even while the $A_\perp$ part is *CP*-odd.

Each amplitude is a complex number with a *CP*-conserving strong phase δ_i and a *CP*-violating weak phase γ_i

$$A_0 = |A_0| e^{i(\delta_0 + \gamma_0)} \,, \tag{3.5}$$

$$A_\perp = |A_\perp| e^{i(\delta_\perp + \gamma_\perp)} \,, \tag{3.6}$$

$$A_\parallel = |A_\parallel| e^{i(\delta_\parallel + \gamma_\parallel)} \,. \tag{3.7}$$

In the Standard Model it is assumed that the weak phases of the amplitudes are equal *i.e.* $\gamma_0 = \gamma_\perp = \gamma_\parallel$. The *CP*-conjugate decay has the following amplitudes

$$\overline{A}_0 = |\overline{A}_0| e^{i(\overline{\delta}_0 - \gamma_0)} , \tag{3.8}$$

$$\overline{A}_\perp = |\overline{A}_\perp| e^{i(\overline{\delta}_\perp - \gamma_\perp)} , \tag{3.9}$$

$$\overline{A}_\parallel = |\overline{A}_\parallel| e^{i(\overline{\delta}_\parallel - \gamma_\parallel)} . \tag{3.10}$$

The *CP*-conserving phase comes from strong interactions, for instance between final-state particles. The *CP*-violating phase comes from weak interactions and is associated with elements of the CKM matrix. It should be noted that even though the weak phase in the conjugate amplitudes changes sign, this is not direct *CP* violation as a difference in both strong and weak phases is needed, as discussed in Sec. 1.5.1. *CP* violation can however manifest itself from the interference of strong and weak phases as discussed in Sec 3.3.

The angles between the decay products are defined in the helicity basis as shown in Figure 3.3. The angles are determined in the rest frame of the B^0. In this notation, θ_1 is the angle between the K^{*0} momentum vector and its daughter K^+ momentum vector. Similarly, θ_2 is the angle between the ϕ momentum vector and the daughter K^+ momentum vector. The angle between the vectors normal to the decay planes is denoted Φ.

In cases where both vectors decay to pseudoscalars, as is the case for $B^0 \to \phi(\to K^+K^-)K^{*0}(\to K^+\pi^-)$, the differential decay rate can be written as follows [103, 104]

$$\begin{aligned}
\frac{8\pi}{9}\frac{\mathrm{d}^3\Gamma(B^0 \to \phi K^{*0})}{\mathrm{d}\cos\theta_1 \mathrm{d}\cos\theta_2 \mathrm{d}\Phi} &= |A_0|^2 \cos^2\theta_1 \cos^2\theta_2 \\
&+ \frac{|A_\perp|^2}{4} \sin^2\theta_1 \sin^2\theta_2 (1 + \cos 2\Phi) \\
&+ \frac{|A_\parallel|^2}{4} \sin^2\theta_1 \sin^2\theta_2 (1 - \cos 2\Phi) \\
&- \frac{1}{2}\mathcal{I}m(A_\perp A_\parallel^*) \sin^2\theta_1 \sin^2\theta_2 \sin 2\Phi \\
&+ \frac{1}{2\sqrt{2}}\mathcal{R}e(A_\parallel A_0^*) \sin 2\theta_1 \sin 2\theta_2 \cos\Phi \\
&- \frac{1}{2\sqrt{2}}\mathcal{I}m(A_\perp A_0^*) \sin 2\theta_1 \sin 2\theta_2 \sin\Phi .
\end{aligned} \tag{3.11}$$

The imaginary terms change sign for the *CP*-conjugate $\overline{B}$ decay

$$\begin{aligned}
\frac{8\pi}{9}\frac{\mathrm{d}^3\Gamma(\overline{B}^0\to\phi\overline{K}^{*0})}{\mathrm{d}\cos\theta_1\mathrm{d}\cos\theta_2\mathrm{d}\Phi} &= |\overline{A}_0|^2\cos^2\theta_1\cos^2\theta_2 \\
&+ \frac{|\overline{A}_\perp|^2}{4}\sin^2\theta_1\sin^2\theta_2(1+\cos 2\Phi) \\
&+ \frac{|\overline{A}_\parallel|^2}{4}\sin^2\theta_1\sin^2\theta_2(1-\cos 2\Phi) \\
&+ \frac{1}{2}\mathcal{I}m(\overline{A}_\perp\overline{A}_\parallel^*)\sin^2\theta_1\sin^2\theta_2\sin 2\Phi \\
&+ \frac{1}{2\sqrt{2}}\mathcal{R}e(\overline{A}_\parallel\overline{A}_0^*)\sin 2\theta_1\sin 2\theta_2\cos\Phi \\
&+ \frac{1}{2\sqrt{2}}\mathcal{I}m(\overline{A}_\perp\overline{A}_0^*)\sin 2\theta_1\sin 2\theta_2\sin\Phi\ . \qquad (3.12)
\end{aligned}$$

The $K^+K^-K^+\pi^-$ final state has contributions from both scalar (S) and vector (V) resonances. In this analysis $P\to VV$, $P\to VS$ and $P\to SV$ decays are considered, which are separated by studying their kinematic distributions.

Including scalar contributions (S-wave) into the differential decay rate requires modifying Equations 3.11 and 3.12 to include additional amplitudes which describe the scalar fraction. These are denoted $A_{\mathrm{S}}^{K\pi}$ and A_{S}^{KK} in reference to the scalar contribution coming from either the $K\pi$ or KK pair.

The contribution from higher spin resonances is assumed to be negligible at the $K\pi$ and KK masses under study (see Section 4.2 for data selection). This is due to the narrow widths and high masses of these states, *e.g.* $K_2^*(1430)^0$ has a mean of $\approx 1430\,\mathrm{MeV}/c^2$ and a width of $\approx 100\,\mathrm{MeV}/c^2$ [10].

Introducing these S-wave amplitudes and their associated interference adds nine terms to Equations 3.11 and 3.12. At this point it becomes useful to rewrite Equations 3.11 and 3.12, including S-wave contributions, as a sum of terms

$$\frac{8\pi}{9}\frac{\mathrm{d}^3\Gamma(B^0\to\phi K^{*0})}{\mathrm{d}\cos\theta_1\mathrm{d}\cos\theta_2\mathrm{d}\Phi} = \sum_{i=1}^{15} K_i\ f_i(\theta_1,\theta_2,\Phi)\ , \qquad (3.13)$$

and similarly for the $\overline{B}^0$-decay, where K_i are functions of the polarisation amplitudes and f_i are the angle dependent terms. These terms are written explicitly in Table 3.1 which also introduces mass dependent terms, these are the topic of the next section.

The rate is normalised separately for the $\overline{B}^0$ and B^0 decays such that the P- and S-wave fractions are

$$F_{\rm P} = |A_0|^2 + |A_\parallel|^2 + |A_\perp|^2 \,, \quad F_{\rm S} = |A_{\rm S}^{K\pi}|^2 + |A_{\rm S}^{KK}|^2 \,, \quad F_{\rm P} + F_{\rm S} = 1 \,, \quad (3.14)$$

and

$$\overline{F}_{\rm P} = |\overline{A}_0|^2 + |\overline{A}_\parallel|^2 + |\overline{A}_\perp|^2 \,, \quad \overline{F}_{\rm S} = |\overline{A}_{\rm S}^{K\pi}|^2 + |\overline{A}_{\rm S}^{KK}|^2 \,, \quad \overline{F}_{\rm P} + \overline{F}_{\rm S} = 1 \,. \quad (3.15)$$

3.2.2 Mass distributions

Equations 3.11, 3.12, 3.13 are written as a function of helicity angles only. This is an incomplete description of the decay rate as the amplitudes are also strictly a function of the resonance masses $m_{K\pi}$ and m_{KK}. The resonance line shapes are parameterised the same for the three P-wave amplitudes. Thus, when only the P-wave amplitudes are considered the mass dependence decouples from the angular functions. This decoupling breaks when S-wave amplitudes are introduced, specifically the interference between the P-wave and S-wave terms have an explicit mass dependence. The phase difference between P- and S-wave contributions varies with mass across the P-wave resonance. To account for this, Equation 3.13 gains a mass dependent part for each term and is rewritten

$$\frac{{\rm d}^5\Gamma}{{\rm d}\cos\theta_1 {\rm d}\cos\theta_2 {\rm d}\Phi {\rm d}m_{KK} {\rm d}m_{K\pi}} =$$
$$N \sum_{i=1}^{15} K_i \; f_i(\theta_1, \theta_2, \Phi) \; \mathcal{M}_i(m_{K\pi}, m_{KK}) {\rm d}\Phi_4(K, K, K, \pi) \,, \quad (3.16)$$

where N is a normalisation constant, K_i are the polarisation amplitudes, f_i are the angle dependent terms, $\mathcal{M}_i$ are the mass dependent terms and ${\rm d}\Phi_4$ is a four-body phase space factor. These terms are written explicitly in Table 3.1 and explained in further detail in the following sections.

i	h_i	$f_i(\theta_1, \theta_2, \Phi)$	$\mathcal{M}_i(m_{K\pi}, m_{KK})$
1	$\lvert A_0\rvert^2$	$\cos\theta_1^2 \cos\theta_2^2$	$\lvert M_1(m_{K\pi})\rvert^2 \lvert M_1(m_{KK})\rvert^2$
2	$\lvert A_\parallel\rvert^2$	$\frac{1}{4}\sin\theta_1^2 \sin\theta_2^2(1+\cos(2\Phi))$	$\lvert M_1(m_{K\pi})\rvert^2 \lvert M_1(m_{KK})\rvert^2$
3	$\lvert A_\perp\rvert^2$	$\frac{1}{4}\sin\theta_1^2 \sin\theta_2^2(1-\cos(2\Phi))$	$\lvert M_1(m_{K\pi})\rvert^2 \lvert M_1(m_{KK})\rvert^2$
4	$\lvert A_\perp\rvert\lvert A_\parallel^*\rvert e^{i(\delta_\perp-\delta_\parallel)}$	$-\frac{1}{2}\sin\theta_1^2 \sin\theta_2^2 \sin(2\Phi)$	$\lvert M_1(m_{K\pi})\rvert^2 \lvert M_1(m_{KK})\rvert^2$
5	$\lvert A_\parallel\rvert\lvert A_0^*\rvert e^{i\delta_\parallel}$	$\sqrt{2}\cos\theta_1 \sin\theta_1 \cos\theta_2 \sin\theta_2 \cos\Phi$	$\lvert M_1(m_{K\pi})\rvert^2 \lvert M_1(m_{KK})\rvert^2$
6	$\lvert A_\perp\rvert\lvert A_0^*\rvert e^{i\delta_\perp}$	$-\sqrt{2}\cos\theta_1 \sin\theta_1 \cos\theta_2 \sin\theta_2 \sin\Phi$	$\lvert M_1(m_{K\pi})\rvert^2 \lvert M_1(m_{KK})\rvert^2$
7	$\lvert A_S^{K\pi}\rvert^2$	$\frac{1}{3}\cos\theta_2^2$	$\lvert M_0(m_{K\pi})\rvert^2 \lvert M_1(m_{KK})\rvert^2$
8	$\lvert A_\parallel\rvert\lvert A_S^{*K\pi}\rvert e^{i(\delta_\parallel-\delta_S^{K\pi})}$	$\frac{\sqrt{6}}{3}\sin\theta_1 \cos\theta_2 \sin\theta_2 \cos\Phi$	$\lvert M_1(m_{KK})\rvert^2 M_1(m_{K\pi}) M_0^*(m_{K\pi})$
9	$\lvert A_\perp\rvert\lvert A_S^{*K\pi}\rvert e^{i(\delta_\perp-\delta_S^{K\pi})}$	$-\frac{\sqrt{6}}{3}\sin\theta_1 \cos\theta_2 \sin\theta_2 \sin\Phi$	$\lvert M_1(m_{KK})\rvert^2 M_1(m_{K\pi}) M_0^*(m_{K\pi})$
10	$\lvert A_0\rvert\lvert A_S^{*K\pi}\rvert e^{-i\delta_S^{K\pi}}$	$\frac{2}{\sqrt{3}}\cos\theta_1 \cos\theta_2^2$	$\lvert M_1(m_{KK})\rvert^2 M_1(m_{K\pi}) M_0^*(m_{K\pi})$
11	$\lvert A_S^{KK}\rvert^2$	$\frac{1}{3}\cos\theta_1^2$	$\lvert M_0(m_{KK})\rvert^2 \lvert M_1(m_{K\pi})\rvert^2$
12	$\lvert A_\parallel\rvert\lvert A_S^{*KK}\rvert e^{i(\delta_\parallel-\delta_S^{KK})}$	$\frac{\sqrt{6}}{3}\sin\theta_1 \cos\theta_1 \sin\theta_2 \cos\Phi$	$\lvert M_1(m_{K\pi})\rvert^2 M_1(m_{KK}) M_0^*(m_{KK})$
13	$\lvert A_\perp\rvert\lvert A_S^{*KK}\rvert e^{i(\delta_\perp-\delta_S^{KK})}$	$-\frac{\sqrt{6}}{3}\sin\theta_1 \cos\theta_1 \sin\theta_2 \sin\Phi$	$\lvert M_1(m_{K\pi})\rvert^2 M_1(m_{KK}) M_0^*(m_{KK})$
14	$\lvert A_0\rvert\lvert A_S^{*KK}\rvert e^{-i\delta_S^{KK}}$	$\frac{2}{\sqrt{3}}\cos\theta_1^2 \cos\theta_2$	$\lvert M_1(m_{K\pi})\rvert^2 M_1(m_{KK}) M_0^*(m_{KK})$
15	$\lvert A_S^{K\pi}\rvert\lvert A_S^{*KK}\rvert e^{i(\delta_S^{K\pi}-\delta_S^{KK})}$	$\frac{2}{3}\cos\theta_1 \cos\theta_2$	$M_1(m_{KK}) M_0(m_{K\pi}) M_0^*(m_{KK}) M_1^*(m_{K\pi})$

Table 3.1: Definition of the h_i, f_i and $\mathcal{M}_i$ terms in Eqn. 3.13. Note that the P-wave interference terms $i = 4$ and $i = 6$ take the imaginary parts of $A_\perp A_\parallel^*$ and $A_\perp A_0^*$, while $i = 5$ takes the real part of $A_\parallel A_0^*$. Similarly the S-wave interference terms $i = 9$ and $i = 13$ take the imaginary parts of $A_\perp A_S^* M_1 M_0^*$, and the terms $i = 8, 10, 12, 14$ take the real parts of $A_\parallel A_S^* M_1 M_0^*$ and $A_0 A_S^* M_1 M_0^*$.

The Kπ P-wave

The $K\pi$ P-wave mass amplitude $M_1(m_{K\pi})$ is parameterised by a relativistic spin-1 Breit-Wigner [83] (see the section "Dalitz Plot Analysis Formalism" in [10]),

$$M_1(m_{K\pi}) = N\frac{m_{K\pi}}{q}R_1(m_{K\pi}) \ , \tag{3.17}$$

where $R_1(m_{K\pi})$ is a spin-1 relativistic Breit-Wigner

$$R_1(m_{K\pi}) = \frac{m_{K^*}\Gamma(m_{K\pi})}{(m_{K^*})^2 - m_{K\pi}^2 - im_{K^*}\Gamma_1(m_{K\pi})} \ , \tag{3.18}$$

and m_{K^*} is the K^{*0} resonance mass, $m_{K\pi}$ is the measured $K\pi$ mass and N is a complex constant which normalises the amplitude in the mass range under study. The momentum of a daughter particle in the resonance rest frame is denoted

$$q(m, m_A, m_B) = \frac{\sqrt{(m^2 - (m_A + m_B)^2)(m^2 - (m_A - m_B)^2)}}{2m} \ , \tag{3.19}$$

where m is the mass of a particle with daughter masses m_A and m_B. The mass dependent width $\Gamma(m_{K\pi})$ is given by

$$\Gamma(m_{K\pi}) = \Gamma_{K^*}\left[\frac{m_{K^*}}{m_{K\pi}}\right]\left[\frac{1 + r^2q(m_{K^*}, m_K, m_\pi)^2}{1 + r^2q(m_{K\pi}, m_K, m_\pi)^2}\right]\left[\frac{q(m_{K\pi}, m_K, m_\pi)^3}{q(m_{K^*}, m_K, m_\pi)^3}\right] \ , \tag{3.20}$$

where Γ_{K^*} is the K^{*0} resonance width and r is the interaction radius [105]. The charged kaon and pion masses are given m_K and m_π, respectively. The values used for the mean and width of the K^{*0} can be found in Table 3.2.

In this analysis, Equation 3.18 uses the convention that the phase of $M_1(m_{K\pi})$ at m_{K^*} is zero. The phase of $M_0(m_{K\pi})$ is also fixed to zero at m_{K^*}, together this ensures that the measured S-wave phase is defined as the phase difference $\delta_s^{K\pi} - \delta_0$ at the resonance mean, where by convention $\delta_0 = 0$.

The KK P-wave

The KK P-wave amplitude is described in a similar way to the $K\pi$ P-wave, using a relativistic spin-1 Breit-Wigner (Equation 3.17). However, the $m_{K\pi}$ is replaced with m_{KK}, Γ_{K^*} with Γ_ϕ and m_{K^*} with m_ϕ. The values used for the mean and width can be found in Table 3.2.

	$(K\pi)_0$	$K^*(892)^0$	$(KK)_0$	$\phi(1020)$
m (MeV/c^2)	$1435 \pm 5 \pm 5$	895.81 ± 0.19	939.9 ± 6.3	1019.455 ± 0.020
Γ (MeV/c^2)	$279 \pm 6 \pm 21$	47.4 ± 0.6	-	4.26 ± 0.04
r ($\hbar c$/ GeV)	-	3.0 ± 0.5	-	3.0 ± 0.5
a (GeV^{-1})	$1.95 \pm 0.09 \pm 0.06$	-	-	-
b (GeV^{-1})	$1.76 \pm 0.36 \pm 0.67$	-	-	-
$g_{\pi\pi}$ (MeV)	-	-	199 ± 30	-
$g_{KK}/g_{\pi\pi}$	-	-	3.00 ± 0.3	-

Table 3.2: Values used for the spin dependent resonances in this analysis. The mass of the resonance is m, Γ is the width, r the interaction radius, a the scattering length and b is the effective range. The P-wave parameters are taken from Ref. [10], the $K\pi$ S-wave parameters from Ref. [106] and the KK S-wave parameters from Ref. [107].

The narrow width of the ϕ resonance (4.26 MeV/c^2 [10]) is comparable with the resolution of the reconstructed K^+K^- mass at the LHCb detector (~ 1 MeV/c^2), as seen in Figure 3.4. Therefore, to include this effect, the K^+K^- line shape is modified by convolving each term in Equation 3.16 with a Gaussian distribution. Strictly the resolution depends on the momentum of the K^+K^- pair, this is studied in Appendix A and is found to have a negligible effect.

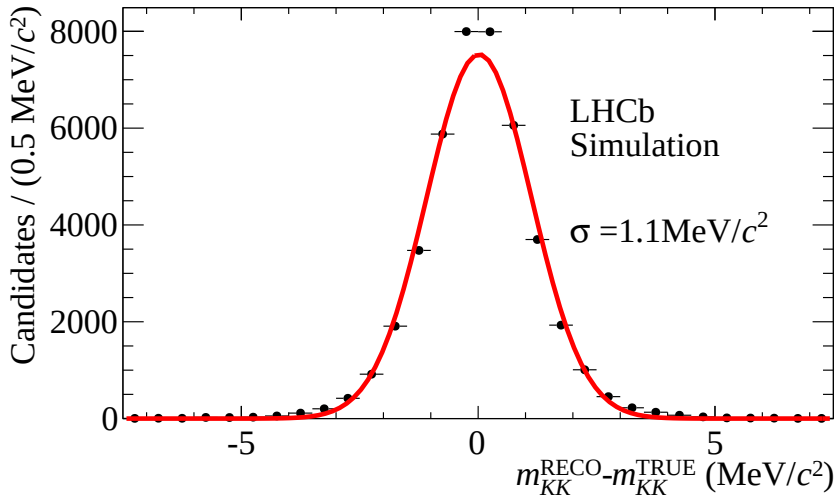

Figure 3.4: Difference between reconstructed m_{KK} ($m_{KK}^{\rm RECO}$) and true m_{KK} ($m_{KK}^{\rm TRUE}$) using simulated data. A Gaussian distribution is fit to the data, the width (σ) is taken to be the resolution on the reconstructed KK mass.

The Kπ S-wave

The $K\pi$ S-wave component, $M_0(m_{K\pi})$, is modelled using the LASS parameterisation [83,106]. This model takes the sum of a spin-0 relativistic Breit-Wigner, to model the $K_0^*(1430)$ resonance, and a non-resonant contribution. The amplitude is defined as

$$M_0(m_{K\pi}) = N\frac{m_{K\pi}}{q(m_{K\pi}, m_K, m_\pi)}\left[\frac{1}{\cot\delta_\beta - i} + e^{2i\delta_\beta}\frac{1}{\cot\delta_\alpha(m_{K\pi}) - i}\right] , \quad (3.21)$$

where N is a complex constant which normalises the distribution over the mass range and fixes the phase of the amplitude to be zero at the nominal $K^*(892)^0$ mass. The cotangent terms are defined as

$$\cot\delta_\beta = \frac{1}{aq(m_{K\pi}, m_K, m_\pi)} + \frac{1}{2}bq(m_{K\pi}, m_K, m_\pi) , \quad (3.22)$$

and

$$\cot\delta_\alpha(m_{K\pi}) = \frac{(m_{K_0^*})^2 - m_{K\pi}^2}{m_{K_0^*}\Gamma_0(m_{K\pi})} , \quad (3.23)$$

where $m_{K_0^*}$ is the nominal mass of the $K_0^*(1430)$ resonance, a is the scattering length and b is the effective range. The mass dependent width $\Gamma_0(m_{K\pi})$ is defined as

$$\Gamma_0(m_{K\pi}) = \Gamma_{K_0^*}\frac{m_{K_0^*}}{m_{K\pi}}\frac{q(m_{K\pi}, m_K, m_\pi)}{q(m_{K_0^*}, m_K, m_\pi)} , \quad (3.24)$$

where $\Gamma_{K_0^*}$ is the width of the $K_0^*(1430)$ resonance as found in Table 3.2.

The KK S-wave

The KK S-wave mass distribution is modelled using the Flatté parameterisation [108], which describes a resonance near threshold (see the section "Dalitz Plot Analysis Formalism" in [10]). The amplitude is given by

$$M_0(m_{KK}) = N\big[\frac{1}{m_{f_0}^2 - m_{KK}^2 - im_{f_0}(g_{\pi\pi}\rho_{\pi\pi} + g_{KK}\rho_{KK})}\big] , \quad (3.25)$$

where $g_{KK,\pi\pi}$ are coupling constants. A complex term N normalises the amplitude over the mass range and also fixes the phase of the amplitude to be zero at the ϕ resonance mass. The phase space terms $\rho_{KK,\pi\pi}$ are described by

$$\rho_{XX} = 2\frac{q_X}{m_{KK}} = \begin{cases} \sqrt{1-4\frac{m_X^2}{m_{KK}^2}} & m_{KK} \geq 2m_X \ , \\ \\ i\sqrt{4\frac{m_X^2}{m_{KK}^2}-1} & m_{KK} < 2m_X \ , \end{cases} \tag{3.26}$$

where $X = K, \pi$. In this analysis the values for the Flatté function are taken from Ref [107] and are shown in Table 3.2.

Four-body phase space

The four-body phase space element is given [10]

$$\mathrm{d}\Phi_4 = \frac{2}{3(2\pi)^{10} m_B} q(m_{KK}, m_K, m_K) q(m_{K\pi}, m_K, m_\pi) q(m_B, m_{K\pi}, m_{KK}) \ , \tag{3.27}$$

where m_B is the nominal B^0 meson mass.

3.3 Triple product asymmetries

Triple Product Asymmetries (TPAs) can be a useful tool in the investigation of *CP* violation [92,100,109–112]. In $B^0 \to \phi K^{*0}$ two types of TPA can be observed, so called *true* and *fake* TPAs. If significant true TPAs are observed it would be an unambiguous sign of new physics.

Triple products of momentum vectors take the form $\vec{p}_1 \times \vec{p}_2 \cdot \vec{p}_3$, which is odd under time reversal. Using the angular basis defined in Figure 3.3 two T-odd triple products can be defined [92, 110–112]

$$(\vec{n}_1 \times \vec{n}_2) \cdot \vec{p}_1 = \sin\Phi \ , \tag{3.28}$$

$$2(\vec{n}_1 \cdot \vec{n}_2)(\vec{n}_1 \times \vec{n}_2) \cdot \vec{p}_1 = \sin 2\Phi \ , \tag{3.29}$$

where $\vec{p}_1$ is a unit vector in the direction of the K^{*0} momentum in the B^0 rest frame and $\vec{n}_1$ and $\vec{n}_2$ are unit vectors normal to the decay planes of the K^{*0} and ϕ mesons, respectively. T-odd asymmetries can be written as the difference

between the number of events with positive and negative values of $U = \sin 2\Phi$ or $V = s_{\theta_1\theta_2} \sin \Phi$ where $s_{\theta_1\theta_2} = \text{sign}(\cos\theta_1 \cos\theta_2)$

$$\mathcal{A}_T^{(1)} \equiv \frac{\Gamma(U>0) - \Gamma(U<0)}{\Gamma(U>0) + \Gamma(U<0)} , \tag{3.30}$$

$$\mathcal{A}_T^{(2)} \equiv \frac{\Gamma(V>0) - \Gamma(V<0)}{\Gamma(V>0) + \Gamma(V<0)} . \tag{3.31}$$

Using this method to study the decay $K^0_{\text{L}} \to \pi^+\pi^- e^+ e^-$ a $(13.6 \pm 1.4 \pm 1.5)\%$ T-odd asymmetry was observed by the KTeV collaboration [113]. This supports earlier measurements made by the KTeV [114] and NA62 [115] collaborations and is in agreement with theoretical predictions [116–118].

Triple products can also be defined using combinations of the polarisation amplitudes and strong phases. Integrating Equation 3.11, which only contains P-wave terms, over $\cos\theta_1$ and $\cos\theta_2$ gives the following

$$\frac{\mathrm{d}\Gamma}{\mathrm{d}\Phi} = \frac{4}{9} N(|A_0|^2 + 2|A_\perp|^2 \sin^2\Phi + 2|A_\parallel|^2 \cos^2\Phi - 2\mathcal{I}m(A_\perp A_\parallel^*) \sin 2\Phi) . \tag{3.32}$$

As shown in Equation 3.29, $\sin 2\Phi$ can be used to search for a T-odd asymmetry. Considering Equations 3.30 and 3.32 produces a triple product asymmetry which is a function of polarisation amplitudes [110]

$$\mathcal{A}_T^{(1)} \equiv \frac{\Gamma(U>0) - \Gamma(U<0)}{\Gamma(U>0) + \Gamma(U<0)} \tag{3.33}$$

$$= \left[\int_0^{\pi/2} + \int_\pi^{3\pi/2}\right] (\mathrm{d}\Gamma/\mathrm{d}\Phi)\mathrm{d}\Phi - \left[\int_{\pi/2}^{\pi} + \int_{3\pi/2}^{2\pi}\right] (\mathrm{d}\Gamma/\mathrm{d}\Phi)\mathrm{d}\Phi \tag{3.34}$$

$$= -\frac{4}{\pi} \frac{\mathcal{I}m(A_\perp A_\parallel^*)}{|A_0|^2 + |A_\perp|^2 + |A_\parallel|^2} . \tag{3.35}$$

Similarly, Equation 3.31 can be written as

$$\mathcal{A}_T^{(2)} = -\frac{2\sqrt{2}}{\pi} \frac{\mathcal{I}m(A_\perp A_0^*)}{|A_0|^2 + |A_\perp|^2 + |A_\parallel|^2} . \tag{3.36}$$

Although the triple product asymmetries defined in Equations 3.30, 3.31, 3.35 and 3.36 are T-odd, they are not genuinely CP-violating. Specifically, a non-zero triple product asymmetry of this form can be the result of a difference between the strong phases of corresponding polarisation amplitudes, which are CP-conserving,

while the weak phase difference is zero.

Adding the B and $\overline{B}$ triple products

$$\mathcal{A}_{T(\text{true})} = \frac{1}{2}(A_T + \overline{A}_T) \ , \tag{3.37}$$

produces an observable which is genuinely *CP*-violating [100, 110] *i.e.* $A_T = -\overline{A}_T$ if *CP* symmetry is conserved.

If direct *CP* violation is assumed to be zero, such that

$$A_\lambda = |A_\lambda| e^{i(\delta_\lambda + \gamma_\lambda)}, \quad \overline{A}_\lambda = |A_\lambda| e^{i(\delta_\lambda - \gamma_\lambda)} \qquad (\lambda = 0, \perp, \|) \ , \tag{3.38}$$

the asymmetry is non-zero if the weak phases differ and the strong phase difference is not $\pi/2$

$$\mathcal{I}m(A_\perp A_0^*) - \mathcal{I}m(\overline{A}_\perp \overline{A}_0^*) = 2|A_\perp||A_0| \cos(\delta_\perp - \delta_0) \sin(\gamma_\perp - \gamma_0) \ . \tag{3.39}$$

This is sometimes called a *true* triple product asymmetry in contrast to *fake* triple product asymmetries which are formed from the difference in amplitudes

$$\mathcal{A}_{T(\text{fake})} = \frac{1}{2}(A_T - \overline{A}_T) \ . \tag{3.40}$$

An example of a fake asymmetry is the following

$$\mathcal{I}m(A_\perp A_0^*) + \mathcal{I}m(\overline{A}_\perp \overline{A}_0^*) = 2|A_\perp||A_0| \sin(\delta_\perp - \delta_0) \cos(\gamma_\perp - \gamma_0) \ , \tag{3.41}$$

as it can be non-zero due to strong phase differences even when the weak phase difference vanishes.

Equations 3.35 and 3.36 are then written as true and fake triple product asymmetries

$$\begin{aligned} \mathcal{A}^{(1)}_{T(\text{true})} &= \frac{1}{2}\left[\frac{\Gamma(U>0) - \Gamma(U<0)}{\Gamma(U>0) + \Gamma(U<0)} - \frac{\Gamma(\overline{U}>0) - \Gamma(\overline{U}<0)}{\Gamma(\overline{U}>0) + \Gamma(\overline{U}<0)}\right] \ , \\ &= -\frac{2}{\pi}\left[\frac{\mathcal{I}m(A_\perp A_\|^*)}{F_{\mathrm{P}}} - \frac{\mathcal{I}m(\overline{A}_\perp \overline{A}_\|^*)}{\overline{F}_{\mathrm{P}}}\right] \ , \end{aligned} \tag{3.42}$$

$$\mathcal{A}^{(1)}_{T(\text{fake})} = \frac{1}{2}\left[\frac{\Gamma(U>0)-\Gamma(U<0)}{\Gamma(U>0)+\Gamma(U<0)}+\frac{\Gamma(\overline{U}>0)-\Gamma(\overline{U}<0)}{\Gamma(\overline{U}>0)+\Gamma(\overline{U}<0)}\right],$$
$$= -\frac{2}{\pi}\left[\frac{\mathcal{I}m(A_\perp A^*_\parallel)}{F_\text{P}}+\frac{\mathcal{I}m(\overline{A}_\perp \overline{A}^*_\parallel)}{\overline{F}_\text{P}}\right], \quad (3.43)$$

and

$$\mathcal{A}^{(2)}_{T(\text{true})} = \frac{1}{2}\left[\frac{\Gamma(V>0)-\Gamma(V<0)}{\Gamma(V>0)+\Gamma(V<0)}-\frac{\Gamma(\overline{V}>0)-\Gamma(\overline{V}<0)}{\Gamma(\overline{V}>0)+\Gamma(\overline{V}<0)}\right],$$
$$= -\frac{2\sqrt{2}}{\pi}\left[\frac{\mathcal{I}m(A_\perp A^*_0)}{F_\text{P}}-\frac{\mathcal{I}m(\overline{A}_\perp \overline{A}^*_0)}{\overline{F}_\text{P}}\right], \quad (3.44)$$

$$\mathcal{A}^{(2)}_{T(\text{fake})} = \frac{1}{2}\left[\frac{\Gamma(V>0)-\Gamma(V<0)}{\Gamma(V>0)+\Gamma(V<0)}+\frac{\Gamma(\overline{V}>0)-\Gamma(\overline{V}<0)}{\Gamma(\overline{V}>0)+\Gamma(\overline{V}<0)}\right],$$
$$= -\frac{2\sqrt{2}}{\pi}\left[\frac{\mathcal{I}m(A_\perp A^*_0)}{F_\text{P}}+\frac{\mathcal{I}m(\overline{A}_\perp \overline{A}^*_0)}{\overline{F}_\text{P}}\right]. \quad (3.45)$$

The introduction of S-wave terms into the decay rate, as seen in Equation 3.16, allows the definition of two further triple products

$$\mathcal{A}^{(3)}_T = \frac{\Gamma(s_{\theta_1}\sin\Phi>0)-\Gamma(s_{\theta_1}\sin\Phi<0)}{\Gamma(s_{\theta_1}\sin\Phi>0)+\Gamma(s_{\theta_1}\sin\Phi<0)},$$
$$= -\sqrt{\frac{3}{2}}\left(\frac{\mathcal{I}m(A_\perp A^{K\pi^*}_\text{S})\int_{m^L_{K\pi}}^{m^H_{K\pi}}\mathcal{M}_1(K\pi)\mathcal{M}_0(K\pi)\text{d}m_{K\pi}}{F_\text{P}+F_\text{S}}\right), \quad (3.46)$$

and

$$\mathcal{A}^{(4)}_T = \frac{\Gamma(s_{\theta_2}\sin\Phi>0)-\Gamma(s_{\theta_2}\sin\Phi<0)}{\Gamma(s_{\theta_2}\sin\Phi>0)+\Gamma(s_{\theta_2}\sin\Phi<0)},$$
$$= -\sqrt{\frac{3}{2}}\left(\frac{\mathcal{I}m(A_\perp A^{KK^*}_\text{S})\int_{m^L_{KK}}^{m^H_{KK}}\mathcal{M}_1(KK)\mathcal{M}_0(KK)\text{d}m_{KK}}{F_\text{P}+F_\text{S}}\right), \quad (3.47)$$

where $m^{L(H)}_{K\pi,KK}$ is the lower (upper) mass limit under study and $s_{\theta_i} = sign(\cos\theta_i)$ for $i = 1, 2$. The dependence on mass is not seen in triple products which are

constructed only from P-wave terms because all P-wave terms have the same dependence on mass.

The S-wave interference terms can be written in terms of true and fake triple product asymmetries using Equations 3.37 and 3.40.

3.4 Previous measurements

The first observation of the decay $B^0 \to \phi K^{*0}$ was made by the CLEO collaboration in 2001 [119]. This was followed by branching fraction measurements and angular analyses by the Belle and BaBar collaborations [81–86]. The branching fraction as averaged by the Particle Data Group is $(9.8 \pm 0.6) \times 10^{-6}$ [10], in good agreement with theoretical predictions [50, 95].

The previous most precise angular analysis was performed by the Belle collaboration in 2013 using 1100 signal events [86]. In their analysis a statistical precision of 6% was obtained on the longitudinal fraction with a systematic uncertainty of 11%. The dominant systematic uncertainty on this measurement is due the uncertainty on the efficiency function. No evidence of *CP* violation was observed in this analysis.

Using $1\,\text{fb}^{-1}$ of collision data collected by LHCb an analysis of the decay $B^0 \to \phi K^{*0}$ has been carried out which improves upon the Belle measurement [86, 120]. The LHCb analysis is described in Chapter 4 with the results shown in Chapter 5. Chapter 6 discusses the future prospects for this decay mode.

Chapter 4

Analysis of $\mathbf{B^0 \to \phi K^*(892)^0}$

4.1 Data sample

The analysis of $B^0 \to \phi K^{*0}$ uses pp collision data corresponding to an integrated luminosity of $1\,\text{fb}^{-1}$. The data were collected at $\sqrt{s} = 7\,\text{TeV}$ in 2011 by the LHCb detector. Selection criteria are applied in the first stages of the analysis to improve the signal to background ratio.

This analysis also uses simulated data to validate the fit model (see Appendix B) and to understand the detector acceptance (see Sec. 4.5). The generation of simulated data is discussed in Sec. 2.6.

The simulation is generated with the polarisation amplitudes and phases shown in Table 4.1. These values are based on early measurements by Belle and BaBar. The simulated data does not have any $K^+\pi^-$ or K^+K^- S-wave components and the effect of this is studied in Sec. 5.3.1. Five million events are generated which are required to pass the same selection as the real data (see Sec. 4.2) after which 45550 simulated events remain. Samples of $B^0_s \to \phi\phi$, $B^0_s \to K^{*0}K^{*0}$, $\Lambda^0_b \to pKKK$ and $\Lambda^0_b \to p\pi KK$ decays are also generated as part of the systematic study of the background.

4.2 Event selection

4.2.1 Trigger selection

First, each event must pass the hardware stage of the trigger as described in Section 2.5. In this analysis two categories of events that pass the hardware trigger stage are considered: those where the signal b-hadron products are used in the trigger decision (TOS) and those where the trigger decision is based on other activity in the event (TIS) [70]. The software trigger accepts events with at least a three-track secondary vertex, where one of the particles has p_{T} greater than 1.7 GeV/c and is well separated from the primary pp interaction vertex (PV). This is accomplished by requiring that at least one particle has a χ^2_{IP} with respect to any PV greater than 16, where χ^2_{IP} is the difference in χ^2 of a given PV reconstructed with and without the additional track. A multivariate algorithm is used to further identify vertices consistent with the decay of a b quark [121].

4.2.2 Loose selection

A loose offline selection is then performed which rejects a large proportion of background but retains much of the signal. The final-state particles are required to have p_{T} greater than 500 MeV/c with a $\chi^2_{\mathrm{IP}} > 9$ for each track. To differentiate between pions and kaons in the final state, the difference in logarithms of the likelihood is taken between the kaon and pion hypotheses, $\Delta LL(K-\pi)$ [122]. The kaons from the ϕ meson are required to have $\Delta LL(K-\pi) > 0$, while the pion from the K^{*0} must have $\Delta LL(K-\pi) < 0$. In order to suppress $\pi^+\pi^-$ combinatorial background, the kaon from the K^{*0} has a tighter requirement of $\Delta LL(K-\pi) > 2$. Fake tracks created by the reconstruction, which are not

Parameter	Generated value
f_{L}	0.521
$f_{\perp}$	0.251
$\delta_{\perp}$	1.426
$\delta_{\parallel}$	1.352

Table 4.1: Polarisation amplitudes and phases used in the generation of the simulated data.

associated to actual charged particles, are suppressed using the output of a neural network trained to discriminate between these and real particles [123].

The resulting charged particles are then combined to form ϕ and K^{*0} meson candidates. The mass of the $K^+\pi^-(K^+K^-)$ pair is required to be within $\pm 150\,\mathrm{MeV}/c^2$ ($\pm 15\,\mathrm{MeV}/c^2$) of the known K^{*0} (ϕ) meson mass [10] and the p_T of the resonances is required to be greater than $900\,\mathrm{MeV}/c$. In order to suppress background from $B_s^0 \to \phi\phi$ decays where one kaon is misidentified as a pion, the $K^+\pi^-$ mass is recalculated assuming the K^+K^- hypothesis and this is required to be more than $15\,\mathrm{MeV}/c^2$ away from the known ϕ meson mass.

The ϕ and K^{*0} meson candidates are combined to form B^0 meson candidates, which are required to have mass in the range $5150 < M(KKK\pi) < 5600\,\mathrm{MeV}/c^2$. A fit of the B^0 vertex is made by requiring all four final-state particles to originate from a common vertex, the χ^2 of this fit per degree of freedom must be less than 15. The B^0 meson candidate is required to be displaced from the PV by requiring that its flight distance significance is more than five standard deviations. Finally, the B^0 meson is required to originate from the primary vertex by using the following criteria: B^0 $\chi^2_\mathrm{IP} < 5$ and the distance of closest approach between the PV and B^0 meson trajectory less than 0.3 mm, if more than one B^0 meson is found the closest to the PV is chosen. After this selection is applied approximately 8000 candidates remain, the distribution of these candidates in the B^0 mass spectrum is shown in Fig. 4.1.

4.2.3 Geometric likelihood

The background is further suppressed through the use of a multivariate technique, the geometric likelihood method (GL) [124–127]. The GL is trained on a signal sample consisting of simulated $B^0 \to \phi K^{*0}$ decays and a background sample from the upper mass sideband of the B^0 meson, $M(KKK\pi) > 5413\,\mathrm{MeV}/c^2$ and the sidebands of the ϕ meson mass, $|m_{KK} - m_\phi| > 15\,\mathrm{MeV}/c^2$. The data used for the sidebands are shown in Figure 4.2 and are not used in the subsequent analysis.

The GL takes the discriminating variables for signal and background distributions and transforms them into uncorrelated Gaussian distributions. For each event a signal and background χ^2 is calculated

$$\chi^2_\mathrm{S} = \sum S_i^2 \quad \text{and} \quad \chi^2_\mathrm{B} = \sum B_i^2 \,, \tag{4.1}$$

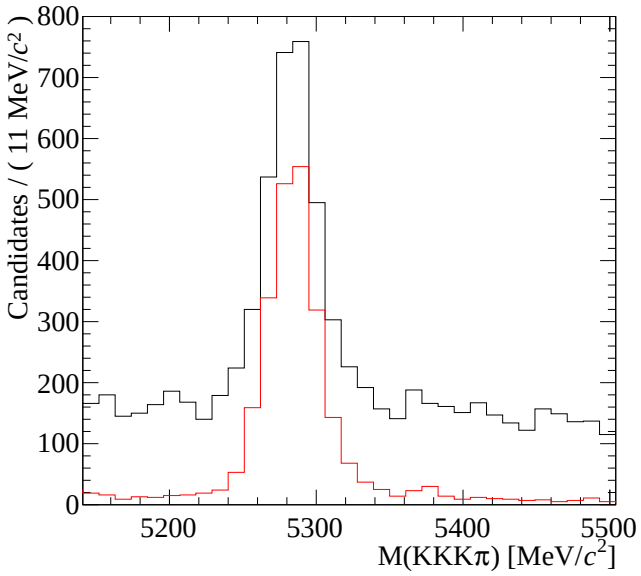

Figure 4.1: B^0 meson mass before (black lined histogram) and after (red histogram) the GL has been applied. The loose selection described in Sec. 4.2 has been performed.

where S_i and B_i are the normalised Gaussian distributions for signal and background, respectively, with mean of zero and width of one. The sum is over the i discriminating variables, of which there are six in this analysis. A new discriminating variable is created

$$\Delta\chi^2 = \chi^2_{\rm B} - \chi^2_{\rm S} \,, \tag{4.2}$$

which is transformed to be uniformly distributed between zero and one for signal; the background will then peak at zero.

The GL uses the following variables to discriminate between signal and background: the B^0 meson impact parameter with respect to the PV, the distance of closest approach between the ϕ and K^{*0} meson trajectories, the measured lifetime of the B^0 meson candidate, the $p_{\rm T}$ of the B^0 meson, the minimum $\chi^2_{\rm IP}$ of the K^+K^- pair and the minimum $\chi^2_{\rm IP}$ of the $K^+\pi^-$ pair. The figure of merit optimised by the GL is $S/\sqrt{S+B}$ where S (B) is the number of signal (background) candidates. Based on the number of candidates observed in Fig. 4.1, the GL is optimised assuming 2000 (6000) signal (background)

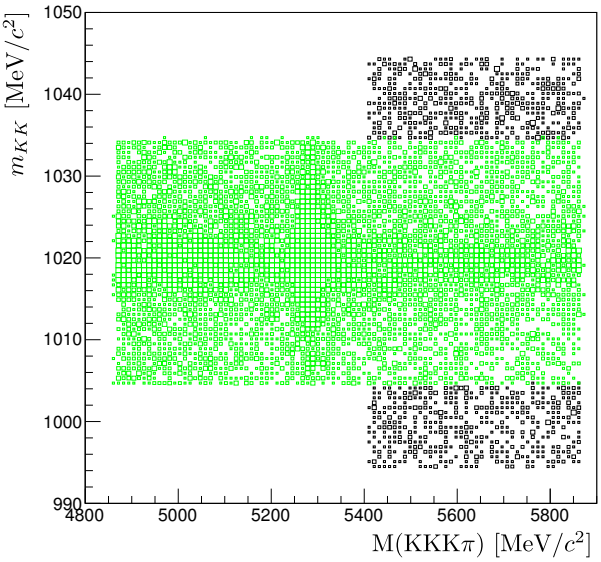

Figure 4.2: B^0 meson mass against ϕ meson mass. The data in green are used for the subsequent analysis while those in black are only used to train the GL.

candidates. The maximum value of the figure of merit is found to be 24.6 which corresponds to a GL value of greater than 0.1, as seen in Fig. 4.3. This reduces the sample size for the subsequent analysis to 1852 candidates.

4.3 Fit method

4.3.1 Maximum likelihood method

This analysis uses the maximum likelihood method to determine the physics parameters from the data. The likelihood ($\mathcal{L}$) for a set of physics parameters $\vec{\lambda}$ given a data sample with distributions w is equal to the probability density function ($\mathcal{P}$) for w given $\vec{\lambda}$ [128]

$$\mathcal{L}(\vec{\lambda}|w) = \mathcal{P}(w|\vec{\lambda}) \, . \tag{4.3}$$

The theory of maximum likelihood estimation states that the values for the physics parameters which maximise the likelihood are the most probable given the data. For computational reasons the logarithm of both sides of Eqn. 4.3 is

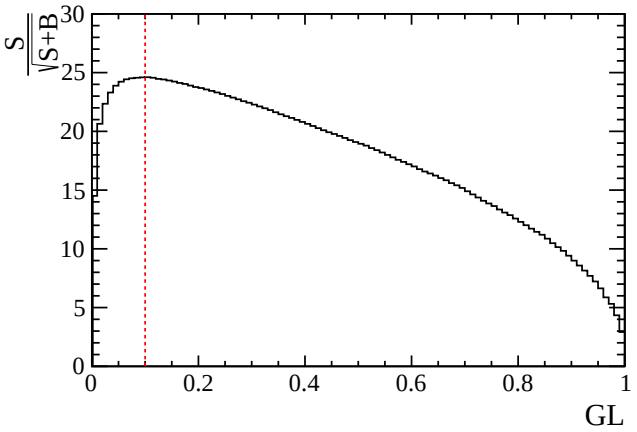

Figure 4.3: Figure of merit as a function of GL value. The GL value corresponding to the maximum value of the figure of merit is shown by a red dotted line.

typically taken. Taking the logarithm preserves the order of a function, thus finding the maximum of $\ln \mathcal{L}$ is equivalent to finding the maximum of $\mathcal{L}$. For a number of independent measurements Eqn. 4.3 can be written

$$\ln \mathcal{L} = \sum_i \ln \mathcal{P}_i(\vec{\lambda}) \ , \tag{4.4}$$

over a sum of i events. The physics parameters which maximise Eqn. 4.4 are taken to be the most likely values for that data set.

4.3.2 sPlot technique

When a data sample is populated from several sources, for example signal and background, the *sPlot* technique can be used to separate the different contributions [129]. This method defines a *discriminating* variable, x, which is different between signal and background; in this analysis the discriminating variable is the $K^+K^-K^+\pi^-$ mass. Crucially x must be independent of the variables of interest, $\vec{y}$, which in this analysis are the helicity angles and resonance masses. An extended maximum likelihood fit of the discriminating variable is used to find the number of signal and background events, $N_{\rm S}$ and $N_{\rm B}$, respectively[2].

[2]In general the *sPlot* technique can be extended to include more than two populations and used to fit more than one discriminating variable.

A signal and background weight can then be defined for each event

$$w_{\rm S}(x) = \frac{V_{\rm SB}(x) g_{\rm S}(x)}{N_{\rm S} g_{\rm S}(x) + N_{\rm B} g_{\rm B}(x)} \quad \text{and} \quad w_{\rm B}(x) = \frac{V_{\rm SB}(x) g_{\rm B}(x)}{N_{\rm S} g_{\rm S}(x) + N_{\rm B} g_{\rm B}(x)} \,, \tag{4.5}$$

where $g_{\rm S}$ ($g_{\rm B}$) is the signal (background) PDF. In general $V_{SB}(x)$ is the covariance matrix describing the different population yields, however in this example it collapses to a single number. Plotting a distribution, y_i, of the i events with signal weights $w_{\rm S}(x_i)$ reproduces the signal distribution, free from background, given the PDFs used for the discrimination are correct. The weight is then added to the likelihood from Eqn. 4.4 to perform a fit to the unfolded distribution

$$\ln \mathcal{L} = \alpha \sum_i w_{\rm S}(x_i) \ln \mathcal{P}_i(\vec{\lambda}) \,, \tag{4.6}$$

where $\alpha = \sum_i w_{\rm S}(x_i) / \sum_i w_{\rm S}(x_i)^2$ is a normalisation factor which includes the effect of the weights in the determination of the uncertainties [130, 131]

4.4 Mass fit model

To measure the signal yield a fit is made to the reconstructed mass of the $K^+K^-K^+\pi^-$ system, denoted $M(KKK\pi)$. The signal and background models are discussed in this section. Alternative models are discussed as part of the systematic uncertainty determination in Section 5.

4.4.1 Signal component

The signal contribution is modelled using the sum of Gaussian and Crystal Ball [132] functions which share a common mean. This can be written as a function of mass M

$$S(M) = (1 - f_{\rm CB}) G(M) + f_{\rm CB} CB(M) \,, \tag{4.7}$$

where $S(M)$ is the unnormalised signal model, $G(M)$ is a Gaussian distribution, $CB(M)$ is the Crystal Ball shape and $f_{\rm CB}$ is the fraction of the signal represented by the Crystal Ball function. The Gaussian and Crystal Ball functions can be

written as

$$G(M) \;=\; \exp\left(-\frac{(M-M_B)^2}{2\sigma_{\rm G}^2}\right)\,,$$

and

$$CB(M) = \begin{cases} \exp\left(\frac{(M-M_B)^2}{2\sigma_{\rm CB}^2}\right)\,, & \text{if } \frac{M-M_B}{\sigma_{\rm CB}} > -a \\ A(B-\frac{M-M_B}{\sigma_{\rm CB}})^{-n}, & \text{if } \frac{M-M_B}{\sigma_{\rm CB}} \leq -a\,, \end{cases}$$

$$\begin{aligned} A &= \left(\frac{n}{a}\right)^n \exp\left(-\frac{1}{2}|a|^2\right)\,, \\ B &= \frac{n}{|a|} - a\,, \end{aligned} \tag{4.8}$$

where M_B is the mean of the Gaussian and Crystal Ball functions and $\sigma_{\rm G}$ ($\sigma_{\rm CB}$) is the width of the Gaussian (Crystal Ball) function. The tail of the Crystal Ball function is described by n and a, where a is taken to be positive. Table 4.2 shows the values used for the fit parameters.

The results of a fit to this model are shown in Figure 4.4, using simulated $B^0 \to \phi K^{*0}$ candidates. With the exception of one bin near 5250 MeV/c^2, the pull plot is small across the mass range.

4.4.2 Background components

Main contributions

The main background component comes from random combinations of tracks not originating from a B decay, this is modelled using an exponential function.

A small contribution from $B_s^0 \to \phi\overline{K}^{*0}$ decays is expected [126]; this is included in the fit using the same model as the signal. The shape parameters are shared with the signal mode while the mean is fixed to the measured B^0 mean plus the known mass difference between the B^0 and B_s^0 mesons [10].

$\mathbf{B_s^0 \to \phi\phi}$

Backgrounds where a final-state particle has been misidentified are studied. A single kaon-pion misidentification in the decay $B_s^0 \to \phi(\to K^+K^-)\phi(\to K^+K^-)$

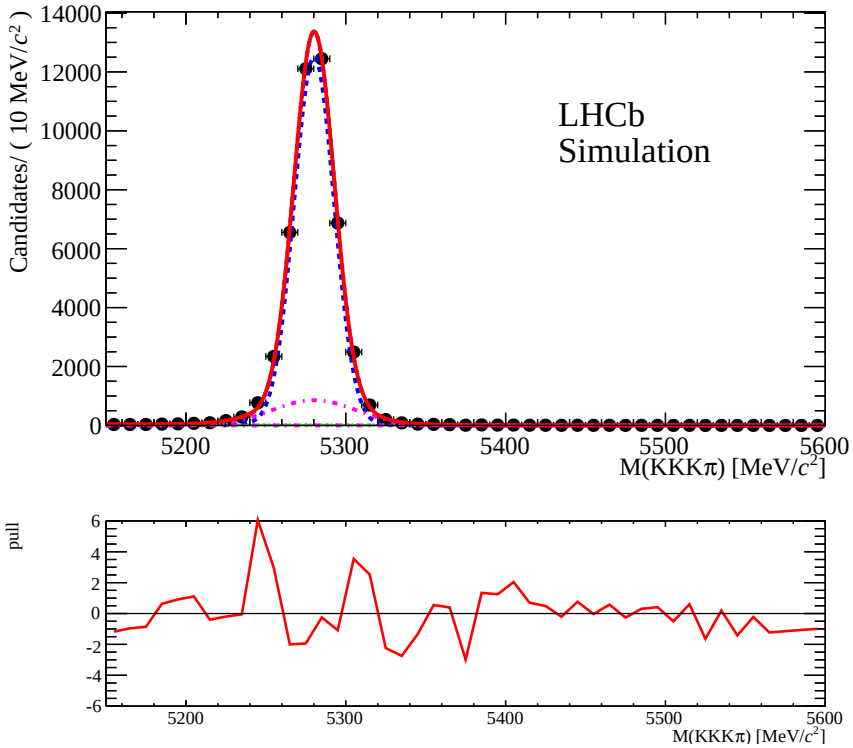

Figure 4.4: Mass distribution for simulated $B^0 \to \phi K^{*0}$ candidates. A fit to the model described in Sec. 4.4.1 is overlaid (solid red). The Crystal Ball and Gaussian contributions are shown in dashed magenta and blue, respectively. The pull distribution is shown below.

leads to the $K^+K^-K^+\pi^-$ final state. This background peaks under the B^0 mass peak as shown in Figure 4.5; as such a good understanding of this decay is needed.

The number of $B_s^0 \to \phi\phi$ events expected in data is estimated using simulation and the factor ρ relates the two samples

$$\rho = \frac{\text{Data}(\phi\phi)}{\text{MC}(\phi\phi)} \,, \tag{4.9}$$

where Data($\phi\phi$) and MC($\phi\phi$) are the number of $B_s^0 \to \phi\phi$ candidates seen in data and simulation, respectively. These are Data($\phi\phi$) $= 880 \pm 30$ [133] and MC($\phi\phi$) $= 36594 \pm 191$. Using the same $B_s^0 \to \phi\phi$ simulation sample and applying the $B^0 \to \phi K^{*0}$ selection gives MC(ϕK^*) $= 246 \pm 16$ candidates. This is scaled

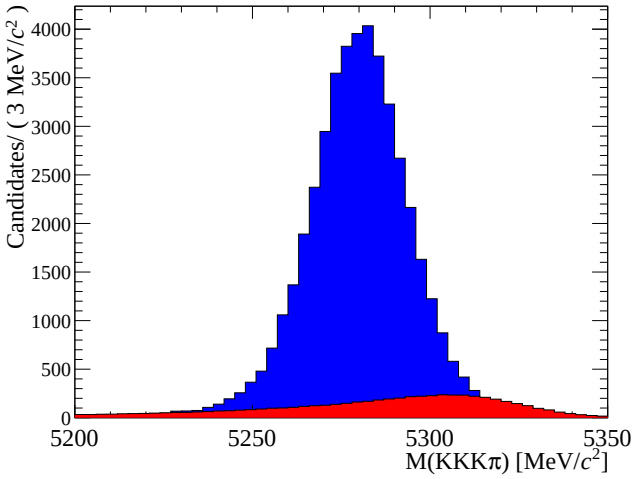

Figure 4.5: Simulated $B^0 \to \phi K^{*0}$ events (blue) overlayed with simulated $B_s \to \phi\phi$ events (red) reconstructed as $B^0 \to \phi K^{*0}$. The distributions are arbitrarily normalised.

by ρ to give the number of events expected in data

$$\text{Data}(\phi K^*) = \rho \times \text{MC}(\phi K^*) \,, \tag{4.10}$$

$$= 6 \pm 1 \,. \tag{4.11}$$

This is negligible and not included in the fit. Similarly, the decay $B_s^0 \to K^{*0}K^{*0}$ is studied and also found to be negligible.

$\mathbf{B^0 \to D_s^- K^+}$

Searches are also made for possible three-body decays in combination with a pion or kaon. Analysis of the $K^+K^-\pi^-$ mass distribution reveals a peak near the known mass of the D_s^- meson, as seen in Figure 4.6. A fit is made to the $K^+K^-\pi^-$ mass using a Gaussian distribution to model the D_s^- and a second, wider, Gaussian distribution for the background. The mean of the signal Gaussian distribution is fixed using the known D_s^- mass [10] and the width is taken from a previous LHCb measurement [134]. The fitted yield is 11 ± 4 D_s^- candidates. In Figure 4.7, events within 21 MeV/c^2 of the known D_s^- meson mass are selected and overlaid onto the full $K^+K^-K^+\pi^-$ mass spectrum together with events from the background taken between $|M(KK\pi) - m_{Ds^-}| > 21\,\text{MeV}/c^2$ and $|M(KK\pi) -$

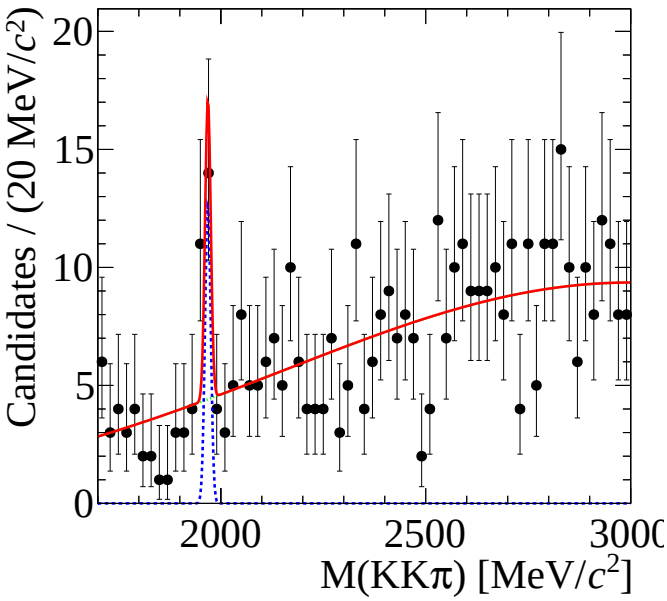

Figure 4.6: Mass of the K^+K^- from the ϕ meson combined with the π^- from the K^{*0} meson. A fit using a Gaussian distribution for the D_s^- component (blue dotted) and a second Gaussian distribution for the background (green dotted) is superimposed.

$m_{Ds^-}| < 81\,\mathrm{MeV}/c^2$ where m_{Ds^-} is the known D_s^- meson mass [10]. A small number of D_s^- candidates are observed near the B^0 peak. However, data from the D_s^- sidebands, which is formed from real K^{*0} candidates, show that the majority of the peaking component at the B^0 meson mass is from real $B^0 \to \phi K^{*0}$ candidates. As a further check, the angular analysis is repeated after applying a veto on events within $15\,\mathrm{MeV}/c^2$ of the D_s^- mass. Negligible differences are seen compared to the nominal result (see Sec. 5.3). Therefore, any contribution from $B^0 \to D_s^- K^+$ is safely ignored.

$\mathbf{\Lambda_b^0 \to p\pi^-(K^-)\phi}$

Another pair of decay modes which can peak in the signal region are $\Lambda_b^0 \to p\pi^-\phi$ and $\Lambda_b^0 \to pK^-\phi$. The former requires that a proton is misidentified as a kaon and the latter that pK^- is misidentified as $K^+\pi^-$. This is studied by generating a large sample of simulated $\Lambda_b^0 \to p\pi^-\phi$ and $\Lambda_b^0 \to pK^-\phi$ events and applying the $B^0 \to \phi K^{*0}$ selection. The resulting mass distribution is shown in Figure 4.8, where the line shapes have been combined including the expected

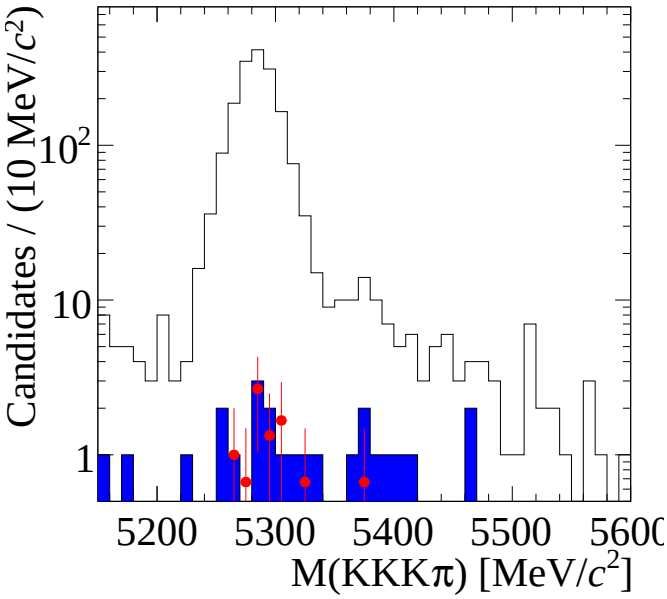

Figure 4.7: The $K^+K^-K^+\pi^-$ mass spectrum (white) with possible D_s^- meson candidates overlaid (blue). Data from the D_s^- sidebands ($21 < |M(KK\pi) - m_{Ds^-}| < 81\,\text{MeV}/c^2$) are scaled by 1/3, which is the ratio of the D_s^- signal to sideband mass windows, and are shown as red points.

Cabibbo suppression of the $p\pi^-$ mode.

These decays have yet to be observed and as such no measurement of their branching fractions exist. As the yields cannot be estimated and only an approximation to their line shapes is made, the contribution from $\Lambda_b^0 \to p\pi^-\phi$ and $\Lambda_b^0 \to pK^-\phi$ is treated as a systematic uncertainty (Sec. 5.3.1).

Partially reconstructed B decays

If the $K^+K^-K^+\pi^-$ mass range is extended below $5150\,\text{MeV}/c^2$ a contribution from partially reconstructed B decays can be observed, as seen in Figure 4.9. Most of this contribution is removed via the selection, in particular the $M(KKK\pi) > 5150\,\text{MeV}/c^2$ requirement (see Sec. 4.2), however the tail of this distribution could extend into the signal region. To test this, the contribution from partially reconstructed B decays is fitted over the extended mass range using an ARGUS function [135] convolved with a Gaussian distribution.

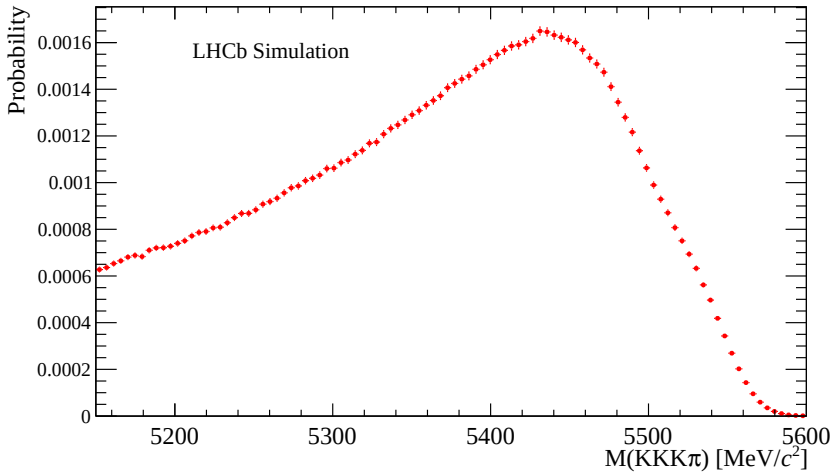

Figure 4.8: Sum of line shapes for the decays $\Lambda_b^0 \to p\pi^-\phi$ and $\Lambda_b^0 \to pK^-\phi$ where the former contains a misidentified proton and the latter contains a misidentified proton and kaon.

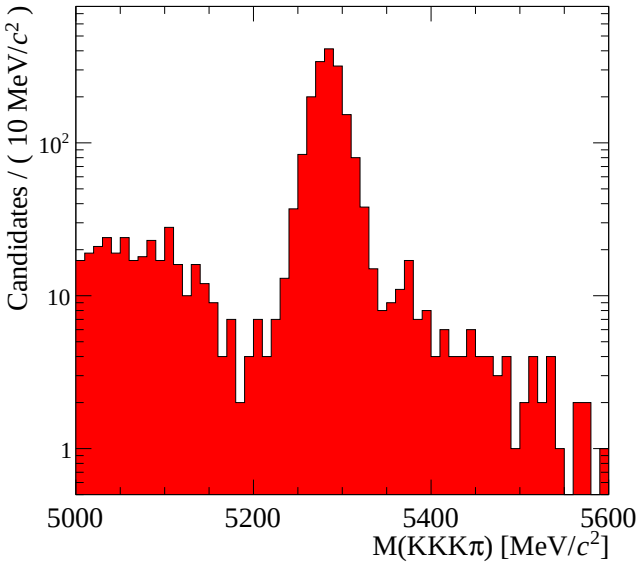

Figure 4.9: $K^+K^-K^+\pi^-$ mass distribution extended to 5000 MeV/c^2.

The ARGUS function is defined

$$AR(M) = M\left[1 - \frac{M^2}{M_{AR}^2}\right]^p \times \exp\left(c - \frac{c \cdot M^2}{M_{AR}^2}\right), \tag{4.12}$$

where M_{AR} is the mean of the ARGUS distribution. The tail of the ARGUS function is described by p and c. The difference between this model and the nominal fit is treated as a source of systematic uncertainty (see Sec. 5.3.1).

4.4.3 Results of mass fit

In order to determine the signal yield an unbinned maximum likelihood fit is made to the $K^+K^-K^+\pi^-$ mass distribution using the RooFit framework [136]. The mass distribution is shown in Figure 4.10, from which a signal yield of 1655 ± 42 B^0 candidates is observed. The full results of the fit are shown in Table 4.2.

Parameter	Status	Value
N_{sig}	Free	1655 ± 42
N_{bs}	Free	40 ± 9
N_{bkg}	Free	157 ± 18
M	Free	$5284.2 \pm 0.4\,\text{MeV}/c^2$
σ_{CB}	Free	$15.7 \pm 0.4\,\text{MeV}/c^2$
σ_{G}	Fixed	$26.3\,\text{MeV}/c^2$
f_{CB}	Fixed	0.875
a	Fixed	2.79
n	Fixed	1.0
λ	Free	$(-2.0 \pm 0.4) \times 10^{-3}$

Table 4.2: Results from a fit to data of the $K^+K^-K^+\pi^-$ mass, showing which parameters are free in the fit and which are fixed from simulation. N_{sig}, N_{bs}, N_{bkg} are the B^0, B_s^0 and combinatorial background yields, respectively. M is the B^0 mean, which is slightly shifted from the known value as the LHCb momentum measurements were not properly calibrated. The slope of the background is given by λ.

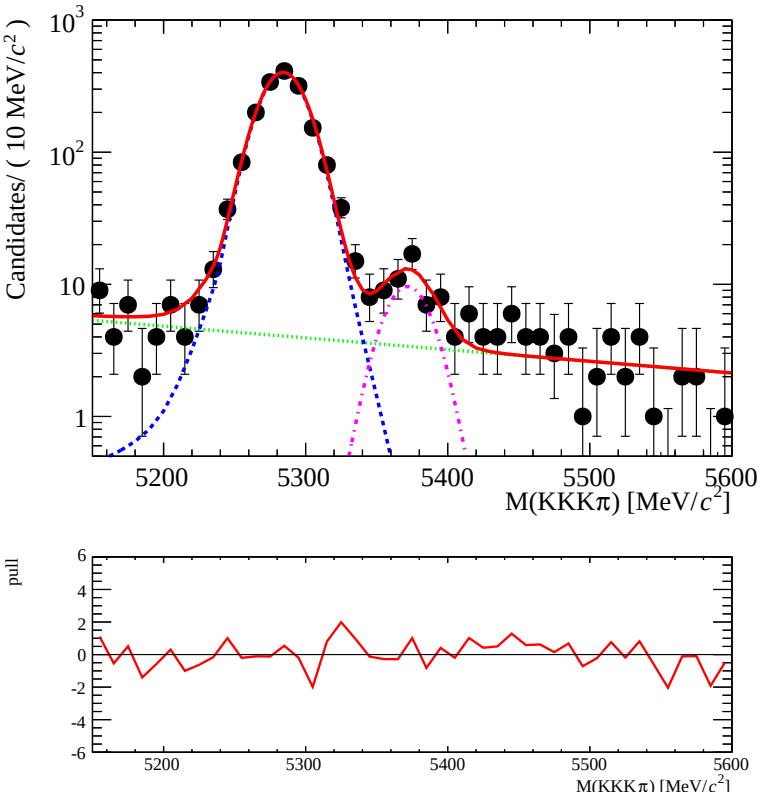

Figure 4.10: Mass distribution for selected $K^+K^-K^+\pi^-$ candidates. A fit to the model described in Sec 4.4 is superimposed (red). The signal contribution is shown as the blue dotted line. The $B_s^0 \to \phi\overline{K}^*$ contribution is shown as the purple dot-dashed line and the combinatorial background is shown as the green dotted line. The pull distribution is shown below and is small across the entire mass range.

4.5 Treatment of non-uniform acceptance effects

The main aim of this analysis is to determine the polarisation amplitudes from the background subtracted angular and resonance mass distributions, as discussed in Sec. 3.2. The results of the analysis are shown in Chapter 5 but in order to make this measurement a good understanding of the detector acceptance, as a function of the angles and resonance masses, is needed.

Due to the detector geometry and selection criteria, the efficiency as a function of some of the helicity angles and resonance masses is non-uniform. Quantities

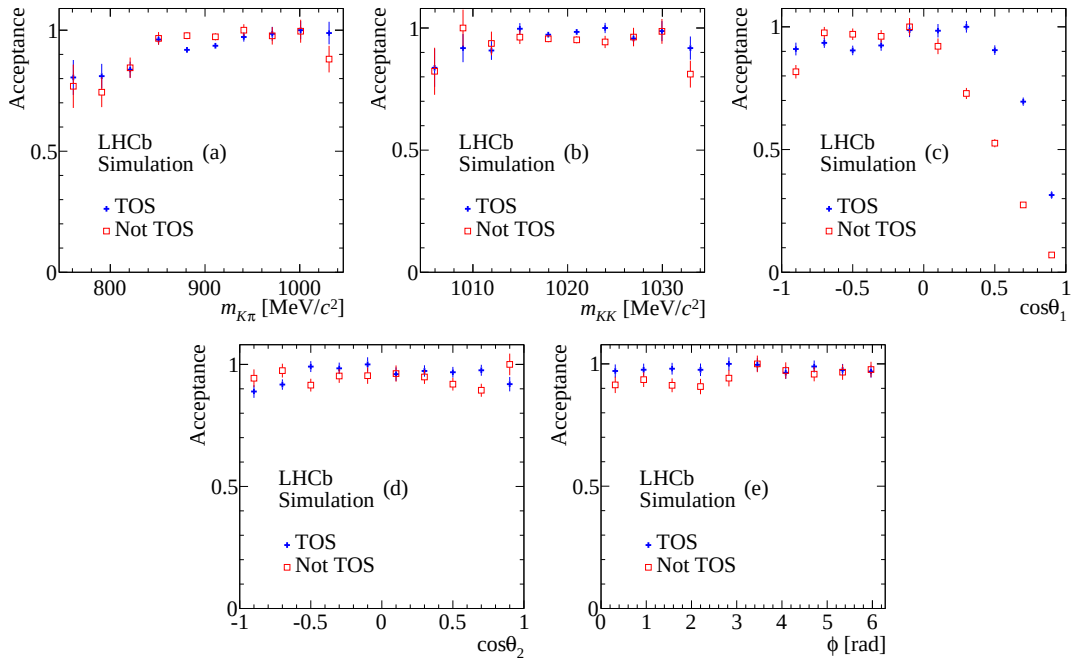

Figure 4.11: Binned projections of the detector acceptance for (a) $m_{K\pi}$, (b) m_{KK} , (c) $\cos\theta_1$, (d) $\cos\theta_2$ and (e) Φ. The acceptance for the TOS (filled crosses) and not-TOS (open squares) trigger categories are shown on each plot.

relating to the p_{T} of the decay products are used in the hardware trigger decision, therefore the efficiency is expected to be different for events in the TIS and TOS categories. As some events can fall into both categories, for the angular analysis, the overlap events are placed into the TOS category and the remaining TIS candidates are labelled 'not-TOS'. Efficiency plots for TOS and not-TOS categories are obtained from simulation by dividing histograms filled from the simulation by corresponding ones filled by the theoretical PDF (Eqn. 3.16) and are shown in Figure 4.11. The efficiency in $m_{KK}, \cos\theta_2$ and Φ is nearly flat while in $\cos\theta_1$ there is a large drop in efficiency as $\cos\theta_1 \to 1$. This is due to the p_{T} requirements in the selection which remove low p_{T} pions. The $m_{K\pi}$ efficiency slowly rises across the mass range.

The efficiency is modelled in three angles and $m_{K\pi}$ using Legendre polynomials [137], where it has been assumed that the m_{KK} efficiency is uniform (see Figure 4.11). This parameterisation is motivated by the fact that the angular terms of the decay rate (see Table 3.1) can easily be written in terms of spherical

harmonics and Legendre polynomials. The efficiency has the form

$$\epsilon(\vec{\Omega}) \equiv \sum_{abcd} c^{abcd} P_a(m_{K\pi}) P_b(\cos\theta_1) Y_{cd}(\cos\theta_2, \Phi) \ , \tag{4.13}$$

where $\vec{\Omega} = (m_{K\pi}, \cos\theta_1, \cos\theta_2, \Phi)$, P are Legendre polynomials, Y are spherical harmonics and $abcd$ are integers between zero and four. The coefficients, c^{abcd}, are determined from simulation by first noting that an efficiency can be written as a sum over accepted events

$$\begin{aligned} \frac{1}{N_A}\sum_{i=1}^{N_A} f(\vec{\Omega}_i) &= \frac{1}{N_G}\sum_{i=1}^{N_G} \epsilon(\vec{\Omega}_i) f(\vec{\Omega}_i) \ , \\ &\approx \int g(\vec{\Omega}) d\vec{\Omega}\, \epsilon(\vec{\Omega}) f(\vec{\Omega}) \ , \end{aligned} \tag{4.14}$$

where N_G are the number of events generated by the PDF $g(\vec{\Omega})$ which describes the angular and mass distributions (Eqn. 3.16), $f(\vec{\Omega})$ is a function upon which the PDF depends (see Table 3.1) and N_A are the number of accepted events after some efficiency function $\epsilon(\vec{\Omega})$ has been applied.

The orthogonality relation between Legendre polynomials is given

$$\int_{-1}^{1} P_a(x) P_b(x) dx = \frac{2}{2b+1}\delta_{ab} \ , \tag{4.15}$$

and similarly for spherical harmonics

$$\int_0^{\pi}\int_0^{2\pi} Y_{ab}(\theta,\Phi) Y_{cd}(\theta,\Phi) \sin\theta d\theta d\Phi = \delta_{ac}\delta_{bd} \ , \tag{4.16}$$

which make it easy to simplify the following equations. Substituting Eqn. 4.13 into Eqn. 4.14 gives

$$\frac{1}{N_A}\sum_{i=1}^{N_A} f(\vec{\Omega}_i) = \int g(\vec{\Omega}) f(\vec{\Omega}) d\vec{\Omega} \sum_{abcd} c^{abcd} P_a P_b Y_{cd} \ , \tag{4.17}$$

which can then be written with $f(\vec{\Omega})$ expressed in terms of Legendre polynomials

and spherical harmonics giving

$$\begin{aligned}\frac{1}{N_A} & \sum_{i=1}^{N_A} \frac{(2j+1)(2k+1)}{4} \frac{P_j P_k Y_{lm}}{g(\vec{\Omega})} \\ &= \int g(\vec{\Omega}) d\vec{\Omega} c^{abcd} P_a P_b Y_{cd} \left[\frac{(2j+1)(2k+1)}{4} \frac{P_j P_k Y_{lm}}{g(\vec{\Omega})} \right] , \\ &= c^{abcd} \frac{(2j+1)(2k+1)}{4} \int d\vec{\Omega} P_a P_b P_j P_k Y_{cd} Y_{lm} \, . \end{aligned} \tag{4.18}$$

Using the orthogonality relations given in Eqns. 4.15 and 4.16, Eqn. 4.18 is reduced to

$$\frac{1}{N_A} \sum_{i=1}^{N_A} \frac{(2j+1)(2k+1)}{4} \frac{P_a P_b Y_{cd}}{g(\vec{\Omega})} = c^{abcd} \, . \tag{4.19}$$

This produces a set of coefficients which can be used to describe the efficiency as a function of $\cos\theta_1, \cos\theta_2, \Phi$ and $m_{K\pi}$ which does not assume the efficiency factorises between any of the angles or $m_{K\pi}$. The order of the polynomials is chosen to give a good description of the acceptance, as shown in Figs. 4.12 and 4.13. A 4^{th} order polynomial is used to model $\cos\theta_1$ and 2^{nd} order polynomials are used for $\cos\theta_2$, Φ and $m_{K\pi}$. The coefficients are calculated from 45,550 simulated events (see Sec. 4.1), *i.e.* $N_A = 45,550$. The coefficients are shown in Tables 4.3 and 4.4.

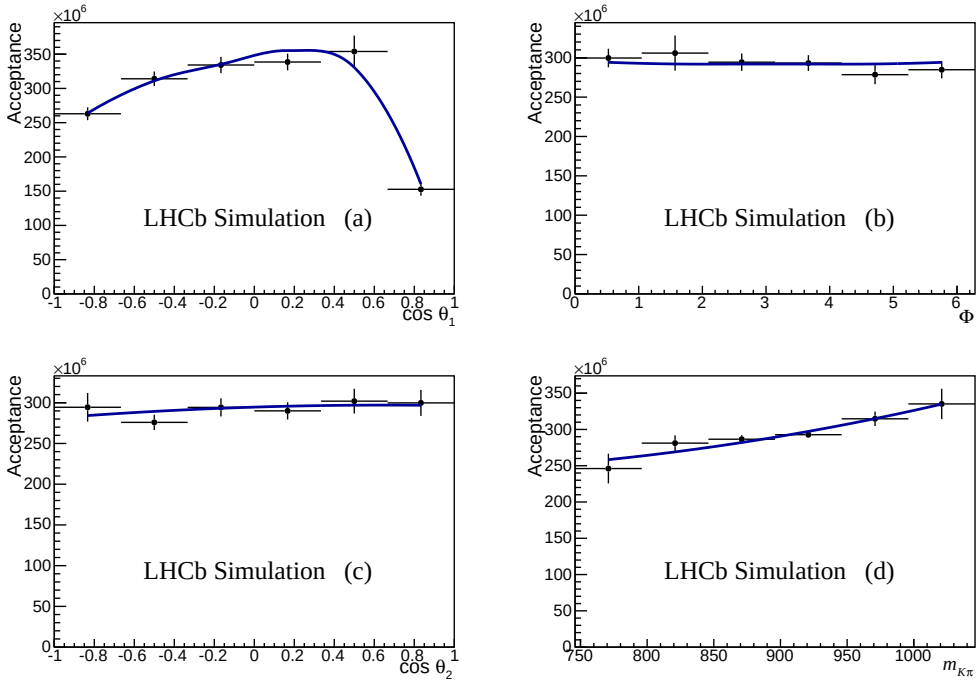

Figure 4.12: Projections of the detector acceptance for TOS candidates for (a) $\cos\theta_1$, (b) $\cos\theta_2$, (c) Φ and $m_{K\pi}$. The acceptance calculated using the Legendre polynomials and spherical harmonics is overlayed. Note this is a one dimensional projection of a three dimensional acceptance function, it is not a fit to the points.

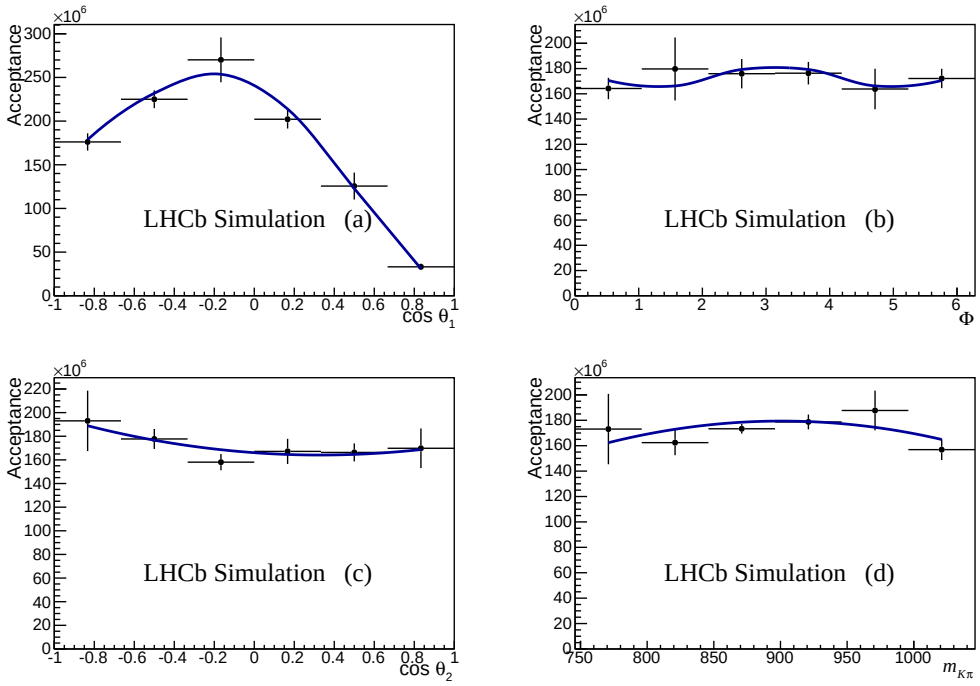

Figure 4.13: Projections of the detector acceptance for not-TOS candidates for (a) $\cos\theta_1$, (b) $\cos\theta_2$, (c) Φ and $m_{K\pi}$. The acceptance calculated using the Legendre polynomials and spherical harmonics is overlayed. Note this is a one dimensional projection of a three dimensional acceptance function, it is not a fit to the points. This is demonstrated in the $\cos\theta_2$ projection which seems to be over fitting if taken as a fit to the points.

TOS Coefficient	Value	TOS Coefficient	Value
c^{0000}	4271.777±0.003	c^{1211}	293.074±0.011
c^{0001}	63.980±0.003	c^{1212}	239.204±0.011
c^{0002}	-25.418±0.003	c^{1222}	120.762±0.011
c^{0011}	-14.311±0.002	c^{1300}	150.879±0.017
c^{0012}	-11.006±0.002	c^{1301}	853.818±0.020
c^{0022}	9.157±0.003	c^{1302}	-304.052±0.017
c^{0100}	-578.210±0.004	c^{1311}	285.928±0.012
c^{0101}	35.942±0.004	c^{1312}	-506.575±0.012
c^{0102}	131.885±0.004	c^{1322}	60.880±0.016
c^{0111}	29.302±0.003	c^{1400}	-681.392±0.016
c^{0112}	67.703±0.003	c^{1401}	91.695±0.018
c^{0122}	-76.643±0.004	c^{1402}	-66.767±0.015
c^{0200}	-2096.609±0.005	c^{1411}	-392.626±0.014
c^{0201}	-175.116±0.005	c^{1412}	230.422±0.015
c^{0202}	252.445±0.005	c^{1422}	-2.193±0.015
c^{0211}	-98.464±0.005	c^{2000}	101.827±0.008
c^{0212}	-17.055±0.005	c^{2001}	94.353±0.010
c^{0222}	8.194±0.005	c^{2002}	572.150±0.009
c^{0300}	-1071.932±0.007	c^{2011}	-103.027±0.006
c^{0301}	-204.899±0.008	c^{2012}	75.241±0.007
c^{0302}	-360.941±0.007	c^{2022}	-88.644±0.007
c^{0311}	-171.076±0.005	c^{2100}	993.226±0.012
c^{0312}	-46.942±0.005	c^{2101}	-42.817±0.012
c^{0322}	240.811±0.007	c^{2102}	350.782±0.011
c^{0400}	-676.608±0.007	c^{2111}	-311.358±0.009
c^{0401}	-133.240±0.007	c^{2112}	343.981±0.008
c^{0402}	-216.450±0.006	c^{2122}	-307.714±0.011
c^{0411}	230.151±0.006	c^{2200}	-928.204±0.015
c^{0412}	35.856±0.006	c^{2201}	-190.319±0.017
c^{0422}	41.547±0.007	c^{2202}	-452.293±0.016
c^{1000}	669.584±0.007	c^{2211}	-88.236±0.014
c^{1001}	-281.817±0.008	c^{2212}	45.966±0.015
c^{1002}	27.687±0.007	c^{2222}	-340.400±0.014
c^{1011}	5.387±0.005	c^{2300}	-474.108±0.021
c^{1012}	-72.265±0.005	c^{2301}	-545.763±0.026
c^{1022}	-255.963±0.006	c^{2302}	-945.130±0.022
c^{1100}	-1266.288±0.010	c^{2311}	-356.995±0.014
c^{1101}	-340.194±0.010	c^{2312}	107.321±0.015
c^{1102}	80.672±0.009	c^{2322}	662.793±0.019
c^{1111}	-12.504±0.008	c^{2400}	519.979±0.020
c^{1112}	53.162±0.007	c^{2401}	-273.609±0.023
c^{1122}	-156.507±0.009	c^{2402}	-362.843±0.020
c^{1200}	950.113±0.012	c^{2411}	-381.396±0.017
c^{1201}	540.449±0.013	c^{2412}	-15.729±0.019
c^{1202}	-410.758±0.013	c^{2422}	944.199±0.019

Table 4.3: Table showing the calculated value of the coefficients for the TOS subsample.

not-TOS Coefficient	Value	not-TOS Coefficient	Value
c^{0000}	4397.325±0.009	c^{1211}	-710.759±0.043
c^{0001}	-178.103±0.011	c^{1212}	-1248.596±0.031
c^{0002}	139.919±0.009	c^{1222}	-58.481±0.042
c^{0011}	99.030±0.006	c^{1300}	-808.109±0.053
c^{0012}	-48.282±0.006	c^{1301}	920.467±0.058
c^{0022}	138.054±0.007	c^{1302}	-2313.328±0.053
c^{0100}	-2410.023±0.011	c^{1311}	483.745±0.053
c^{0101}	154.385±0.011	c^{1312}	-132.868±0.034
c^{0102}	-19.368±0.011	c^{1322}	1180.959±0.055
c^{0111}	-277.918±0.012	c^{1400}	-2081.513±0.045
c^{0112}	-200.170±0.007	c^{1401}	490.676±0.039
c^{0122}	-42.440±0.012	c^{1402}	618.820±0.051
c^{0200}	-3109.336±0.019	c^{1411}	-1356.840±0.059
c^{0201}	484.861±0.021	c^{1412}	477.166±0.035
c^{0202}	-575.898±0.021	c^{1422}	-700.038±0.056
c^{0211}	258.498±0.018	c^{2000}	-386.068±0.017
c^{0212}	251.329±0.013	c^{2001}	-479.762±0.019
c^{0222}	73.605±0.018	c^{2002}	-313.227±0.018
c^{0300}	469.218±0.025	c^{2011}	332.191±0.017
c^{0301}	-655.592±0.029	c^{2012}	-278.721±0.017
c^{0302}	349.013±0.025	c^{2022}	682.418±0.016
c^{0311}	-158.375±0.023	c^{2100}	489.150±0.023
c^{0312}	-9.580±0.015	c^{2101}	-102.662±0.018
c^{0322}	-547.013±0.025	c^{2102}	-196.799±0.022
c^{0400}	794.699±0.020	c^{2111}	-663.505±0.029
c^{0401}	-731.417±0.018	c^{2112}	-471.521±0.019
c^{0402}	408.337±0.023	c^{2122}	-66.238±0.027
c^{0411}	545.181±0.025	c^{2200}	-501.732±0.039
c^{0412}	-7.806±0.015	c^{2201}	1755.410±0.039
c^{0422}	661.344±0.024	c^{2202}	-7.121±0.041
c^{1000}	38.824±0.019	c^{2211}	-44.959±0.045
c^{1001}	447.793±0.023	c^{2212}	947.378±0.037
c^{1002}	-119.692±0.020	c^{2222}	-174.928±0.040
c^{1011}	-122.846±0.015	c^{2300}	666.266±0.046
c^{1012}	410.724±0.015	c^{2301}	-932.257±0.045
c^{1022}	-637.013±0.016	c^{2302}	1330.516±0.047
c^{1100}	93.446±0.024	c^{2311}	-233.853±0.054
c^{1101}	-224.620±0.022	c^{2312}	-10.950±0.038
c^{1102}	213.898±0.023	c^{2322}	-1298.432±0.050
c^{1111}	951.952±0.028	c^{2400}	1535.897±0.046
c^{1112}	311.094±0.016	c^{2401}	-1341.895±0.040
c^{1122}	276.319±0.023	c^{2402}	-192.411±0.050
c^{1200}	625.762±0.041	c^{2411}	1680.810±0.059
c^{1201}	-900.405±0.044	c^{2412}	-569.122±0.042
c^{1202}	1168.838±0.044	c^{2422}	1405.266±0.055

Table 4.4: Table showing the calculated value of the coefficients for the not-TOS subsample.

Chapter 5

Results from the analysis of $B^0 \to \phi K^*(892)^0$

5.1 Determination of fit parameters

The parameters measured in the angular analysis are defined in Table 5.1. In this analysis the *sPlot* technique is used to subtract the background and an unbinned maximum likelihood fit is made to the signal only likelihood shown in Eqn. 3.16. The *sPlot* technique only works when the correlation between the observables and separation parameters is small. The correlation between distributions x and y is defined as

$$\eta = \frac{\mathrm{cov}(x, y)}{\sigma_x \sigma_y} \,, \tag{5.1}$$

where $\sigma_x(\sigma_y)$ is the RMS for the distribution $x(y)$. Using this definition, the correlation between the angles, $m_{K\pi}$, m_{KK} and $\mathrm{M}(K^+K^-K^+\pi^-)$ is calculated and shown in Table 5.2. As this is found to be small, the *sPlot* technique is valid for this analysis.

The selection efficiency is included by multiplying the signal PDF by the efficiency function shown in Eqn. 4.13. The method described in Section 4.5 is used to calculate the coefficients and these are shown in Tables 4.3 and 4.4.

The data are separated into TOS and not-TOS subsamples and the fit performed using the RapidFit framework [138]: a fitter written by the Edinburgh Group specifically for angular analyses. The results are described in Section 5.3.

Parameter	Definition
$f_{\rm L}$	$0.5(\lvert A_0\rvert^2/F_{\rm P} + \lvert\overline{A}_0\rvert^2/\overline{F}_{\rm P})$
$f_\perp$	$0.5(\lvert A_\perp\rvert^2/F_{\rm P} + \lvert\overline{A}_\perp\rvert^2/\overline{F}_{\rm P})$
$f_{\rm S}(K\pi)$	$0.5(\lvert A_{\rm S}^{K\pi}\rvert^2 + \lvert\overline{A}_{\rm S}^{K\pi}\rvert^2)$
$f_{\rm S}(KK)$	$0.5(\lvert A_{\rm S}^{KK}\rvert^2 + \lvert\overline{A}_{\rm S}^{KK}\rvert^2)$
$\delta_\perp$	$0.5(\arg A_\perp + \arg\overline{A}_\perp)$
$\delta_\parallel$	$0.5(\arg A_\parallel + \arg\overline{A}_\parallel)$
$\delta_{\rm S}(K\pi)$	$0.5(\arg A_{\rm S}^{K\pi} + \arg\overline{A}_{\rm S}^{K\pi})$
$\delta_{\rm S}(KK)$	$0.5(\arg A_{\rm S}^{KK} + \arg\overline{A}_{\rm S}^{KK})$
$\mathcal{A}_0^{CP}$	$(\lvert A_0\rvert^2/F_{\rm P} - \lvert\overline{A}_0\rvert^2/\overline{F}_{\rm P})/(\lvert A_0\rvert^2/F_{\rm P} + \lvert\overline{A}_0\rvert^2/\overline{F}_{\rm P})$
$\mathcal{A}_\perp^{CP}$	$(\lvert A_\perp\rvert^2/F_{\rm P} - \lvert\overline{A}_\perp\rvert^2/\overline{F}_{\rm P})/(\lvert A_\perp\rvert^2/F_{\rm P} + \lvert\overline{A}_\perp\rvert^2/\overline{F}_{\rm P})$
$\mathcal{A}_{\rm S}(K\pi)^{CP}$	$(\lvert A_{\rm S}^{K\pi}\rvert^2 - \lvert\overline{A}_{\rm S}^{K\pi}\rvert^2)/(\lvert A_{\rm S}^{K\pi}\rvert^2 + \lvert\overline{A}_{\rm S}^{K\pi}\rvert^2)$
$\mathcal{A}_{\rm S}(KK)^{CP}$	$(\lvert A_{\rm S}^{KK}\rvert^2 - \lvert\overline{A}_{\rm S}^{KK}\rvert^2)/(\lvert A_{\rm S}^{KK}\rvert^2 + \lvert\overline{A}_{\rm S}^{KK}\rvert^2)$
$\delta_\perp^{CP}$	$0.5(\arg A_\perp - \arg\overline{A}_\perp)$
$\delta_\parallel^{CP}$	$0.5(\arg A_\parallel - \arg\overline{A}_\parallel)$
$\delta_{\rm S}(K\pi)^{CP}$	$0.5(\arg A_{\rm S}^{K\pi} - \arg\overline{A}_{\rm S}^{K\pi})$
$\delta_{\rm S}(KK)^{CP}$	$0.5(\arg A_{\rm S}^{KK} - \arg\overline{A}_{\rm S}^{KK})$

Table 5.1: Parameters measured in the angular analysis.

Variable	Correlation with $M_{KKK\pi}$
$\cos\theta_{K\pi}$	-0.004
$\cos\theta_{KK}$	0.005
Φ	-0.001
$m_{K\pi}$	0.039
m_{KK}	0.028

Table 5.2: Correlation between $M(KKK\pi)$ and the helicity angles and resonances masses.

5.2 Goodness of fit

A goodness of fit test known as the point-to-point dissimilarity test [139] is performed to determine the likelihood that the fit result is compatible with the data distribution.

The point-to-point dissimilarity test compares the fit result obtained in Sec. 5.3 with the full data sample. The fit result is used to generate 90,000 simulation events which are used to compare to the data. The test returns a p-value which can be interpreted as a rejection of the hypothesis $S_0 = S$ at a confidence level $1 - P$, where S_0 is the theoretical PDF to which the data distribution, S, is compared and P is the p-value. The p-value returned by the goodness of fit for this analysis is 0.64, indicating no disagreement between the data and fit result.

5.3 Polarisation amplitudes

The polarisation amplitudes are determined from the angular and resonance mass distributions, as described in Sec. 5.1. The results are shown in Table 5.3 and the projection of the fit results onto the data distributions are shown in Figure 5.1. A goodness of fit test determines a p-value of 0.64 (see Sec. 5.2).

The results show equal longitudinal and transverse polarisations with amplitude structure $f_{\mathrm{L}} \approx 2f_{\perp} \approx 2f_{\parallel}$ while significant S-wave fractions are observed in both the $K^+\pi^-$ and K^+K^- systems. The strong phases for the P- and S-wave contributions are significantly different from zero or π indicating the presence of final-state interactions. The *CP*-violating parameters are consistent with zero, supporting previous measurements. The systematic uncertainties will be discussed in the following section.

5.3.1 Systematic uncertainties

The systematic uncertainty on the polarisation amplitudes is dominated by the uncertainty on the efficiency function while for the phases the main contribution comes from the S-wave mass model. Other contributions come from the B^0 mass model and the difference in kinematic variables between data and simulation. The systematic uncertainties are summarised in Table 5.4 and are discussed in more detail in the following sections.

Parameter	Fitted value
$f_{\rm L}$	0.497 ± 0.019
$f_\perp$	0.221 ± 0.016
$f_{\rm S}(K\pi)$	0.143 ± 0.013
$f_{\rm S}(KK)$	0.122 ± 0.013
$\delta_\perp$	2.633 ± 0.062
$\delta_\parallel$	2.562 ± 0.069
$\delta_{\rm S}(K\pi)$	2.222 ± 0.063
$\delta_{\rm S}(KK)$	2.481 ± 0.072
$\mathcal{A}_0^{CP}$	-0.003 ± 0.038
$\mathcal{A}_\perp^{CP}$	$+0.047 \pm 0.074$
$\mathcal{A}_{\rm S}(K\pi)^{CP}$	$+0.073 \pm 0.091$
$\mathcal{A}_{\rm S}(KK)^{CP}$	-0.209 ± 0.105
$\delta_\perp^{CP}$	$+0.062 \pm 0.062$
$\delta_\parallel^{CP}$	$+0.045 \pm 0.069$
$\delta_{\rm S}(K\pi)^{CP}$	$+0.062 \pm 0.062$
$\delta_{\rm S}(KK)^{CP}$	$+0.022 \pm 0.072$

Table 5.3: Results of the angular analysis, where the uncertainty is statistical.

Parameter	Efficiency	B^0 model	Data/MC difference	S-wave model	Total
$f_{\rm L}$	0.014	0.002	0.005	0.001	0.015
$f_\perp$	0.013	0.001	0.002	0.001	0.013
$f_{\rm S}(K\pi)$	0.012	0.001	-	0.002	0.012
$f_{\rm S}(KK)$	0.007	0.002	-	0.003	0.008
$\delta_\parallel$	0.023	0.006	0.010	0.026	0.037
$\delta_\perp$	0.029	0.004	0.013	0.024	0.040
$\delta_{\rm S}(K\pi)$	0.045	0.004	0.026	0.062	0.081
$\delta_{\rm S}(KK)$	0.045	0.004	0.005	0.016	0.048
$\mathcal{A}_\perp^{CP}$	-	0.002	0.002	0.004	0.005
$\mathcal{A}_0^{CP}$	-	0.006	0.001	0.007	0.009
$\mathcal{A}_{\rm S}(K\pi)^{CP}$	-	0.005	0.007	0.034	0.035
$\mathcal{A}_{\rm S}(KK)^{CP}$	-	0.009	0.007	0.003	0.012
$\delta_\parallel^{CP}$	-	0.001	0.003	0.004	0.005
$\delta_\perp^{CP}$	-	0.002	0.005	0.014	0.015
$\delta_{\rm S}(K\pi)^{CP}$	-	0.003	0.005	0.021	0.022
$\delta_{\rm S}(KK)^{CP}$	-	0.002	0.002	0.003	0.004

Table 5.4: Summary of systematic uncertainties for the angular analysis results. The column labelled 'total' is the quadratic sum of the individual components.

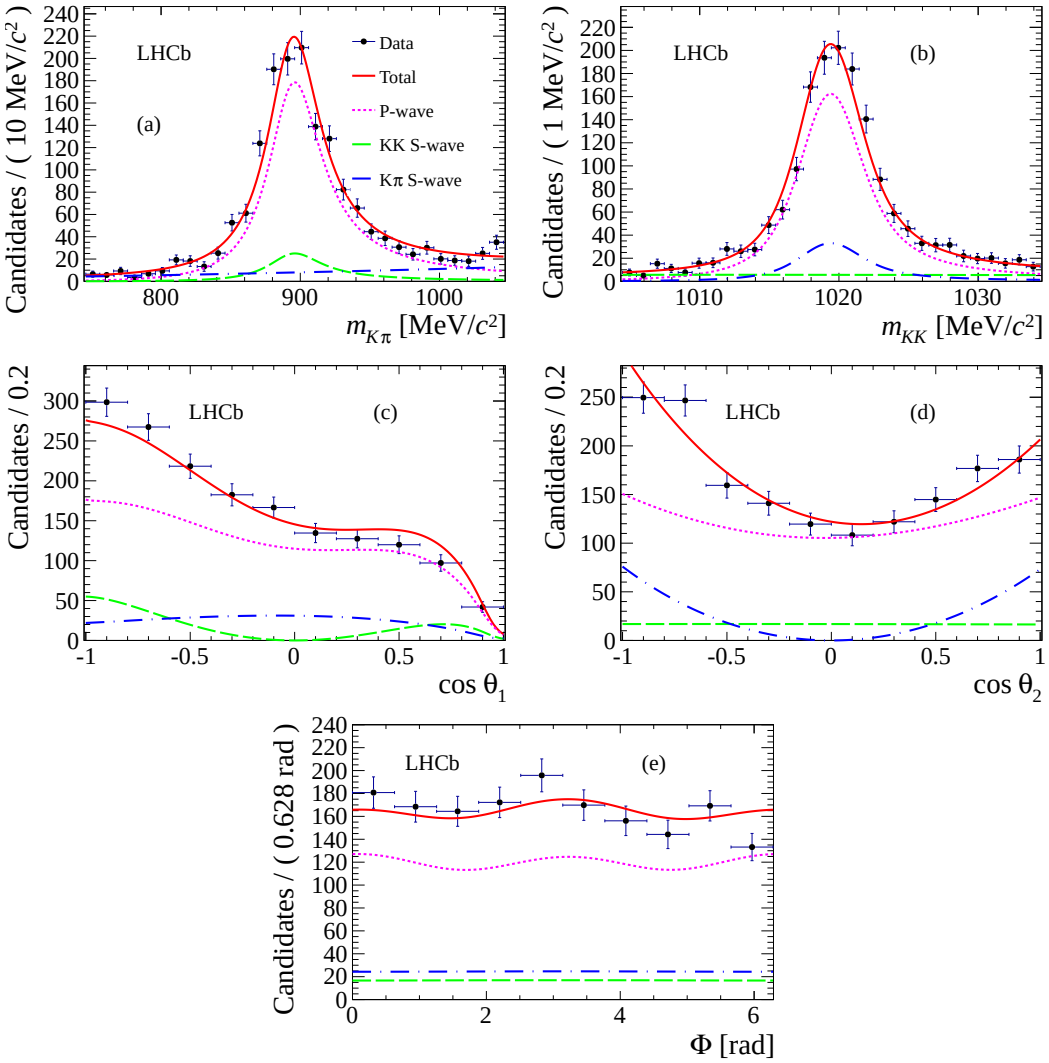

Figure 5.1: Data distributions for the helicity angles and intermediate-resonance masses: (a) $m_{K\pi}$ and (b) m_{KK}, (c) $\cos\theta_1$, (d) $\cos\theta_2$ and (e) Φ. The background has been subtracted using the *sPlot* technique and the results of the fit are superimposed.

Efficiency function

The efficiency function is calculated using simulated events, as described in Sec. 4.5. The finite simulation statistics limit the precision of the coefficients and so a systematic uncertainty is added to the final result. It was not possible to generate additional simulated events because of the lack of available computing resources.

Parameter	Value
f_{L}	0.521
$f_{\perp}$	0.251
$\delta_{\perp}$	1.426
$\delta_{\parallel}$	1.352

Table 5.5: Amplitudes used to generate simulated events to study the efficiency function. The S-wave components and *CP* asymmetries are zero.

To evaluate this uncertainty, two million generator level events are produced using EvtGen [76] with the amplitudes shown in Table 5.5. These events only contain four-vector information for each particle. A simple kinematic selection is applied to reproduce the main effect of the selection: a non-uniform loss in efficiency in helicity angles and resonance masses. The selection requires that the final-state particle p_{T} is greater than 500 MeV/c and the intermediate-resonance p_{T} is greater than 900 MeV/c. Figure 5.2 shows the distribution of $\cos\theta_1$ for simulated events before and after the aforementioned selection is applied, demonstrating the drop in efficiency as $\cos\theta \to 1$.

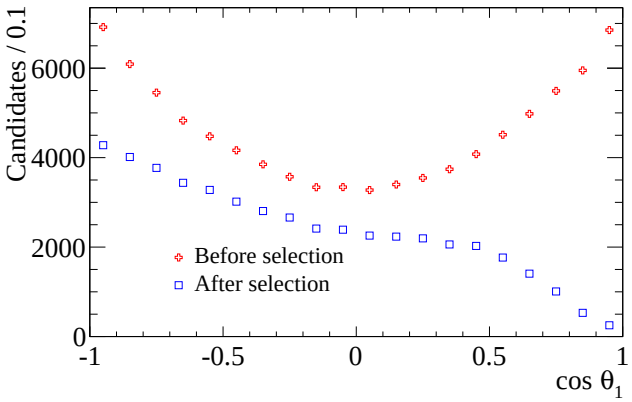

Figure 5.2: Simulated events before and after selection criteria are applied on the final-state and intermediate-resonance p_{T}.

After this selection is applied approximately 0.9 million candidates remain; from these an efficiency function is calculated, as described in Sec. 4.5. This efficiency is then included in the generation phase of a series of pseudo-experiments.

For each experiment a sample of 45,000 events is generated, corresponding to

approximately the size of the full simulation sample after all selections. A further 0.5 million events are also generated. The size of the large sample is chosen to reduce the statistical uncertainty on the angular fit variables to a negligible level compared to data.

The acceptance is calculated using the small sample and used to fit the large sample. Therefore, the difference between the fitted result and the generated result is due to the knowledge of the acceptance.

The difference between the fit result and the value used in the generation of the simulation is plotted for each parameter. This is repeated 365 times and a fit made to each distribution using a Gaussian function. The width of the Gaussian function is taken as the systematic uncertainty on each parameter due to the acceptance correction. The results of this study are shown in Table 5.6. The systematic uncertainty on the *CP*-violating parameters is zero because it is assumed that the acceptance does not depend on the charge of the final-state particles. This is checked in Section 5.6 by comparing magnet up/down and TOS/not-TOS results in data. In Appendix B the $B^0/\overline{B}^0$ results from simulation are also checked.

Parameter	Systematic uncertainty
f_{L}	0.013
$f_{\perp}$	0.014
$f_{\mathrm{S}}(K\pi)$	0.012
$f_{\mathrm{S}}(KK)$	0.007
$\delta_{\perp}$	0.023
$\delta_{\parallel}$	0.029
$\delta_{\mathrm{S}}(K\pi)$	0.045
$\delta_{\mathrm{S}}(KK)$	0.045

Table 5.6: Systematic uncertainty on fit parameters due to the statistical uncertainty on the acceptance correction. The systematic uncertainty on the *CP*-violating parameters is zero.

$\mathbf{B^0}$ mass model

The model describing the $K^+K^-K^+\pi^-$ mass spectrum is used to determine the signal and background yields for the *sPlot* technique (see Sec. 4.3.2). The effect of

the $K^+K^-K^+\pi^-$ mass model on the angular fit variables is probed by remaking the per-event weights using a variety of signal and background models.

As a variation on the signal model a double Gaussian function is used. The Gaussian functions have a shared mean and the width of the smaller, wider Gaussian function is fixed to 28.2 MeV/c^2 from simulation. The fraction of the narrower Gaussian is 0.880, compared to 0.875 for the other fit models considered. The projection of this fit onto the data is shown in Fig. 5.3. To study the effect of the background model, the exponential function is replaced by a first order polynomial with the projection of the fit shown in Fig. 5.4.

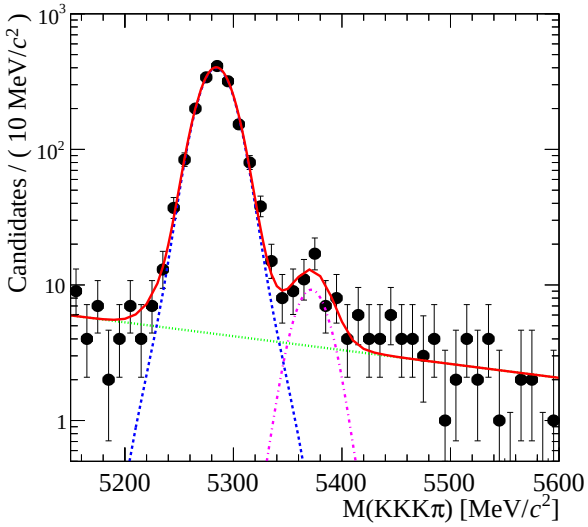

Figure 5.3: Distribution of $K^+K^-K^+\pi^-$ mass where a double Gaussian function is used to model the B^0 and B_s^0 peaks (blue dashed and magenta dot-dashed lines, respectively). An exponential is used to model the combinatorial background (green dotted line) and the total of these components is shown as the solid red line.

The effect of additional peaking backgrounds is studied by adding components to the nominal model. The decay $\Lambda_b^0 \to pK^-\phi$ can be misidentified as $B^0 \to \phi K^{*0}$ if the pK^- pair is misidentified as $K^+\pi^-$. Similarly, in $\Lambda_b^0 \to p\pi^-\phi$ a $p \to K^+$ misidentification leads to the $K^+K^-K^+\pi^-$ final state. As a systematic check a component describing these is added to the fit.

The shape is fixed from simulation and the yield is allowed to vary in the fit (see Sec. 4.4.2). The projection of this fit onto the data is shown in

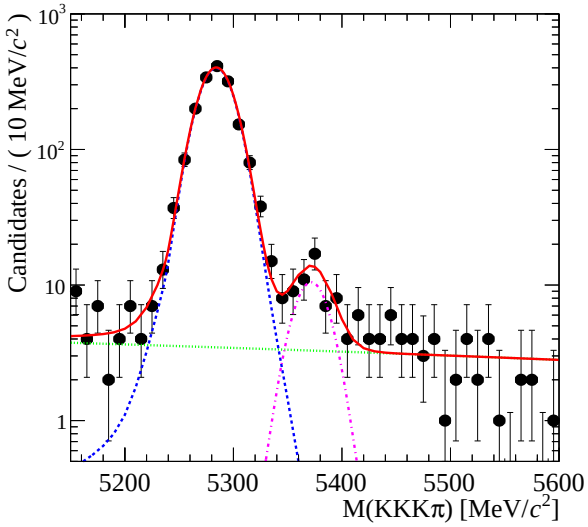

Figure 5.4: Distribution of $K^+K^-K^+\pi^-$ mass where the background is described by a first order polynomial (green dotted line). The B^0 and B_s^0 peaks are shown in blue dashed and magenta dot-dashed lines, respectively and the background in dotted green.

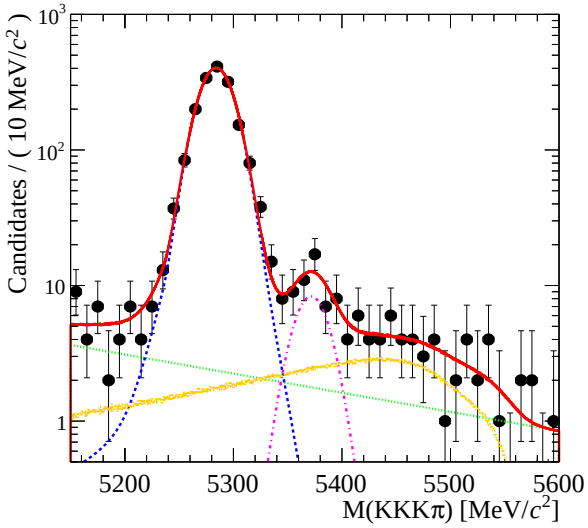

Figure 5.5: Distribution of $K^+K^-K^+\pi^-$ mass. A possible contribution from Λ_b^0 decays is shown as a dotted orange line. The B^0 and B_s^0 peaks are shown in blue dashed and magenta dot-dashed lines, respectively and the combinatorial background in dotted green.

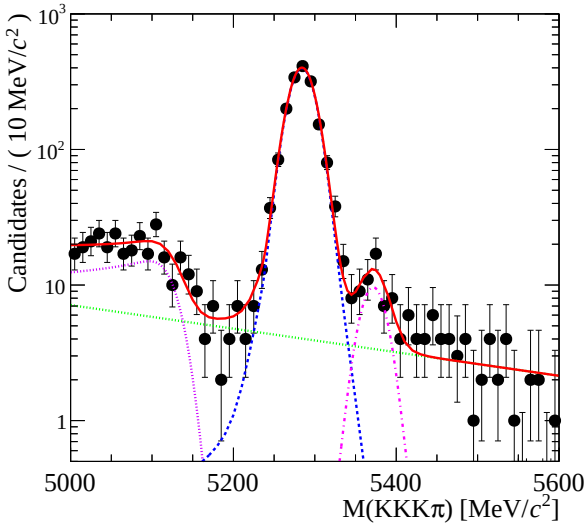

Figure 5.6: Distribution of $K^+K^-K^+\pi^-$ mass where partially reconstructed B decays are included (dotted purple line). The B^0 and B_s^0 peaks are shown in blue dashed and magenta dot-dashed lines, respectively and the combinatorial background in dotted green.

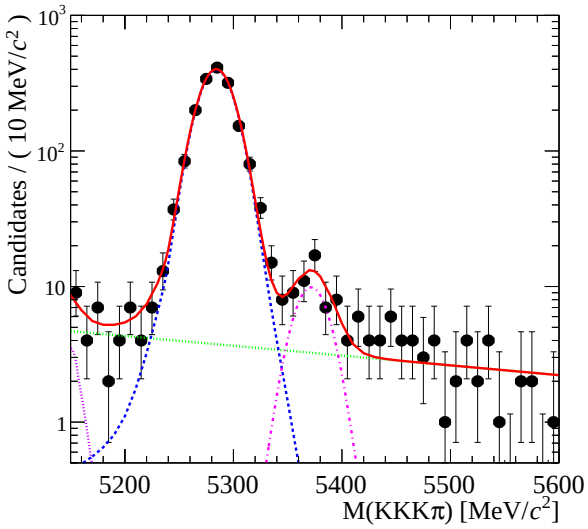

Figure 5.7: Distribution of $K^+K^-K^+\pi^-$ mass where a possible contribution from partially reconstructed B decays is included (dotted purple line). The B^0 and B_s^0 peaks are shown in blue dashed and magenta dot-dashed lines, respectively and the combinatorial background in dotted green.

Fig 5.5. For this model the per-event weights are not remade directly from the fit with the Λ_b^0 components included. This is because the *sPlot* technique relies on the discriminating parameter and fitted parameters being independent from one another. In this case, when a particle misidentification occurs, there is a correlation between the reconstructed $K^+K^-K^+\pi^-$ mass and the decay angles.

To account for this correlation a number of $\Lambda_b^0 \to p\pi^-\phi$ and $\Lambda_b^0 \to pK^-\phi$ events are injected into the signal sample with negative weighting. Each injected event has a weight $w = -N_{\Lambda b}/N_{\rm gen}$, where $N_{\Lambda b}$ is the number of Λ_b^0 events returned from the fit and $N_{\rm gen}$ is the number of Λ_b^0 events injected. The injected events use a phase space model with a simplified simulation. A selection is applied which is similar to the selection applied to data. The number of generated Λ_b^0 events after this selection is applied is $N_{\rm gen} = 3288$. A fit to determine the per-event weights is then done to the dataset which contains both the real data and the Λ_b^0 simulation.

A contribution from partially reconstructed B decays is observed below the signal peak (see Sec. 4.4.2). To see if this affects the results a fit is made to the (5000-5500) MeV/c^2 mass range. An ARGUS function (see Sec. 4.4.2) convolved with a Gaussian function is used to model the partially reconstructed background, as seen in Figure 5.6. The parameters of this fit are then fixed and the per-event weights are remade using the nominal mass range with the ARGUS included, a fit using this model is shown in Figure 5.7. The results of the alternative fits can be seen in Table 5.7.

Parameter	Nominal	Argus	Double Gaussian	Polynominal background	Λ_b^0 background
M(MeV/c^2)	5284.2±0.4	5284.2±0.4	5286.2±0.4	5284.2±0.4	5284.2±0.4
σ(MeV/c^2)	15.7±0.4	15.7±0.4	15.6±0.4	15.6±0.4	15.6±0.4
N_{Bd}	1655±42	1657±42	1648±42	1650±42	1654±42
N_{Bs}	40±9	41±9	38±8	38±9	35±9
$N_{\rm argus}$	-	4±4	-	-	-
$N_{\Lambda b}$	-	-	-	-	77±25

Table 5.7: Fit parameters determined using a variety of signal and background models. The measured mean of the B^0 is denoted by M and σ is the width of the Crystal Ball function or Gaussian function, depending on the model used. The yields for the B^0, B_s^0, Λ_b^0 and low mass background components of the fit are given by $N_{Bd}, N_{Bs}, N_{\Lambda b}$ and $N_{\rm argus}$, respectively.

The angular fit is then repeated using the per-event weights calculated using the different signal and background models. Table 5.8 shows the difference between the tested models and the nominal model where the largest variation for each parameter is chosen as an estimate of the systematic uncertainty.

Parameter	Double Gaussian	Polynomial background	ARGUS	Λ_b^0 background
f_{L}	0.001	0.0	0.002	0.0
$f_{\perp}$	0.0	0.0	0.001	0.001
$f_{\mathrm{S}}(K\pi)$	0.001	0.0	0.0	0.001
$f_{\mathrm{S}}(KK)$	0.001	0.0	0.0	0.002
$\delta_{\parallel}$	0.001	0.001	0.001	0.004
$\delta_{\perp}$	0.003	0.001	0.002	0.006
$\delta_{\mathrm{S}}(K\pi)$	0.0	0.0	0.002	0.004
$\delta_{\mathrm{S}}(KK)$	0.001	0.0	0.001	0.004
$\mathcal{A}_{\perp}^{CP}$	0.001	0.003	0.006	0.001
$\mathcal{A}_{0}^{CP}$	0.001	0.0	0.002	0.001
$\mathcal{A}_{\mathrm{S}}(K\pi)^{CP}$	0.0	0.0	0.001	0.005
$\mathcal{A}_{\mathrm{S}}(KK)^{CP}$	0.0	0.005	0.009	0.003
$\delta_{\parallel}^{CP}$	0.0	0.0	0.0	0.002
$\delta_{\perp}^{CP}$	0.001	0.001	0.0	0.0
$\delta_{\mathrm{S}}(K\pi)^{CP}$	0.003	0.001	0.003	0.002
$\delta_{\mathrm{S}}(KK)^{CP}$	0.002	0.001	0.002	0.001

Table 5.8: Difference between the nominal result and results using various signal and background models for a fit to the $K^+K^-K^+\pi^-$ mass.

Difference in kinematic variables

Figure 5.8 shows a comparison of pion p_{T} for data and simulation, where the background has been subtracted using the *sPlot* technique. Further distributions are shown in Appendix C.1. As small discrepancies are observed in most variables, their effect on the final result is studied.

The simulated $B^0 \to \phi K^{*0}$ events are generated with a different set of polarisation amplitudes than those observed in data *i.e.* the data has S-wave components which are not present in the simulation. This will produce different distributions for the kinematic variables.

The efficiency function is calculated from the simulation and is independent of

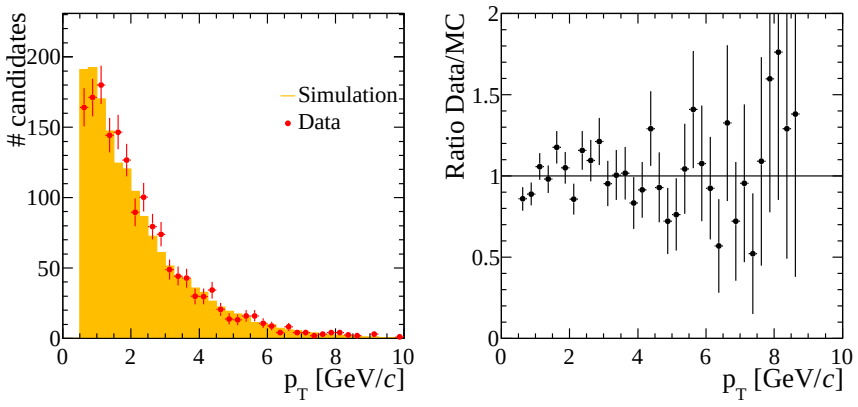

Figure 5.8: Comparison of the pion transverse momentum distribution between data (red points) and simulation (solid yellow). The simulation is normalised to the number of candidates seen in data.

i	f_i	ξ_i^{TOS}	$\xi_i^{\text{not-TOS}}$
1	$\cos\theta_1^2 \cos\theta_2^2$	0.8608	0.8004
2	$\frac{1}{4}\sin\theta_1^2 \sin\theta_2^2(1+\cos(2\Phi))$	1.131	1.16
3	$\frac{1}{4}\sin\theta_1^2 \sin\theta_2^2(1-\cos(2\Phi))$	1.138	1.158
4	$-\frac{1}{2}\sin\theta_1^2 \sin\theta_2^2 \sin(2\Phi)$	0.00295	-0.01935
5	$\sqrt{2}\cos\theta_1 \sin\theta_1 \cos\theta_2 \sin\theta_2 \cos\Phi$	-0.007641	-0.002277
6	$-\sqrt{2}\cos\theta_1 \sin\theta_1 \cos\theta_2 \sin\theta_2 \sin\Phi$	-0.01472	0.02436
7	$\frac{1}{3}\cos\theta_2^2$	0.9967	1.076
8	$\frac{\sqrt{6}}{3}\sin\theta_1 \cos\theta_2 \sin\theta_2 \cos\Phi$	0.006234	-0.02481
9	$-\frac{\sqrt{6}}{3}\sin\theta_1 \cos\theta_2 \sin\theta_2 \sin\Phi$	0.0165	0.06494
10	$\frac{2}{\sqrt{3}}\cos\theta_1 \cos\theta_2^2$	-0.2959	-0.7187
11	$\frac{1}{3}\cos\theta_1^2$	0.8731	0.8054
12	$\frac{\sqrt{6}}{3}\sin\theta_1 \cos\theta_1 \sin\theta_2 \cos\Phi$	-0.0295	0.009665
13	$-\frac{\sqrt{6}}{3}\sin\theta_1 \cos\theta_1 \sin\theta_2 \sin\Phi$	-0.02833	0.003017
14	$\frac{2}{\sqrt{3}}\cos\theta_1^2 \cos\theta_2$	0.0007746	-0.03411
15	$\frac{2}{3}\cos\theta_1 \cos\theta_2$	0.003278	0.02569

Table 5.9: Angular terms (f_i) and their integrations over the data distributions for TOS (ξ_i^{TOS}) and not-TOS data sets ($\xi_i^{\text{not-TOS}}$). The integrals are normalised such that $(\xi_1 + \xi_2 + \xi_3 + \xi_7 + \xi_{11})/5 = 1$.

the polarisation amplitudes. It is assumed that the detector acceptance calculated from simulation matches that in data; this is tested in the following study.

In order to improve the agreement between data and simulation an iterative

data-driven reweighting procedure is applied [140]. This iteratively reweights the simulated helicity angles, B^0 p_{T} and final-state particle p_{T} in the simulation and calculates a new efficiency function each time until the method converges. For computational reasons the simulation is reweighted using the mass-independent PDF shown in Eqn. 3.13. It is assumed that the effect of the $m_{K\pi}$ acceptance is small, hence the effect of reweighting in this variable is negligible.

The efficiency function makes use of the *acceptance weights* method [141] to further reduce computation time. This method includes the effect of the detector acceptance into the fit by renormalising the theoretical PDF with the integrals of the angular terms

$$y(\vec{\Omega}) = \frac{g(\vec{\Omega})}{\sum_{i=1}^{15} h_i \xi_i} \, , \tag{5.2}$$

where $g(\vec{\Omega})$ is the theoretical PDF shown in Eqn. 3.16, h_i are the amplitude terms shown in Table 3.1 and ξ_i are the integrals of the angular terms, shown in Table 5.9, which are calculated from the data distributions. The integrals are normalised such that the average of the diagonal terms is one. Therefore, for a perfect acceptance the integral of each diagonal term is one and the integration of each interference term is zero.

The iterative reweighting is applied as follows:

1. Fit to data using Eqn. 3.13 and the acceptance weights calculated from the nominal simulation.
2. Reweight the simulation to have the same B^0 p_{T} as the data.
3. Reweight the simulation in the helicity angles, using the results of the previous fit.
4. Reweight the simulation to have the same final-state particle p_{T} as data.
5. Use this weighted simulation to recalculate the acceptance weights, with the results of the previous fit as input.
6. Use these new acceptance weights to refit the data.
7. Go back to step 3 and iterate until the fit to data converges.

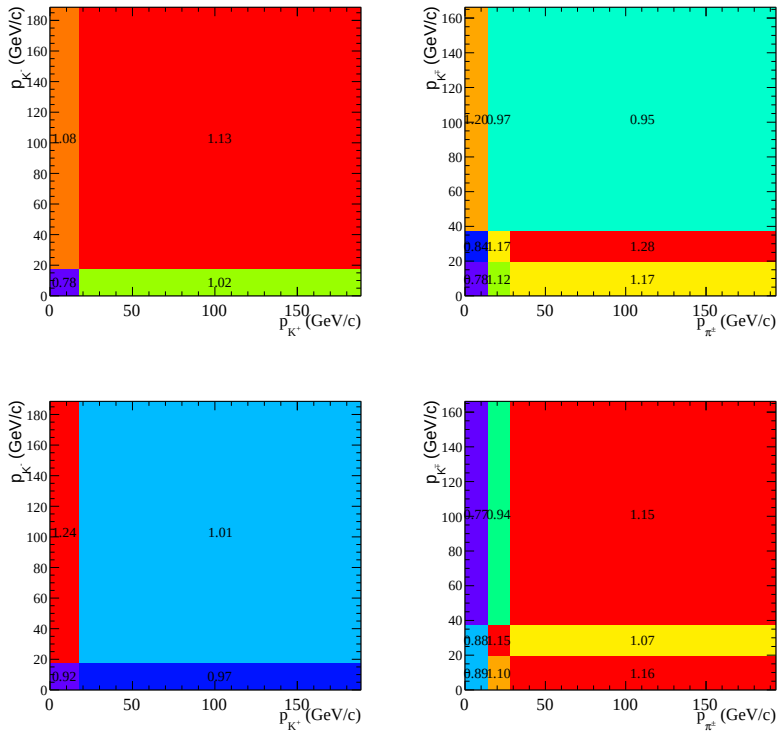

Figure 5.9: Ratio of K^+K^- momenta between data and simulation (left) and $K^+\pi^-$ momenta (right) for the not-TOS (top) and TOS sample (bottom). The values indicate the bin content.

For step 4 the momenta are reweighted using two 2D histograms, one containing the kaons from the ϕ meson and the other containing the $K^+\pi^-$ from the K^{*0} meson. These histograms are binned very coarsely, as shown in Fig. 5.9. This is due to limited simulation and data sample size and the relatively small phase space of these decays. The bin width is chosen so that roughly equal numbers of candidates fall into each bin. The TOS and not-TOS datasets have different kinematic distributions, therefore the reweighting is done separately for TOS and not-TOS candidates. Figure 5.10 shows the result of the reweighting on the pion p_{T} spectrum *cf.* Figure 5.8 without reweighting. Table 5.11 shows the fit results of a mass-independent fit for each iteration and Table 5.10 shows the effect the reweighting has on the acceptance weights.

TOS	B^0 p_{T}	It. 1	It. 2	It. 3	It. 4
ξ_1	0.863	0.8544	0.8553	0.8558	0.856
ξ_2	1.128	1.135	1.134	1.134	1.134
ξ_3	1.137	1.145	1.144	1.143	1.143
ξ_4	0.002017	0.001106	0.001097	0.001079	0.001071
ξ_5	-0.008553	-0.008783	-0.00868	-0.008643	-0.008626
ξ_6	-0.01664	-0.01657	-0.01679	-0.01686	-0.01689
ξ_7	0.9978	1.002	1.001	1.001	1.001
ξ_8	0.004383	0.00354	0.003715	0.003775	0.003811
ξ_9	0.01877	0.02056	0.02076	0.02087	0.02091
ξ_{10}	-0.2941	-0.3449	-0.3565	-0.3616	-0.3638
ξ_{11}	0.8744	0.8643	0.8652	0.8657	0.8659
ξ_{12}	-0.02796	-0.02736	-0.02735	-0.02733	-0.02733
ξ_{13}	-0.0293	-0.0291	-0.02911	-0.02912	-0.02911
ξ_{14}	-0.0006473	-0.006756	-0.005823	-0.005702	-0.005696
ξ_{15}	0.005598	0.005152	0.005013	0.004986	0.004992
not-TOS	B^0 p_{T}	It. 1	It. 2	It. 3	It. 4
ξ_1	0.7991	0.8162	0.8178	0.8187	0.819
ξ_2	1.158	1.15	1.149	1.148	1.147
ξ_3	1.16	1.143	1.142	1.141	1.141
ξ_4	-0.01895	-0.02427	-0.02445	-0.02453	-0.02456
ξ_5	-0.002054	-0.002173	-0.002158	-0.002153	-0.002148
ξ_6	0.02527	0.02119	0.02139	0.02145	0.02146
ξ_7	1.079	1.068	1.067	1.067	1.067
ξ_8	-0.02819	-0.02784	-0.02782	-0.02777	-0.02775
ξ_9	0.06665	0.05587	0.05588	0.05586	0.05585
ξ_{10}	-0.7119	-0.716	-0.7246	-0.7287	-0.7304
ξ_{11}	0.8038	0.8229	0.8245	0.8253	0.8256
ξ_{12}	0.008006	0.003103	0.003247	0.003324	0.003354
ξ_{13}	0.007378	0.01523	0.01498	0.01483	0.01477
ξ_{14}	-0.03559	-0.00666	-0.005602	-0.005508	-0.005519
ξ_{15}	0.02277	0.006751	0.006472	0.006504	0.006534

Table 5.10: Acceptance weights calculated at each stage of the iterative reweighting procedure.

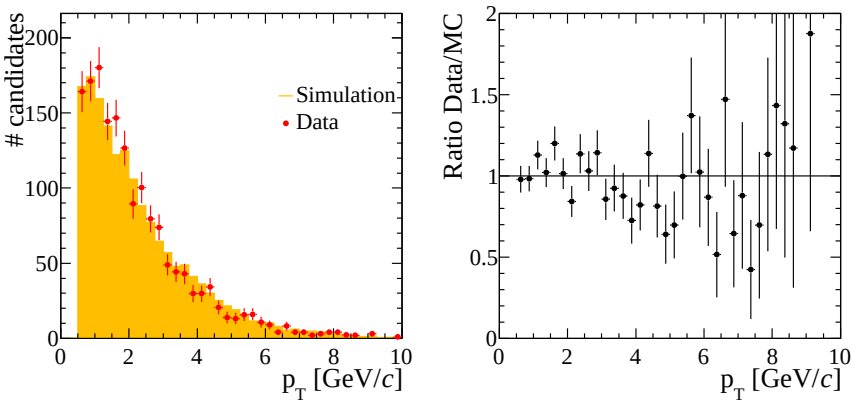

Figure 5.10: Comparison of the pion transverse momentum distribution between data (red points) and simulation (solid yellow) after the reweighting procedure. The simulation is normalised to the number of candidates seen in data.

The difference between a full mass-dependent fit using the nominal acceptance weights and a fit using the weights calculated from the final iteration is taken as an estimate of the systematic uncertainty and is shown in Table 5.12.

Parameter	Nominal	B^0 p_T	It. 1	It. 2	It. 3	It. 4
f_L	0.526	0.525	0.524	0.523	0.523	0.523
$f_\perp$	0.227	0.226	0.227	0.226	0.226	0.226
$f_S(K\pi)$	0.073	0.073	0.073	0.073	0.073	0.073
$f_S(KK)$	0.027	0.027	0.027	0.027	0.027	0.027
$\delta_\parallel$	2.615	2.615	2.602	2.596	2.593	2.592
$\delta_\perp$	2.681	2.681	2.669	2.664	2.662	2.660
$\delta_S(K\pi)$	1.895	1.900	1.864	1.849	1.842	1.839
$\delta_S(KK)$	2.083	2.082	2.092	2.091	2.091	2.091

Table 5.11: Fit results of a mass-independent fit using the weights calculated at each iteration (see Tab. 5.10). The fit is judged to have converged after the fourth iteration.

S-wave line shape

To probe the effect of the S-wave line shape on the fit results the fit is repeated using several alternative models. The $K^+\pi^-$ contribution uses the LASS

Parameter	Difference from nominal fit
$f_{\rm L}$	0.005
$f_\perp$	0.002
$f_{\rm S}(K\pi)$	0.0
$f_{\rm S}(KK)$	0.0
$\delta_\parallel$	0.013
$\delta_\perp$	0.010
$\delta_{\rm S}(K\pi)$	0.026
$\delta_{\rm S}(KK)$	0.005
$\mathcal{A}_\perp^{CP}$	0.001
$\mathcal{A}_0^{CP}$	0.002
$\mathcal{A}_{\rm S}(K\pi)^{CP}$	0.007
$\mathcal{A}_{\rm S}(KK)^{CP}$	0.007
$\delta_\parallel^{CP}$	0.005
$\delta_\perp^{CP}$	0.003
$\delta_{\rm S}(K\pi)^{CP}$	0.005
$\delta_{\rm S}(KK)^{CP}$	0.002

Table 5.12: Systematic uncertainties due to the difference in kinematic distributions between data and simulation.

parameterisation in the default fit. As alternatives both a relativistic spin-0 Breit-Wigner with mean and width of the $K_0^*(1430)$ meson [10] and a pure phase space model are tested. The latter is defined as [10]

$$\mathrm{d}\Phi_2 = \frac{1}{4(2\pi)^6 m_A} q(m_A, m_a, m_b) \ , \tag{5.3}$$

where q is defined in Eqn. 3.19.

The nominal fit parameterises the K^+K^- S-wave component as a Flatté distribution; as an alternative a phase space model is considered. The difference between each of the these models and the default fit is shown in Table 5.13 with the largest variation for each parameter taken as an estimate of the systematic uncertainty.

Parameter	BW(1430)	Phase space $K^+\pi^-$	Phase space K^+K^-
$f_{\rm L}$	0.0004	0.0001	0.0009
$f_\perp$	0.0006	0.0008	0.0001
$f_{\rm S}(K\pi)$	0.0004	0.0015	0.0004
$f_{\rm S}(KK)$	0.0002	0.0010	0.0030
$\delta_\parallel$	0.0139	0.0242	0.0059
$\delta_\perp$	0.0026	0.0257	0.0054
$\delta_{\rm S}(K\pi)$	0.0168	0.0624	0.0054
$\delta_{\rm S}(KK)$	0.0057	0.0158	0.0126
$\mathcal{A}_\perp^{CP}$	0.0067	0.0035	0.0011
$\mathcal{A}_0^{CP}$	0.0026	0.0037	0.0007
$\mathcal{A}_{\rm S}(K\pi)^{CP}$	0.0343	0.0036	0.0057
$\mathcal{A}_{\rm S}(KK)^{CP}$	0.0030	0.0017	0.0010
$\delta_\parallel^{CP}$	0.0011	0.0135	0.0007
$\delta_\perp^{CP}$	0.0035	0.0028	0.0003
$\delta_{\rm S}(K\pi)^{CP}$	0.0098	0.0205	0.0026
$\delta_{\rm S}(KK)^{CP}$	0.0016	0.0033	0.0021

Table 5.13: Difference from nominal fit when using alternative S-wave line shapes.

5.4 Triple product asymmetries

The triple products are defined in terms of the polarisation amplitudes and phases

$$\mathcal{A}_T^{(1)} = -\frac{4}{\pi}\frac{\mathcal{I}m(A_\perp A_\parallel^*)}{|A_0|^2+|A_\perp|^2+|A_\parallel|^2}\,, \tag{5.4}$$

$$\mathcal{A}_T^{(2)} = -\frac{2\sqrt{2}}{\pi}\frac{\mathcal{I}m(A_\perp A_0^*)}{|A_0|^2+|A_\perp|^2+|A_\parallel|^2}\,, \tag{5.5}$$

$$\mathcal{A}_T^{(3)} = -\sqrt{\frac{3}{2}}\left(\frac{\mathcal{I}m(A_\perp A_{\rm S}^{K\pi^*})\int_{m_{K\pi}^L}^{m_{K\pi}^H}\mathcal{M}_1(K\pi)\mathcal{M}_0(K\pi)\mathrm{d}m_{K\pi}}{F_{\rm P}+F_{\rm S}}\right)\,, \tag{5.6}$$

$$\mathcal{A}_T^{(4)} = -\sqrt{\frac{3}{2}}\left(\frac{\mathcal{I}m(A_\perp A_{\rm S}^{KK^*})\int_{m_{KK}^L}^{m_{KK}^H}\mathcal{M}_1(KK)\mathcal{M}_0(KK)\mathrm{d}m_{KK}}{F_{\rm P}+F_{\rm S}}\right)\,. \tag{5.7}$$

The results of the angular analysis are used to determine the true and fake triple products, as described in Sec. 3.3. These are shown in Table 5.14. All true TPAs are consistent with zero while all but one of the fake TPAs are significantly non-zero. The systematic uncertainty determination is discussed in Sec. 5.4.1.

Parameter	Fitted value
$A_{T(\text{true})}^{(1)}$	-0.007 ± 0.012
$A_{T(\text{true})}^{(2)}$	+0.004 ± 0.014
$A_{T(\text{true})}^{(3)}$	+0.004 ± 0.006
$A_{T(\text{true})}^{(4)}$	+0.002 ± 0.006
$A_{T(\text{fake})}^{(1)}$	-0.105 ± 0.012
$A_{T(\text{fake})}^{(2)}$	-0.017 ± 0.014
$A_{T(\text{fake})}^{(3)}$	-0.063 ± 0.006
$A_{T(\text{fake})}^{(4)}$	-0.019 ± 0.006

Table 5.14: Triple product asymmetries where the uncertainty is statistical only. Calculated from the fit results shown in Tab. 5.3.

5.4.1 Systematic uncertainties

For each study described in Sec. 5.3.1 the TPAs are recalculated. The effect of the mass model on the TPAs is shown in Table 5.15, results of the kinematic

reweighting in Table 5.16 and the result of using different S-wave line shapes is shown in Table 5.17. The uncertainty due to the efficiency function is zero because the simulation assumes that the acceptance does not depend on the charge of the final-state particles. The systematic uncertainties are summarised in Table 5.18.

Parameter	Double Gaussian	Polynomial background	ARGUS	Λ_b^0 background
$A_{T(\text{true})}^{(1)}$	0.0	0.0005	0.0004	0.0001
$A_{T(\text{true})}^{(2)}$	0.0002	0.0003	0.0	0.0005
$A_{T(\text{true})}^{(3)}$	0.0002	0.0	0.0	0.0004
$A_{T(\text{true})}^{(4)}$	0.0003	0.0	0.0002	0.0001
$A_{T(\text{fake})}^{(1)}$	0.0002	0.0003	0.0004	0.0017
$A_{T(\text{fake})}^{(2)}$	0.0001	0.0001	0.0008	0.0004
$A_{T(\text{fake})}^{(3)}$	0.0003	0.0	0.0006	0.0
$A_{T(\text{fake})}^{(4)}$	0.0004	0.0	0.0002	0.0002

Table 5.15: Difference between the nominal TPAs and those calculated using various signal and background models for a fit to the $K^+K^-K^+\pi^-$ mass.

Parameter	Difference from nominal fit
$A_{T(\text{true})}^{(1)}$	0.0005
$A_{T(\text{true})}^{(2)}$	0.0006
$A_{T(\text{true})}^{(3)}$	0.0002
$A_{T(\text{true})}^{(4)}$	0.0002
$A_{T(\text{fake})}^{(1)}$	0.0019
$A_{T(\text{fake})}^{(2)}$	0.0008
$A_{T(\text{fake})}^{(3)}$	0.0015
$A_{T(\text{fake})}^{(4)}$	0.0003

Table 5.16: Systematic uncertainties due to the difference in kinematic distributions in data and simulation.

Parameter	BW(1430)	Phase space $K^+\pi^-$	Phase space K^+K^-
$A_{T(\text{true})}^{(1)}$	0.0019	0.0002	0.0002
$A_{T(\text{true})}^{(2)}$	0.0006	0.0024	0.0001
$A_{T(\text{true})}^{(3)}$	0.0000	0.0001	0.0006
$A_{T(\text{true})}^{(4)}$	0.0001	0.0008	0.0000
$A_{T(\text{fake})}^{(1)}$	0.0003	0.0052	0.0014
$A_{T(\text{fake})}^{(2)}$	0.0027	0.0004	0.0002
$A_{T(\text{fake})}^{(3)}$	0.0002	0.0009	0.0051
$A_{T(\text{fake})}^{(4)}$	0.0028	0.0067	0.0002

Table 5.17: Differences between nominal fit and fits using alternative S-wave models.

Parameter	B^0 model	Data/MC difference	S-wave model	Total
$A_{T(\text{true})}^{(1)}$	0.0005	0.0005	0.002	0.002
$A_{T(\text{true})}^{(2)}$	0.0006	0.0005	0.002	0.002
$A_{T(\text{true})}^{(3)}$	0.0002	0.0003	0.001	0.001
$A_{T(\text{true})}^{(4)}$	0.0002	0.0003	0.001	0.001
$A_{T(\text{fake})}^{(1)}$	0.0019	0.0017	0.005	0.006
$A_{T(\text{fake})}^{(2)}$	0.0008	0.0008	0.003	0.003
$A_{T(\text{fake})}^{(3)}$	0.0015	0.0006	0.005	0.005
$A_{T(\text{fake})}^{(4)}$	0.0003	0.0004	0.007	0.007

Table 5.18: Summary of systematic uncertainties for the triple product asymmetries. The total is the quadratic sum of the individual contributions.

5.5 Direct CP asymmetry

5.5.1 Determination of direct CP asymmetry

The direct *CP* asymmetry is the difference in decay amplitudes between B^0 and $\overline{B}^0$, as discussed in Sec. 1.5.1. As the flavour of the B meson can be determined from the charge of the final-state pion, the direct *CP* asymmetry can be determined by studying the number of B^0 and $\overline{B}^0$ candidates at decay.

The raw asymmetry is thus defined as

$$A = \frac{N(\overline{B}^0) - N(B^0)}{N(\overline{B}^0) + N(B^0)} \,, \tag{5.8}$$

where $N(B^0)$ and $N(\overline{B}^0)$ are the number of B^0 and $\overline{B}^0$ candidates, respectively, determined from fits to M(KKKπ) after B^0 and $\overline{B}^0$ decays have been separated. A correction must be applied to this asymmetry because of the contamination from KK and $K\pi$ S-wave contributions

$$A = \frac{N(\overline{B}^0) \times (1 - \overline{F}_{\rm S}) - N(B^0) \times (1 - F_{\rm S})}{N(\overline{B}^0) \times (1 - \overline{F}_{\rm S}) + N(B^0) \times (1 - F_{\rm S})} \,. \tag{5.9}$$

The measured asymmetry A is related to the true asymmetry by

$$A_{CP} = A - \delta \quad \text{with} \quad \delta = A_{\rm D} + \kappa_d A_{\rm P} \,, \tag{5.10}$$

where $A_{\rm P}$ is the asymmetry due to the different rate of B^0 and $\overline{B}^0$ production at the LHC, κ_d is the dilution to this factor due to neutral B oscillations and $A_{\rm D}$ is the detection asymmetry between $K^+\pi^-$and $K^-\pi^+$ final states.

The control channel $B^0 \to J/\psi\, K^{*0}$ is used to determine the difference in asymmetries

$$\Delta A_{CP} = A_{CP}(\phi K^{*0}) - A_{CP}(J/\psi K^{*0}) \,, \tag{5.11}$$

because the production and detector asymmetries cancel out in the difference. If A_{CP} is zero in the tree-level $B^0 \to J/\psi\, K^{*0}$ decay then ΔA_{CP} is the direct *CP* asymmetry in $B^0 \to \phi K^{*0}$.

The decay $B^0 \to J/\psi\, K^{*0}$ is chosen as the control channel because of its high yield and similar decay topology. The sample of $B^0 \to J/\psi\, K^{*0}$ decays, where the

J/ψ decays to two oppositely charged muons, is selected in a similar manner to the $B^0 \to \phi K^{*0}$ decay. However, where the trigger decision is influenced by the muons from the J/ψ decay, the candidate is rejected.

The $\mu^+\mu^- K^+\pi^-$ mass distribution is fit using the same model as the $B^0 \to \phi K^{*0}$ decay, the partially reconstructed B decays are modelled using an ARGUS distribution and the $\Lambda_b^0 \to J/\psi p\pi^-$ contribution modelled using a shape obtained from simulation. The mass distribution with fit results overlayed are shown in Figure 5.11. A total of 15205 ± 130 $B^0 \to J/\psi\, K^{*0}$ candidates are observed.

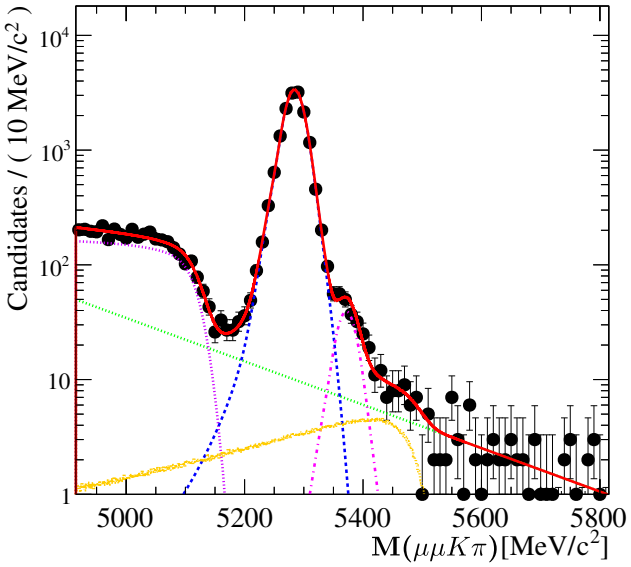

Figure 5.11: Mass distribution for selected $\mu^+\mu^- K^+\pi^-$ candidates. The $B^0 \to J/\psi\, K^{*0}$ contribution is shown in dotted blue and the $B_s^0 \to J/\psi\, K^{*0}$ as the purple dot-dashed line. The combinatorial background is shown as the dotted green line and the contribution from Λ_b^0 decays is shown in dotted orange. The total of all contributions is shown in solid red.

5.5.2 Direct CP results

The direct *CP* asymmetry is measured as described in Section 5.5.1, with separate measurements made for the TIS and TOS samples. Candidates which are accepted by both trigger decisions are included in both categories and any bias due to this is treated as a source of systematic uncertainty. The results from both trigger categories are combined in the final result.

The results of the angular analysis (Sec. 5.3) are used to correct for the $K\pi$ and KK S-wave fractions, the raw asymmetries are then determined to be

$$A^{\mathrm{TOS}}_{\phi K^*} = +0.014 \pm 0.043 \quad \text{and} \quad A^{\mathrm{TIS}}_{\phi K^*} = -0.002 \pm 0.040 \,, \tag{5.12}$$

which is related to the true asymmetry by Eqn. 5.10. To cancel the detector and production asymmetry, the difference in asymmetries between the $B^0 \to \phi K^{*0}$ and $B^0 \to J/\psi\, K^{*0}$ modes is taken, where the raw asymmetries for the latter are measured to be

$$A^{\mathrm{TOS}}_{J/\psi K^*} = -0.003 \pm 0.016 \quad \text{and} \quad A^{\mathrm{TIS}}_{J/\psi K^*} = -0.016 \pm 0.008 \,, \tag{5.13}$$

where the $K\pi$ S-wave in $B^0 \to J/\psi\, K^{*0}$ has not been considered.

The raw asymmetries are combined into a single measurement by taking a weighted average, where each measurement is weighted by its statistical uncertainty. To correct the uncertainty for double counting, the TIS sample is weighted by the error of the not-TOS sample

$$A^{\text{not-TOS}}_{\phi K^*} = 0.000 \pm 0.045 \,, \tag{5.14}$$

to give the correct overall asymmetry

$$A_{CP} = \frac{A^{\mathrm{TOS}}/\sigma^2(A^{\mathrm{TOS}}) + A^{\mathrm{TIS}}/\sigma^2(A^{\text{not-TOS}})}{1/\sigma^2(A^{\mathrm{TOS}}) + 1/\sigma^2(A^{\text{not-TOS}})} \,, \tag{5.15}$$

where $\sigma(A^{\mathrm{TOS}})$ and $\sigma(A^{\text{not-TOS}})$ are the statistical uncertainties of the TOS and not-TOS samples. The error on A_{CP} is given by

$$\sigma(A_{CP}) = \frac{1}{\sqrt{1/\sigma^2(A^{\mathrm{TOS}}) + 1/\sigma^2(A^{\text{not-TOS}})}} \,. \tag{5.16}$$

Using the raw asymmetries from $B^0 \to \phi K^{*0}$ and $B^0 \to J/\psi\, K^{*0}$, the difference in CP asymmetries can be calculated as shown in Eqn. 5.11 to be

$$\Delta A_{CP} = (+1.5 \pm 3.2)\% \,, \tag{5.17}$$

where the uncertainty is statistical only. The systematic uncertainty determination is discussed in the next section.

5.5.3 Systematic uncertainties

The systematic uncertainties on the direct *CP* asymmetry are related to the trigger and the kinematic differences between daughter particles in each mode. The systematic uncertainties are summarised in Table 5.19 and described in detail in the following sections.

Source	Uncertainty (%)
Double counting	0.10
TOS trigger	0.25
Kaon p_{T}	0.29
B^0 p_{T}	0.23
B^0 mass model	0.30
Total	0.547

Table 5.19: Summary of systematic uncertainties on the direct *CP* asymmetry. The total is the quadratic sum of the individual uncertainties.

Difference in kinematic variables

Differences in the kinematic distributions are observed between the signal and control channels, this is due to the difference between the J/ψ and ϕ meson masses. These effects are investigated as a source of systematic uncertainty.

The B^0, kaon and pion p_{T} spectrums for the signal and control channel are compared in Fig. 5.12, where the kaon is the decay product of the K^{*0}. The separate TOS and not-TOS momentum distributions are studied in Appendix C.2 and although small discrepancies are found this is assumed to be negligible compared to the overall difference. As the ϕ meson decays into two charged kaons, it cannot introduce a detection asymmetry and is not examined in this study. Similarly, as the J/ψ is not used in the trigger decision, it cannot introduce a detection asymmetry.

It can be seen from Fig. 5.12 that the pion p_{T} distributions are similar, however this is not the case for the B^0 and K^+ spectra. To see if this difference affects the fit results, the $B^0 \to J/\psi K^{*0}$ sample is reweighted to have the same B^0 p_{T} distribution as $B^0 \to \phi K^{*0}$ and the direct *CP* measurement is repeated.

The difference between this result and the nominal result is taken as a systematic uncertainty. The process is then repeated for the K^+ p_{T}. Using

this method the systematic uncertainties are calculated to be 0.29% and 0.25% for the K^+ and B^0 p_{T} spectrums, respectively.

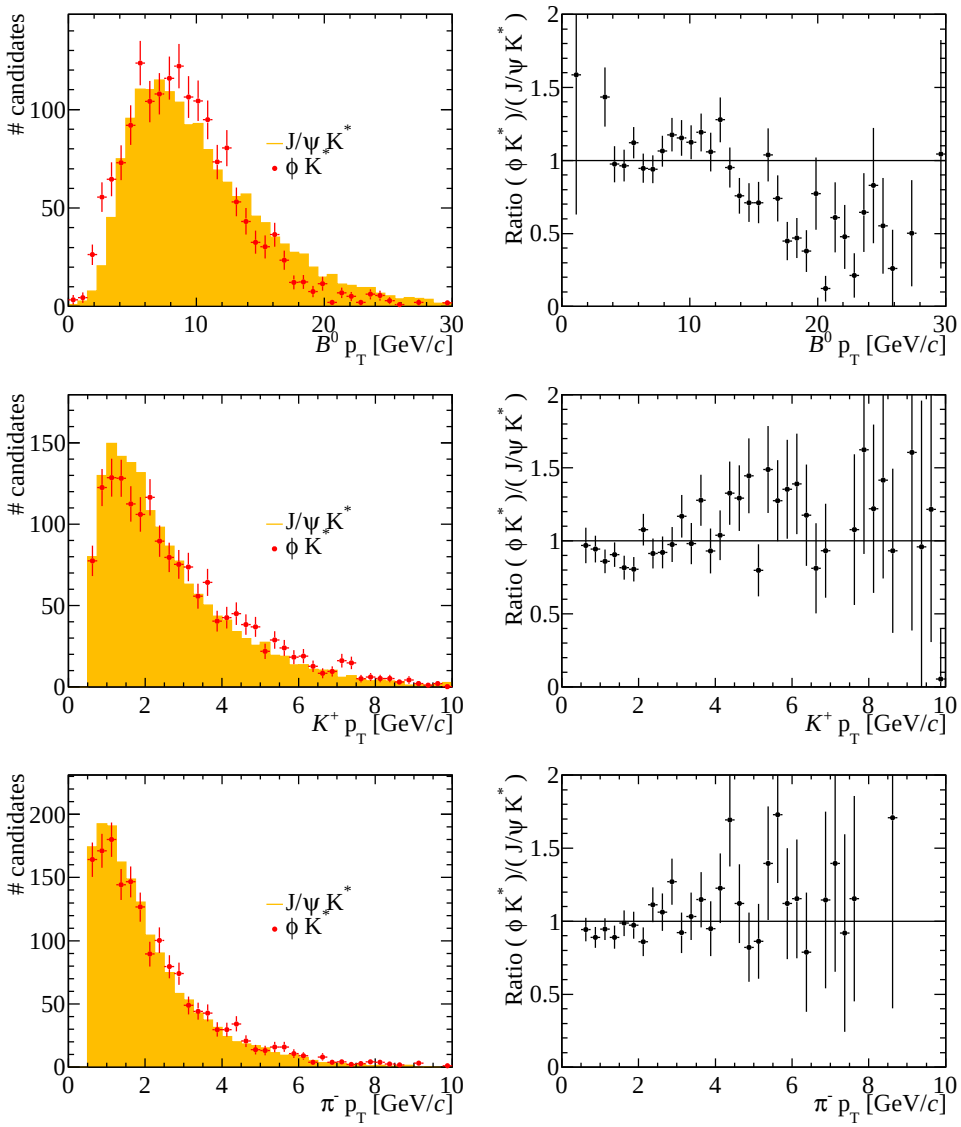

Figure 5.12: Top: B^0 p_{T} distribution from $B^0 \to \phi K^{*0}$ (filled dots) and $B^0 \to J/\psi\, K^{*0}$ (filled histogram) data with the ratio of these shown on the right. Middle: Kaon from K^{*0} p_{T} distribution. Bottom: Pion p_{T} distribution.

Trigger lines

The candidates in the TIS trigger category are recorded based on information which does not come from the signal decay and can be separated into two main

Source	$B^0 \to \phi K^{*0}$	$B^0 \to J/\psi\, K^{*0}$
Muon chamber	$(35.8 \pm 1.5)\%$	$(35.7 \pm 0.4)\%$
HCAL	$(48.9 \pm 1.6)\%$	$(52.3 \pm 0.4)\%$

Table 5.20: Relative fraction of TIS trigger category events stored based on information from the HCAL and muon stations.

categories. Those recorded based on information from the HCAL and those stored based on information from the muon chambers. The ECAL is not used in the TOS trigger decision for this analysis. The fraction of each category is shown in Table 5.20 for the signal and control channel. As the fractions are equal for the signal and control channel, any asymmetry induced by the trigger cancels in the difference.

Since the TIS and TOS trigger categories are not statistically independent, a study is performed to see if this biases the direct *CP* measurement. The measurement is repeated after removing the double counted events from the TIS category. The difference between this and the nominal result is taken as a systematic uncertainty which is found to be 0.10%.

As discussed in Sec. 5.5.1, the TOS candidates in $B^0 \to J/\psi\, K^{*0}$ do not use the muons in the trigger decision. Therefore, all TOS candidates in this channel were recorded based on information from the K^+ or π^- from the K^{*0} decay. In the $B^0 \to \phi K^{*0}$ decay however, the TOS candidates can be recorded based on information from the K^+K^- or $K^+\pi^-$ pair. This leads to 67.1% of $B^0 \to J/\psi\, K^{*0}$ decays being recorded based on information from the kaon from the K^{*0} decay, while for $B^0 \to \phi K^{*0}$ it is 43.2%. A possible detection asymmetry maybe be introduced by this which will not cancel when the difference in asymmetries between the two modes is taken.

The detection asymmetry between K^+ and K^- and π^+ and π^- is shown in Fig. 5.13. These efficiencies are calculated using well identified kaons and pions from $D^{*+} \to D^0(K^-\pi^+)\pi^+$ decays.

Although the detection asymmetry is negligible in pions above $500\,\mathrm{MeV}/c$ (see selection in Sec 4.2), there is a small asymmetry for low momentum kaons. To evaluate any associated systematic uncertainty, the signal and background samples are corrected using the efficiency shown in Fig. 5.13. The ΔA_{CP} measurement is repeated with the corrected sample and the difference from the

nominal result is taken as a systematic uncertainty. This is found to be 0.25%.

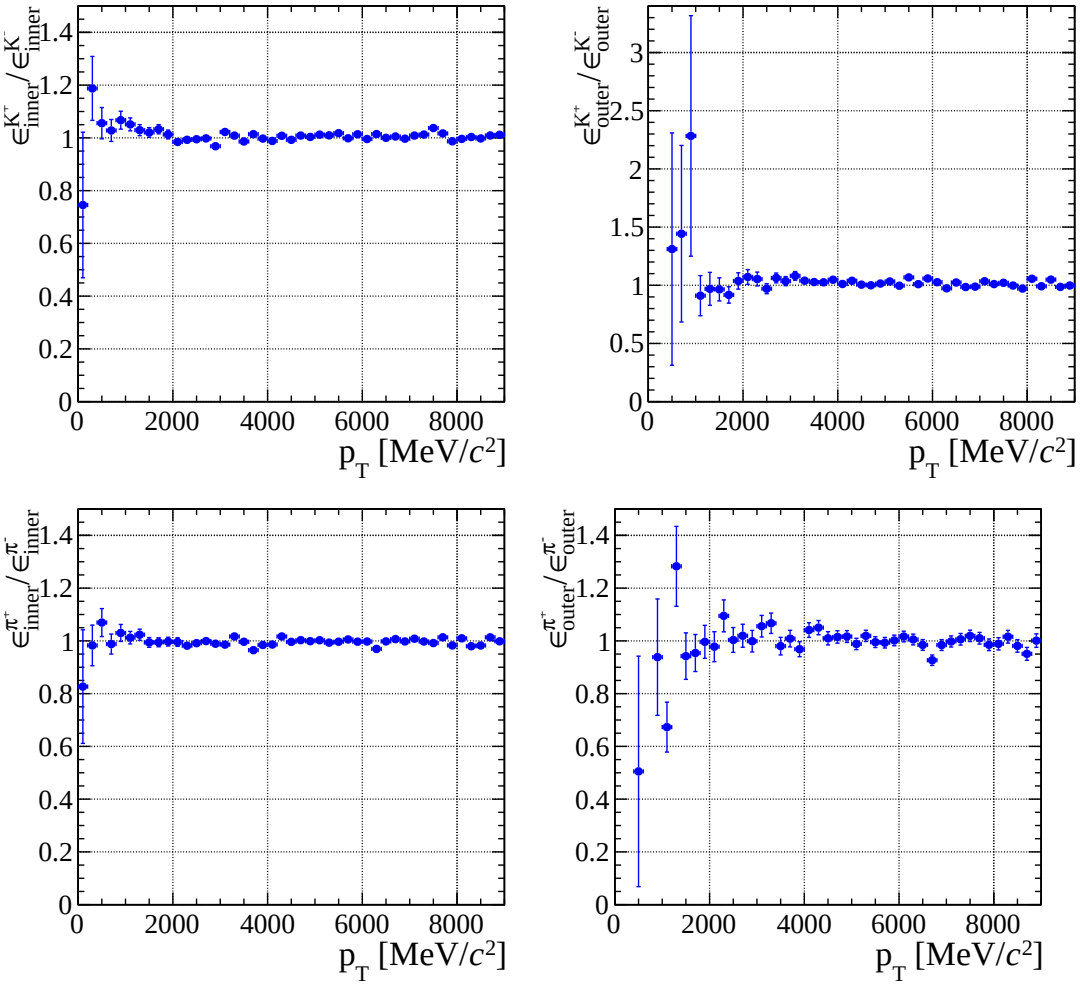

Figure 5.13: Top: Detection asymmetry ratio between K^+ and K^- mesons in the inner (left) and outer (right) regions of the HCAL as a function of p_{T}. Bottom: Detection asymmetry ratio between π^+ and π^- mesons in the inner (left) and outer (right) regions of the HCAL as a function of p_{T}.

$\mathbf{B^0}$ mass model

The B^0 mass model is used to determine the yields for the A_{CP} calculations. To estimate the systematic uncertainty due to the mass model, the signal and background models are varied as described in Sec. 5.3.1. Using a double Gaussian signal model or including the low mass background in the fit has no effect on the A_{CP} calculation. The linear background model and Λ_b^0 contributions introduce a systematic uncertainty of 0.2% and 0.3%, respectively. The larger of the two is chosen as an estimate of the systematic uncertainty due to the B^0 mass model. The systematic uncertainties are summarised in Table 5.19.

5.6 Validation of fit results

5.6.1 Comparison of TOS and not-TOS ratios

In Section 4.5 the detector acceptance correction is discussed and Section 4.2.1 discusses the TIS, TOS and not-TOS trigger categories. As separate efficiency functions are calculated for TOS and not-TOS candidates, the efficiency is independent of the relative TOS and not-TOS fractions in data and simulation. However, the fraction of events which are both TOS and TIS is important because a choice is made about where to place these events. Therefore, the following ratio is important

$$z = \frac{N(\text{TOS\&\&TIS})}{N(\text{TOS})} \,, \tag{5.18}$$

where N(TOS&&TIS) is the number of events which are both TOS and TIS and N(TOS) is the number of events which are TOS. This ratio is shown for data and simulation in Table 5.21 together with the overall TOS and TIS fractions, where the signal has been separated using the *sPlot* technique (see Sec. 4.3.2). As the ratio in Equation 5.18 is the same for data and simulation no further action is taken.

	TOS (%)	TIS (%)	z
Data	45.1 ± 3.0	54.9 ± 3.0	31.3 ± 1.2
Simulation	53.4 ± 0.6	46.6 ± 0.6	30.0 ± 0.2

Table 5.21: TOS and TIS fractions in data and simulation. The ratio z is defined in Equation 5.18.

5.6.2 Fit putting overlap events into the not-TOS category

In this analysis, events which are accepted by the TOS and TIS trigger categories are placed into the TOS data sample. An additional check is performed by moving these events into the other category and recalculating the detector acceptance, giving the results shown in Table 5.22. As this result is very similar to the main result, no systematic uncertainty is assigned.

Parameter	Result
f_{L}	0.497 ± 0.019
$f_{\perp}$	0.222 ± 0.016
$f_{\mathrm{S}}(K\pi)$	0.143 ± 0.013
$f_{\mathrm{S}}(KK)$	0.121 ± 0.013
$\delta_{\parallel}$	2.565 ± 0.070
$\delta_{\perp}$	2.632 ± 0.063
$\delta_{\mathrm{S}}(K\pi)$	2.224 ± 0.062
$\delta_{\mathrm{S}}(KK)$	2.479 ± 0.072
$\mathcal{A}_0^{CP}$	-0.001 ± 0.038
$\mathcal{A}_{\perp}^{CP}$	0.045 ± 0.073
$\mathcal{A}_{\mathrm{S}}(K\pi)^{CP}$	0.063 ± 0.088
$\mathcal{A}_{\mathrm{S}}(KK)^{CP}$	-0.213 ± 0.105
$\delta_{\perp}^{CP}$	0.060 ± 0.062
$\delta_{\parallel}^{CP}$	0.041 ± 0.069
$\delta_{\mathrm{S}}(K\pi)^{CP}$	0.062 ± 0.062
$\delta_{\mathrm{S}}(KK)^{CP}$	0.025 ± 0.071

Table 5.22: Result of a fit performed using a new efficiency and moving events which fall into both the TOS and TIS categories into the TIS category. The uncertainty is statistical only.

5.6.3 Fitting data in subsamples

This section fits the data in subsamples. A TOS/not-TOS comparison is a good test of the calculated detector acceptance while fitting data taken with opposite magnet polarity probes differences between the $K^+\pi^-$ and $K^-\pi^+$ final states. The TOS/not-TOS fit results are compared in Table 5.23 and the results from each magnet polarity are compared in Table 5.24. In general the agreement is good; some tension is seen, for instance in $f_\perp$ but this is covered by the systematic uncertainty.

Parameter	TOS	not-TOS
f_L	0.509 ± 0.025	0.487 ± 0.029
$f_\perp$	0.209 ± 0.022	0.239 ± 0.025
$f_\mathrm{S}(K\pi)$	0.133 ± 0.016	0.145 ± 0.018
$f_\mathrm{S}(KK)$	0.100 ± 0.016	0.143 ± 0.020
$\delta_\parallel$	2.447 ± 0.080	2.660 ± 0.089
$\delta_\perp$	2.460 ± 0.079	2.807 ± 0.088
$\delta_\mathrm{S}(K\pi)$	2.215 ± 0.080	2.248 ± 0.095
$\delta_\mathrm{S}(KK)$	2.276 ± 0.101	2.683 ± 0.100
$\mathcal{A}_\perp^{CP}$	0.022 ± 0.100	0.145 ± 0.095
$\mathcal{A}_0^{CP}$	-0.035 ± 0.048	0.021 ± 0.058
$\mathcal{A}_\mathrm{S}(K\pi)^{CP}$	0.110 ± 0.111	0.032 ± 0.115
$\mathcal{A}_\mathrm{S}(KK)^{CP}$	-0.318 ± 0.146	-0.073 ± 0.137
$\delta_\parallel^{CP}$	0.130 ± 0.078	-0.102 ± 0.088
$\delta_\perp^{CP}$	0.086 ± 0.077	-0.005 ± 0.087
$\delta_\mathrm{S}(K\pi)^{CP}$	0.214 ± 0.074	-0.158 ± 0.092
$\delta_\mathrm{S}(KK)^{CP}$	0.047 ± 0.099	-0.058 ± 0.098

Table 5.23: Results of a fit to TOS data (left) and not-TOS data (right). The uncertainty is statistical only.

Parameter	Magnet up	Magnet down
f_{L}	0.478 ± 0.026	0.514 ± 0.031
$f_{\perp}$	0.259 ± 0.023	0.168 ± 0.025
$f_{\mathrm{S}}(K\pi)$	0.173 ± 0.018	0.117 ± 0.017
$f_{\mathrm{S}}(KK)$	0.117 ± 0.016	0.127 ± 0.023
$\delta_{\parallel}$	2.667 ± 0.087	2.459 ± 0.086
$\delta_{\perp}$	2.692 ± 0.081	2.579 ± 0.093
$\delta_{\mathrm{S}}(K\pi)$	2.249 ± 0.080	2.260 ± 0.106
$\delta_{\mathrm{S}}(KK)$	2.464 ± 0.098	2.503 ± 0.103
$\mathcal{A}_{\perp}^{CP}$	0.052 ± 0.085	0.134 ± 0.295
$\mathcal{A}_{0}^{CP}$	-0.039 ± 0.053	0.018 ± 0.059
$\mathcal{A}_{\mathrm{S}}(K\pi)^{CP}$	0.138 ± 0.094	-0.008 ± 0.132
$\mathcal{A}_{\mathrm{S}}(KK)^{CP}$	-0.194 ± 0.136	-0.185 ± 0.167
$\delta_{\parallel}^{CP}$	-0.054 ± 0.085	0.104 ± 0.084
$\delta_{\perp}^{CP}$	-0.002 ± 0.080	0.092 ± 0.090
$\delta_{\mathrm{S}}(K\pi)^{CP}$	-0.029 ± 0.079	0.123 ± 0.101
$\delta_{\mathrm{S}}(KK)^{CP}$	-0.082 ± 0.095	0.077 ± 0.099

Table 5.24: Results of a fit to magnet up data (left) and magnet down data (right). The uncertainty is statistical only.

5.7 Discussion of results

Using $1\,\text{fb}^{-1}$ collected by the LHCb detector in 2011, results are presented for the polarisation amplitudes, triple product asymmetries and direct *CP* asymmetry in the $B^0 \to \phi K^{*0}$ decay mode. The results for the polarisation amplitudes are shown in Table 5.25 and confirm equal amounts of longitudinal and transverse polarisation. Significant S-wave fractions are observed below the ϕ and K^{*0} resonances while all *CP* asymmetries are consistent with zero.

Parameter	Fitted value
f_L	$0.497 \pm 0.019 \pm 0.015$
$f_\perp$	$0.221 \pm 0.016 \pm 0.013$
$f_\text{S}(K\pi)$	$0.143 \pm 0.013 \pm 0.012$
$f_\text{S}(KK)$	$0.122 \pm 0.013 \pm 0.008$
$\delta_\perp$	$2.633 \pm 0.062 \pm 0.037$
$\delta_\parallel$	$2.562 \pm 0.069 \pm 0.040$
$\delta_\text{S}(K\pi)$	$2.222 \pm 0.063 \pm 0.081$
$\delta_\text{S}(KK)$	$2.481 \pm 0.072 \pm 0.048$
$\mathcal{A}_0^{CP}$	$-0.003 \pm 0.038 \pm 0.005$
$\mathcal{A}_\perp^{CP}$	$+0.047 \pm 0.074 \pm 0.009$
$\mathcal{A}_\text{S}(K\pi)^{CP}$	$+0.073 \pm 0.091 \pm 0.035$
$\mathcal{A}_\text{S}(KK)^{CP}$	$-0.209 \pm 0.105 \pm 0.012$
$\delta_\perp^{CP}$	$+0.062 \pm 0.062 \pm 0.005$
$\delta_\parallel^{CP}$	$+0.045 \pm 0.069 \pm 0.015$
$\delta_\text{S}(K\pi)^{CP}$	$+0.062 \pm 0.062 \pm 0.022$
$\delta_\text{S}(KK)^{CP}$	$+0.022 \pm 0.072 \pm 0.004$

Table 5.25: Results of the angular analysis, where the uncertainties are statistical and systematic, respectively.

The triple product asymmetries are determined from the results of the angular fit and are shown in Table 5.26. All true asymmetries are consistent with zero, showing no evidence of physics beyond the Standard Model. Conversely, all but one of the fake TPAs show significant deviations from zero indicating the presence of final-state interactions.

Additionally, the difference in direct *CP* asymmetries between $B^0 \to \phi K^{*0}$ and $B^0 \to J/\psi\, K^{*0}$ is measured to be

$$\Delta A_{CP} = (+1.5 \pm 3.2 \pm 0.5)\% \,, \tag{5.19}$$

Parameter	Fitted value
$A^{(1)}_{T(\text{true})}$	$-0.007 \pm 0.012 \pm 0.002$
$A^{(2)}_{T(\text{true})}$	$+0.004 \pm 0.014 \pm 0.002$
$A^{(3)}_{T(\text{true})}$	$+0.004 \pm 0.006 \pm 0.001$
$A^{(4)}_{T(\text{true})}$	$+0.002 \pm 0.006 \pm 0.001$
$A^{(1)}_{T(\text{fake})}$	$-0.105 \pm 0.012 \pm 0.006$
$A^{(2)}_{T(\text{fake})}$	$-0.017 \pm 0.014 \pm 0.003$
$A^{(3)}_{T(\text{fake})}$	$-0.063 \pm 0.006 \pm 0.005$
$A^{(4)}_{T(\text{fake})}$	$-0.019 \pm 0.006 \pm 0.007$

Table 5.26: Triple product asymmetries, where the uncertainties are statistical and systematic, respectively.

where the uncertainties are statistical and systematic, respectively. This is consistent with the Standard Model expectation of approximately zero *CP* violation.

In the following chapter these results are compared with previous measurements. Also a study is described which estimates the sensitivity LHCb will be able to achieve for these measurements using $3\,\text{fb}^{-1}$ of integrated luminosity, corresponding to the sum collected by the LHCb detector in the 2011 and 2012 LHC runs.

Chapter 6

Future prospects and conclusion

6.1 Comparison with previous measurements

Prior to the study presented here, measurements of the polarisation amplitudes have been published by the BaBar [83] and Belle [86] collaborations. A comparison of the main results is shown in Table 6.1.

Parameter	LHCb	BaBar	Belle
$f_{\rm L}$	$0.497 \pm 0.019 \pm 0.015$	$0.494 \pm 0.034 \pm 0.013$	$0.499 \pm 0.030 \pm 0.018$
$f_\perp$	$0.221 \pm 0.016 \pm 0.013$	$0.212 \pm 0.032 \pm 0.013$	$0.238 \pm 0.026 \pm 0.008$
$\delta_\perp$	$2.633 \pm 0.062 \pm 0.037$	$2.35 \pm 0.13 \pm 0.09$	$2.37 \pm 0.10 \pm 0.04$
$\delta_\parallel$	$2.562 \pm 0.069 \pm 0.040$	$2.40 \pm 0.13 \pm 0.08$	$2.23 \pm 0.10 \pm 0.02$
$\mathcal{A}_0^{CP}$	$-0.003 \pm 0.038 \pm 0.005$	$+0.01 \pm 0.07 \pm 0.02$	$-0.030 \pm 0.061 \pm 0.007$
$\mathcal{A}_\perp^{CP}$	$+0.047 \pm 0.072 \pm 0.009$	$-0.04 \pm 0.15 \pm 0.06$	$-0.14 \pm 0.11 \pm 0.01$
$\delta_\perp^{CP}$	$+0.062 \pm 0.062 \pm 0.006$	$+0.21 \pm 0.13 \pm 0.08$	$+0.05 \pm 0.10 \pm 0.02$
$\delta_\parallel^{CP}$	$+0.045 \pm 0.068 \pm 0.015$	$+0.22 \pm 0.12 \pm 0.08$	$-0.02 \pm 0.10 \pm 0.01$

Table 6.1: Comparison of measurements made by the LHCb [120], BaBar [83] and Belle [86] collaborations. The first uncertainty is statistical and the second systematic.

The P-wave polarisation amplitudes and *CP*-violating parameters show good agreement between experiments, while a small difference is observed in the P-wave phases; this is discussed later. The S-wave results are not compared since each experiment considers this contribution differently. The BaBar measurement fully models the $K^+\pi^-$ S-wave but subtracts the K^+K^- S-wave using a fit to m_{KK}. They include a systematic uncertainty associated with the subtraction. In contrast, the measurement from Belle includes both the $K^+\pi^-$ and K^+K^-

Parameter	No K^+K^- S-wave	No K^+K^- S-wave interference	No S-wave
f_{L}	0.536 ± 0.017	0.510 ± 0.020	0.559 ± 0.015
$f_{\perp}$	0.204 ± 0.015	0.213 ± 0.017	0.186 ± 0.014
$\delta_{\perp}$	2.629 ± 0.058	2.634 ± 0.072	2.638 ± 0.053
$\delta_{\parallel}$	2.525 ± 0.057	2.591 ± 0.076	2.494 ± 0.056
$\mathcal{A}_0^{CP}$	$+0.004 \pm 0.032$	-0.002 ± 0.038	$+0.007 \pm 0.027$
$\mathcal{A}_{\perp}^{CP}$	$+0.036 \pm 0.071$	$+0.042 \pm 0.080$	$+0.010 \pm 0.070$
$\delta_{\perp}^{CP}$	$+0.023 \pm 0.057$	$+0.021 \pm 0.071$	$+0.068 \pm 0.052$
$\delta_{\parallel}^{CP}$	-0.028 ± 0.057	-0.042 ± 0.075	$+0.047 \pm 0.055$

Table 6.2: Comparison of measurements made by the LHCb when the K^+K^- S-wave is not considered, when the K^+K^- S-wave interference is not considered and when neither S-wave is considered. The uncertainty is statistical only.

S-wave contributions but does not allow interference between the K^+K^- S- and P-wave components in their nominal result. They include the interference terms as a systematic check. Thus, this measurement is the first to include both the $K^+\pi^-$ and K^+K^- S-waves and their interference.

For comparison this analysis is repeated with similar constraints on the S-wave as the previous experiments with the results shown in Table 6.2. Including both S-waves in the fit affects the P-wave phases which might explain the small differences observed between experiments.

The Belle measurement is based on approximately 1100 signal candidates while both the BaBar and LHCb measurements are based on approximately 1700 signal candidates. However, the $K^+\pi^-$ mass range used varies with each analysis, thus affecting the fraction of P-wave candidates in the signal region. The BaBar and Belle measurements consider $K^+\pi^-$ masses up to $1.55\,\mathrm{GeV}/c^2$ which allows them to include not only the P- and S-wave contributions but also $B^0 \to \phi K_2^*(1430)$ which is D-wave (spin-2). The LHCb measurement only considers masses up to approximately $1\,\mathrm{GeV}/c^2$ meaning the D-wave component, which is very narrow, can be safely ignored. This results in LHCb having the largest sample of $B^0 \to \phi K^*(892)^0$ candidates, allowing the most precise measurements of the P-wave parameters as shown in Table 6.1.

These results disagree with the naive prediction and the results from Yang *et al.* [93] which predict a dominant longitudinal polarisation. The approach taken by Beneke *et al.* [50] and Cheng *et al.* [95] in the QCD factorisation framework predicts a longitudinal polarisation fraction which is in good agreement with that

seen in data, however these predictions suffer from large uncertainties. Finally, the prediction by Chua *et al.* [98], which includes rescattering from charm resonances, produces a longitudinal polarisation which is in good agreement with the data but a perpendicular fraction which is too low. Finally, the predictions from Nandi *et al.* [142] use polarisations and branching fractions from Ref [143] as input and are in agreement with these new results.

	LHCb	BaBar	Belle
Direct *CP*	$(+1.5 \pm 3.2 \pm 0.5)\%$	$(+1 \pm 6 \pm 3)\%$	$(-0.7 \pm 4.8 \pm 2.1)\%$

Table 6.3: Comparison of direct *CP* measurements by the LHCb [120], BaBar [83] and Belle [86] collaborations. The first uncertainty is statistical and the second systematic.

The measurement of the direct *CP* asymmetry is compared in Table 6.3 and the TPAs are compared in Table 6.4, where the latter uses older results from the Belle and BaBar collaborations because the most recent results do not include these calculations [82, 85]. For all experiments the direct *CP* and true triple product asymmetries are consistent with zero. BaBar did not measure the fake TPAs but Belle report hints of a non-zero fake TPA, although not the same one as LHCb. This could be due to the fact that Belle do not include all of the S-wave interference terms thus biasing the triple products (which are proportional to interference terms). The LHCb result confirms the presence of final-state interactions.

	LHCb	BaBar	Belle
$A^{(1)}_{T(\text{true})}$	$-0.007 \pm 0.012 \pm 0.002$	$-0.02 \pm 0.04 \pm 0.01$	$+0.01 \pm 0.10 \pm 0.02$
$A^{(2)}_{T(\text{true})}$	$+0.004 \pm 0.014 \pm 0.002$	$+0.11 \pm 0.05 \pm 0.01$	$+0.16^{+0.16}_{-0.14} \pm 0.03$
$A^{(1)}_{T(\text{fake})}$	$-0.105 \pm 0.012 \pm 0.006$	-	$-0.06 \pm 0.10 \pm 0.01$
$A^{(2)}_{T(\text{fake})}$	$-0.017 \pm 0.014 \pm 0.003$	-	$-0.41^{+0.16}_{-0.14} \pm 0.04$

Table 6.4: Comparison of the triple product asymmetries measured by the LHCb [120], BaBar [82] and Belle [85] collaborations. The first uncertainty is statistical and the second systematic.

6.2 Future prospects

6.2.1 Preliminary mass fit using $3\,\text{fb}^{-1}$

A preliminary analysis has been carried out using the combined 2011+2012 dataset collected by LHCb. This dataset combines $2\,\text{fb}^{-1}$ collected in 2012 at a centre-of-mass energy of $\sqrt{s} = 8\,\text{TeV}$ with $1\,\text{fb}^{-1}$ collected in 2011 at $\sqrt{s} = 7\,\text{TeV}$.

The 2011 and 2012 samples are combined and have the same selection applied as that discussed in Sec. 4.2. The GL is retrained using a background sample taken from the combination of 2011 and 2012 data samples and the signal sample is taken from the same simulation sample used to train the GL in the $1\,\text{fb}^{-1}$ analysis. After the selection 5897 candidates remain.

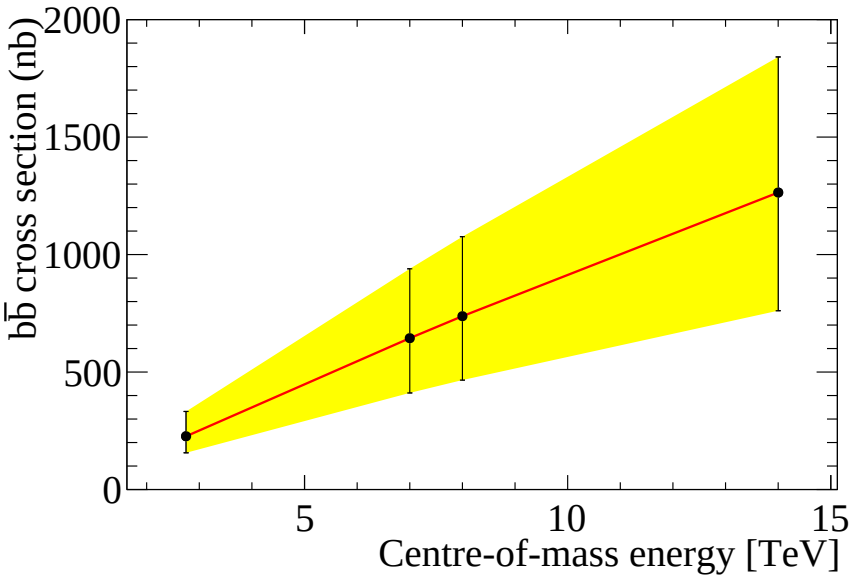

Figure 6.1: Visible cross section of $b\bar{b}$ at LHCb as a function of centre-of-mass energy [144]. The red line is an extrapolation between data points and the yellow shaded area is the uncertainty.

Figure 6.1 shows the visible $b\bar{b}$ cross section at LHCb as a function of energy at the LHC. An increase in energy from 7 to 8 TeV corresponds to an increase in cross section of 14.5% [144]. The 2012 data should therefore contain more than twice as many signal events as the 2011 based on the integrated luminosity and increase in energy. Assuming the selection efficiency is the same for both samples this corresponds to a total of 5445 ± 105 signal candidates in $3\,\text{fb}^{-1}$ where the

uncertainty is propagated from the number of signal candidates in 2011.

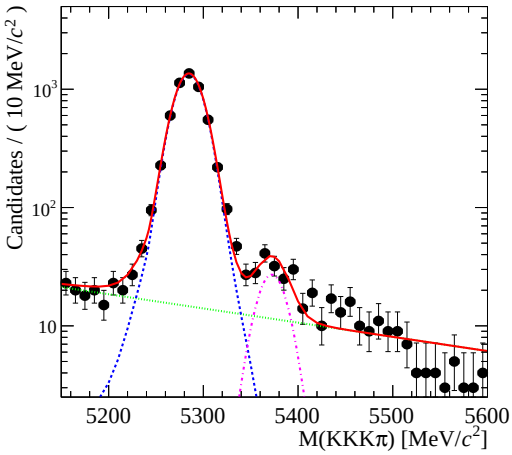

Figure 6.2: Mass distribution for selected $K^+K^-K^+\pi^-$ candidates in $3\,\text{fb}^{-1}$. A fit to the model described in Sec 4.4 is superimposed (red). The signal contribution is shown as the blue dotted line. The $B_s^0 \to \phi\overline{K}^*$ contribution is shown as the purple dot-dashed line and the combinatorial background is shown as the green dotted line.

A fit to the $K^+K^-K^+\pi^-$ mass is shown in Figure 6.2 with results shown in Table 6.5. The fit determines 5289 ± 75 signal candidates, in good agreement with the expectation. Also noteworthy is the width of the Crystal Ball function, which is $1\,\text{MeV}/c^2$ narrower than the 2011 dataset. This is due to improvements in the software which determines the detector alignment from track data.

Parameter	Value
$M(\,\text{MeV}/c^2)$	5284.8 ± 0.2
$\sigma(\,\text{MeV}/c^2)$	14.7 ± 0.2
N_{Bd}	5289 ± 75
N_{Bs}	107 ± 15

Table 6.5: Results of a mass fit to $3\,\text{fb}^{-1}$ of data using the model described in Sec. 4.4.

6.2.2 Expected sensitivity of angular analysis

In the previous section a preliminary fit of the $K^+K^-K^+\pi^-$ mass spectrum is performed using $3\,\text{fb}^{-1}$ of integrated luminosity, with the results shown in

Table 6.5. To estimate the sensitivity on the polarisation amplitudes using this sample, pseudo-experiments are used.

Parameter	Generated value	Absolute uncertainty $3\,\text{fb}^{-1}$ (%)	Relative uncertainty $3\,\text{fb}^{-1}$ (%)	Relative uncertainty $1\,\text{fb}^{-1}$ (%)
f_L	0.499	0.010	2.0	3.8
$f_\perp$	0.235	0.009	3.8	7.2
$f_\text{S}(K\pi)$	0.170	0.007	4.1	9.1
$f_\text{S}(KK)$	0.100	0.006	6.0	10.7
$\delta_\perp$	2.60	0.033	1.3	2.4
$\delta_\parallel$	2.50	0.033	1.3	2.7
$\delta_\text{S}(K\pi)$	2.00	0.030	1.5	2.8
$\delta_\text{S}(KK)$	2.00	0.041	2.1	2.9
$\mathcal{A}_0^{CP}$	0	0.020	-	-
$\mathcal{A}_\perp^{CP}$	0	0.038	-	-
$\mathcal{A}_\text{S}(K\pi)^{CP}$	0	0.040	-	-
$\mathcal{A}_\text{S}(KK)^{CP}$	0	0.060	-	-
$\delta_\perp^{CP}$	0	0.033	-	-
$\delta_\parallel^{CP}$	0	0.033	-	-
$\delta_\text{S}(K\pi)^{CP}$	0	0.030	-	-
$\delta_\text{S}(KK)^{CP}$	0	0.041	-	-

Table 6.6: Values used to generate a series of pseudo-experiments. Also shown are the average absolute and relative statistical uncertainties. The final column labelled '$1\,\text{fb}^{-1}$' shows the relative statistical uncertainty obtained in a fit to $1\,\text{fb}^{-1}$ of data (see Table 5.3).

For each pseudo-experiment 5300 events are generated using the values given in Table 6.6, half are generated as $B^0 \to \phi K^{*0}$ and half as $\overline{B}^0 \to \phi \overline{K}^{*0}$. The detector acceptance is included using the method described in Sec. 4.5, however to simplify the study all of the events are generated with the TOS acceptance shape. A fit is made to these events using the model described in Eqn. 3.16. This is repeated 100 times and the average of the statistical uncertainty is shown in Table 6.6 in the column titled 'Absolute uncertainty $3\,\text{fb}^{-1}$'.

As the generation values of the parameters are different from those measured in data, the relative uncertainties are also shown. This is defined as the absolute uncertainty divided by the central value *e.g.* $\sigma_{f\text{L}}/f_\text{L}$. For comparison, the relative uncertainty from the $1\,\text{fb}^{-1}$ result (Sec. 5.3) is shown in the column labelled 'Relative uncertainty $1\,\text{fb}^{-1}$'.

Scaling the uncertainty from the $1\,\text{fb}^{-1}$ results by the ratio of yields, the

statistical uncertainty is expected to reduce by approximately a factor 1.8; this is confirmed via the pseudo-experiments. The relative uncertainty for the *CP*-violating parameters is not defined because the generated value is zero. However, it can be seen that the precision on these parameters is also approximately twice as small.

These predictions do not take into consideration any improvements to a future analysis and do not include systematic uncertainties. These will be discussed in the next section.

6.2.3 Expected improvements

The results presented in Sec. 5.7 have roughly equal statistical and systematic uncertainties. Therefore, any future analysis must improve on the systematic uncertainties if more data are added.

The dominating systematic uncertainty is caused by the precision of the acceptance correction. This scales with the size of the simulation sample which was roughly 45,000 for the $1\,\text{fb}^{-1}$ analysis. A larger simulation sample has been generated with 2012 conditions *i.e.* centre-of-mass energy $\sqrt{s} = 8\,\text{TeV}$. With the selection applied (see Sec. 4.2) there are approximately 345,000 candidates. This is seven times larger than the previous simulation sample and will drastically improve the precision on the acceptance correction, reducing the systematic uncertainty. The larger sample will also improve the understanding of the difference in kinematics between data and simulation.

The approximate increase in precision presented in Sec. 6.2.2 is based on an identical selection to that used for the 2011 data. As the kinematic distributions are slightly different for each sample due to the difference in centre-of-mass energy, optimising the GL separately for each period could increase the signal efficiency.

Additionally, LHCb has improved its particle identification algorithm through the use of multivariate techniques. Using these new variables could also provide moderate gains (5-10%) in selection efficiency.

Extending the $K^+\pi^-$ mass region above $1\,\text{GeV}/c^2$ would allow LHCb to study the higher order K^{*0} resonances while drastically increasing the number of signal and background events recorded. An efficient selection will need to be produced to make this possible.

6.3 Conclusion

The most precise angular analysis of the decay $B^0 \to \phi K^{*0}$ has been performed using $1\,\text{fb}^{-1}$ of integrated luminosity collected by the LHCb experiment. The results show roughly equal components with transverse and longitudinal polarisations. This is consistent with, but more precise than, previous measurements presented by the BaBar and Belle collaborations [83,86]. The results also show the presence of large S-wave components in both the K^+K^- and $K^+\pi^-$ systems. *CP* violation is searched for in the polarisation amplitudes and phases by comparing the amplitudes when fitting to B^0 and $\overline{B}^0$ samples separately, however no evidence is found.

The polarisation amplitudes and phases are also used to determine the triple product asymmetries. The measured true asymmetries show no evidence for *CP* violation while three of the fake triple product asymmetries are consistent with the presence of final-state interactions.

The difference in direct *CP* asymmetries between $B^0 \to \phi K^{*0}$ and $B^0 \to J/\psi\, K^{*0}$ is also measured and found to be consistent with zero. A future analysis by LHCb has the potential to significantly improve upon these results.

The results support the Standard Model expectation of zero *CP* violation while the precision on the polarisation amplitudes far exceeds that of theoretical predictions. Thus, to further probe the Standard Model and search for new physics, future searches should focus on improving the measurements of the *CP*-violating parameters and triple product asymmetries.

Appendix A

Study of the experimental resolution on m_{KK}

A.1 Average resolution

Due to detector resolution effects on momentum and energy measurements the reconstructed mass of the ϕ and K^{*0} mesons is expected to be smeared by a Gaussian with width of the experimental resolution. Simulated events are used to evaluate the resolution.

The m_{KK} distribution from simulation is used to fit a Breit-Wigner function convolved with a Gaussian distribution. The width of the Breit-Wigner is fixed to the World average width of the ϕ meson ($4.26\,\mathrm{MeV}/c^2$) [10] and the width of the Gaussian distribution is left free. The fitted width of the Gaussian distribution is then the experimental resolution on m_{KK}, which is measured to be $1.18 \pm 0.03\,\mathrm{MeV}/c^2$. Figure A.1 shows the a fit to m_{KK} using this model.

Due to the large width of the K^{*0} meson ($\sim 45\,\mathrm{MeV}/c^2$) compared to the experimental resolution, the resolution effect on the measured $m_{K\pi}$ distribution is ignored.

A.2 Effect of mass-dependent resolution

Section A.1 shows that the detector acceptance needs to be taken into account to have a proper description of the reconstructed ϕ line shape. However, the resolution measured in Section A.1 is actually an average resolution over the fit

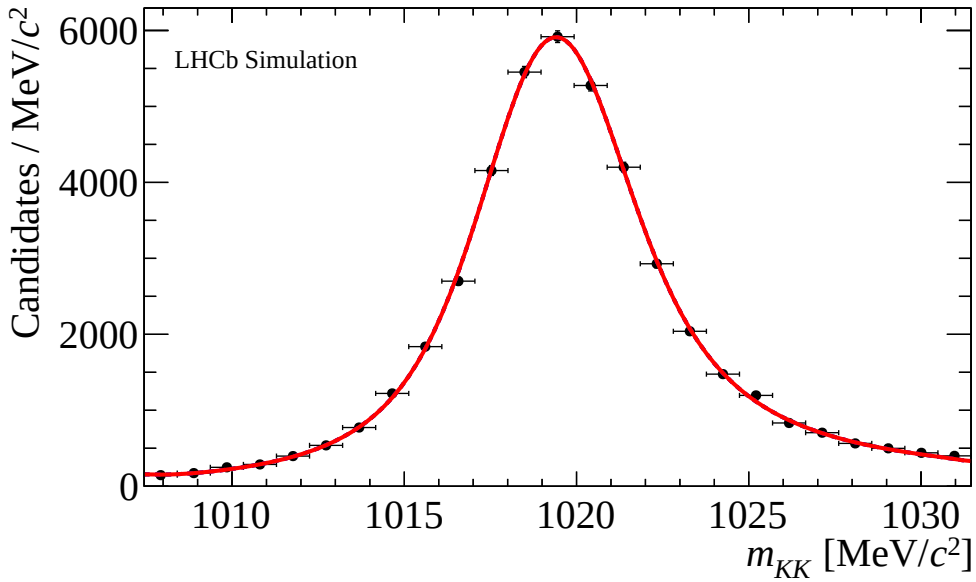

Figure A.1: m_{KK} distribution from simulated data. A fit to a Breit-Wigner function convolved with a Gaussian distribution is overlayed.

range. The absolute value of the resolution is proportional to the momentum of the daughter particles therefore the momentum resolution changes over the K^+K^- mass range. This is demonstrated in Figure A.2 using simulated events. A toy study is performed to test the effect this has on the fit results.

One hundred toys of 500,000 events each are studied, where the events are generated with a mass-dependent resolution taken from a fit to the data points in Figure A.2. The same events are then fit using a common resolution for all events corresponding to the measured value in the simulation (1.18 MeV/c^2). The distribution of all fit results are plotted and fit using a Gaussian distribution. The difference between the mean of the Gaussian and the generated value is shown in Table A.1. This is much smaller than the statistical uncertainty, it is therefore safe to ignore the mass-dependent resolution in the fit and no systematic uncertainty is necessary.

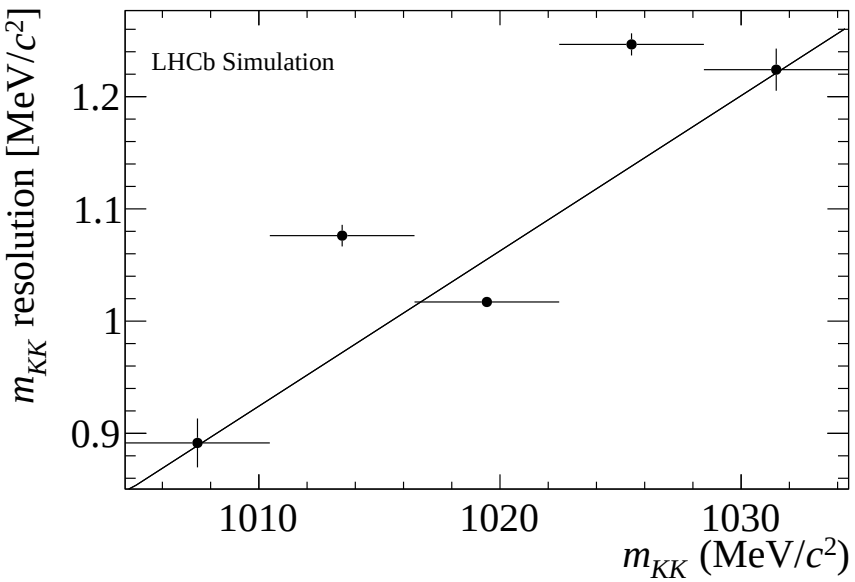

Figure A.2: Resolution on m_{KK}, calculated in bins using simulation. A fit to a first order polynomial is overlayed. The coefficients of the polynomial are calculated to be $a = -12.2 \pm 0.8$ and $b = 0.0130 \pm 0.0008$.

Parameter	Difference
f_L	0.001
$f_\perp$	0.0
$f_{\rm S}(K\pi)$	0.001
$f_{\rm S}(KK)$	0.0
$\delta_\parallel$	0.001
$\delta_\perp$	0.0
$\delta_{\rm S}(K\pi)$	0.001
$\delta_{\rm S}(KK)$	0.001

Table A.1: Difference between generated and fitted values for the study of the mass-dependent resolution.

Appendix B

Fit validation with simulated data

B.1 Fitting simulated data

Fits to simulation are shown as a cross check to see if the generation values are retrieved. The $B^0 \to \phi K^{*0}$ simulation is generated with helicity amplitudes

$$\begin{aligned} H_+ &= 0.69 \,, \\ H_0 &= 0.72 \,, \\ H_- &= 0.03 \,, \end{aligned} \tag{B.1}$$

and phases

$$\begin{aligned} \delta_+ &= 1.39 \,, \\ \delta_0 &= 0.0 \,, \\ \delta_- &= -0.74 \,. \end{aligned} \tag{B.2}$$

Using Eqn. 3.2 these are converted to the following transversity amplitudes

$$\begin{aligned} f_{\rm L} &= 0.521 \,, \\ f_\perp &= 0.251 \,, \\ \delta_\perp &= 1.426 \,, \\ \delta_\parallel &= 1.352 \,. \end{aligned} \tag{B.3}$$

Fitting to simulated events which have no angular acceptance effects or selection cuts applied yields the results in Table B.1 and fitting to fully simulated and selected events yields the results in Table B.2. The yields are also included though these are not calculated from the fit. The fit to simulation includes the detector acceptance as discussed in Sec. 4.5. The simulation was generated with no S-wave amplitudes or *CP*-violation so these are fixed to zero in the fit. Results from generator level and fully reconstructed simulation are in good agreement.

Parameter	Value
f_{L}	0.523 ± 0.002
$f_{\perp}$	0.248 ± 0.002
$\delta_{\perp}$	1.420 ± 0.008
$\delta_{\parallel}$	1.334 ± 0.007
Event yield	91856

Table B.1: Results of a fit to simulated events which have no selection applied or detector acceptance effects included. The uncertainty is statistical only.

Parameter	Value
f_{L}	0.527 ± 0.003
$f_{\perp}$	0.244 ± 0.002
$\delta_{\perp}$	1.426 ± 0.011
$\delta_{\parallel}$	1.355 ± 0.010
Event yield	45550

Table B.2: Results of a fit to fully simulated events with detector acceptance correction included. The uncertainty is statistical only.

B.2 Acceptance correction validation

In this section the simulated data are fit separately in the following subsamples: TOS, not-TOS, magnet up and magnet down. Magnet up/down refers to the polarity of the LHCb magnet in the simulation. The TOS/not-TOS fit results are compared in Table B.4 and the results from each magnet polarity are compared in Table B.5. Good agreement is seen between the results.

Parameter	Value
f_{L}	0.527 ± 0.003
$f_{\perp}$	0.244 ± 0.002
$\delta_{\perp}$	1.426 ± 0.011
$\delta_{\parallel}$	1.355 ± 0.010
$\mathcal{A}_0^{CP}$	-0.005 ± 0.005
$\mathcal{A}_{\perp}^{CP}$	0.010 ± 0.010
$\delta_{\perp}^{CP}$	0.007 ± 0.011
$\delta_{\parallel}^{CP}$	0.004 ± 0.010
Event yield	45550

Table B.3: Results of a fit to simulated events with acceptance correction included, allowing non-zero *CP* violation. The uncertainty is statistical only.

Parameter	TOS	not-TOS
f_{L}	0.531 ± 0.003	0.521 ± 0.005
$f_{\perp}$	0.249 ± 0.003	0.235 ± 0.004
$\delta_{\parallel}$	1.357 ± 0.013	1.352 ± 0.016
$\delta_{\perp}$	1.436 ± 0.014	1.411 ± 0.018
$\mathcal{A}_0^{CP}$	-0.007 ± 0.006	-0.002 ± 0.009
$\mathcal{A}_{\perp}^{CP}$	0.014 ± 0.012	0.003 ± 0.017
$\delta_{\perp}^{CP}$	0.004 ± 0.014	0.011 ± 0.018
$\delta_{\parallel}^{CP}$	0.006 ± 0.013	0.002 ± 0.016

Table B.4: Result of separate fits to TOS and not-TOS trigger samples using simulated data. The uncertainty is statistical only.

Parameter	Magnet up	Magnet down
f_{L}	0.527 ± 0.004	0.527 ± 0.004
$f_{\perp}$	0.244 ± 0.003	0.243 ± 0.003
$\delta_{\parallel}$	1.348 ± 0.014	1.363 ± 0.014
$\delta_{\perp}$	1.426 ± 0.016	1.427 ± 0.016
$\mathcal{A}_0^{CP}$	-0.001 ± 0.007	-0.010 ± 0.007
$\mathcal{A}_{\perp}^{CP}$	0.000 ± 0.014	0.020 ± 0.014
$\delta_{\perp}^{CP}$	0.005 ± 0.016	0.009 ± 0.016
$\delta_{\parallel}^{CP}$	0.006 ± 0.014	0.003 ± 0.014

Table B.5: Result of separate fits to magnet up and down samples using simulated data. The uncertainty is statistical only.

Appendix C

Comparison of kinematic variables

C.1 Comparison between data and simulation

To check the agreement between data and simulation, the *sPlot* technique is used to create background subtracted distributions of the kinematic variables. The simulation has been weighted to have the same ratio of TOS to not-TOS candidates as the signal data, this ensures differences in the distributions are not due to the large difference in the ratio of TOS to not-TOS events between data and simulation. Despite this, differences are observed between the two sets of distributions. This is treated as a source of systematic uncertainty (see Sec. 5.3.1). It can be seen that after reweighting of the final-state particle momenta the difference between data and simulation reduces, particularly in the low momentum region. This agreement is not perfect due to the coarse binning used during the reweighting.

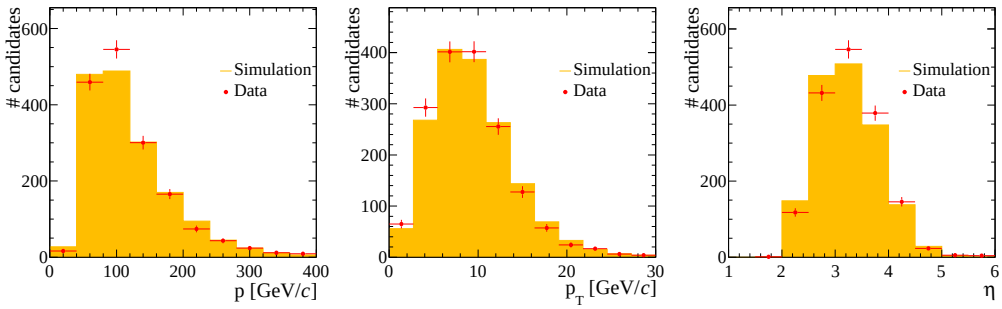

Figure C.1: Comparison of the B^0 momentum (left), transverse momentum (center) and pseudorapidity (right) between data (red points) and simulation (solid yellow). The simulation histogram is normalised to the number of candidates seen in data.

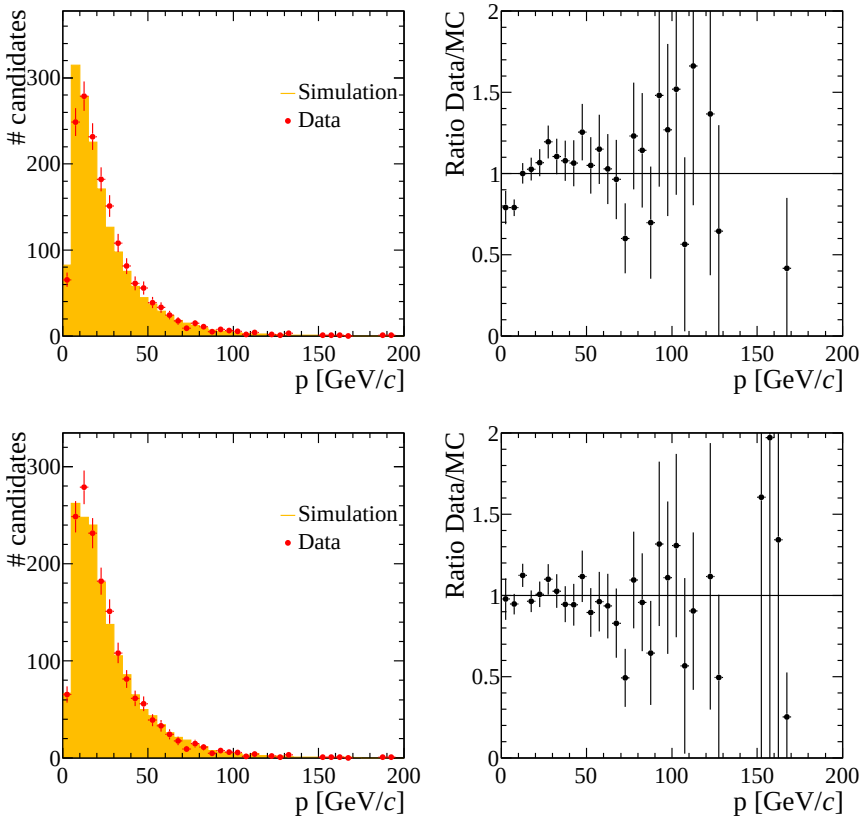

Figure C.2: Comparison of the pion momentum distribution between data (red points) and simulation (solid yellow) before (above) and after (below) the reweighting procedure described in Sec. 5.3.1 is applied. The simulation is normalised to the number of candidates seen in data.

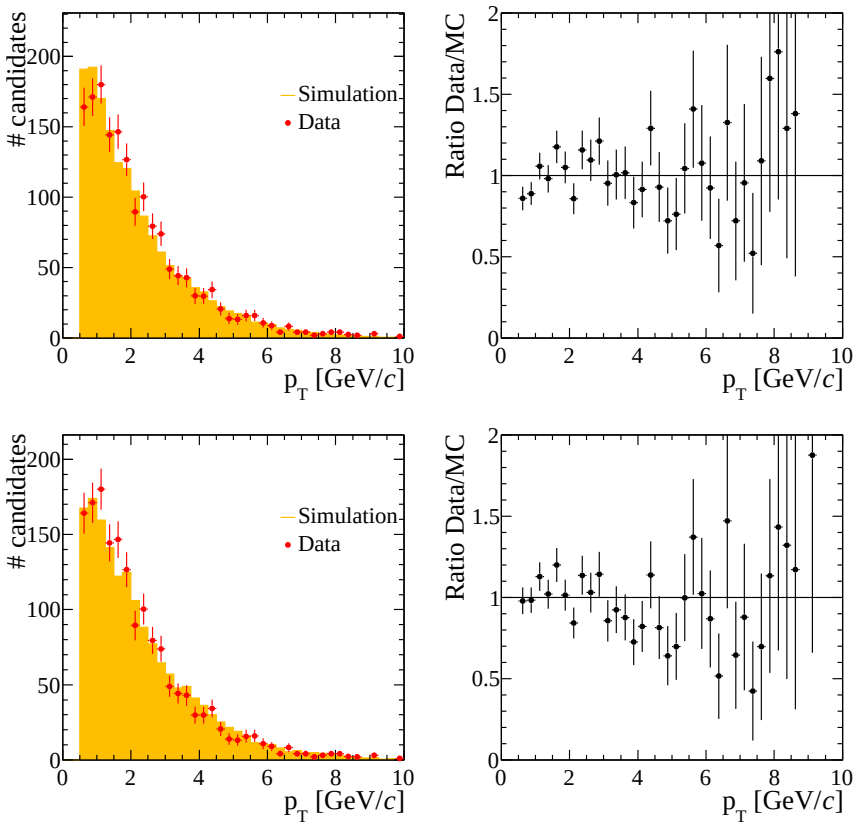

Figure C.3: Comparison of the pion transverse momentum distribution between data (red points) and simulation (solid yellow) before (above) and after (below) the reweighting procedure described in Sec. 5.3.1 is applied. The simulation is normalised to the number of candidates seen in data.

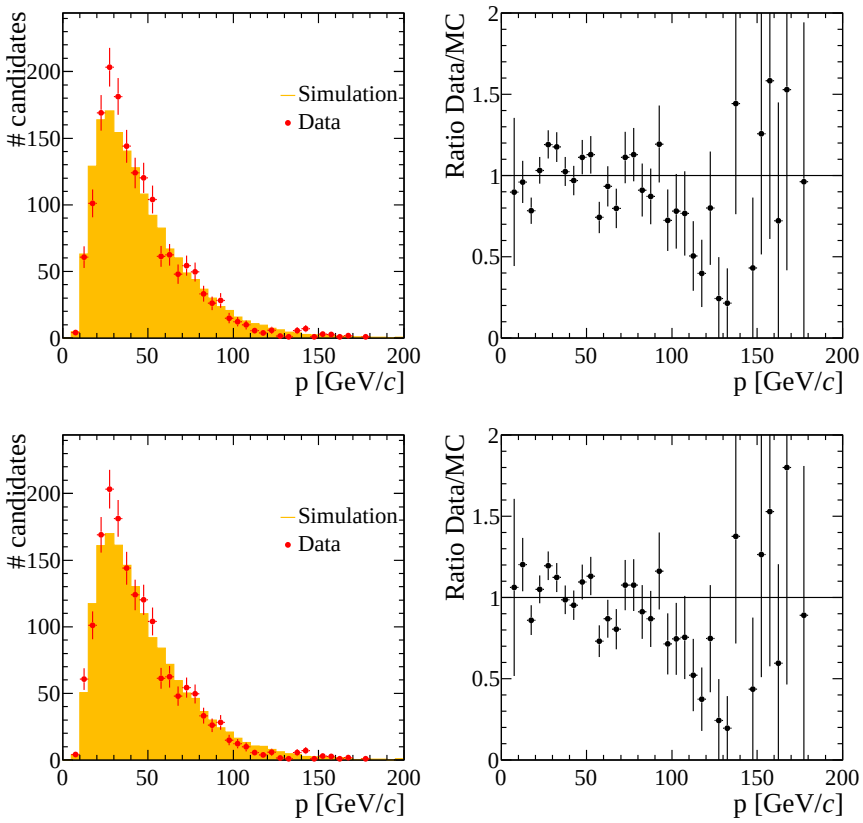

Figure C.4: Comparison of the maximum kaon momentum between data (red points) and simulation (solid yellow) before (above) and after (below) the reweighting procedure described in Sec. 5.3.1 is applied. The simulation is normalised to the number of candidates seen in data.

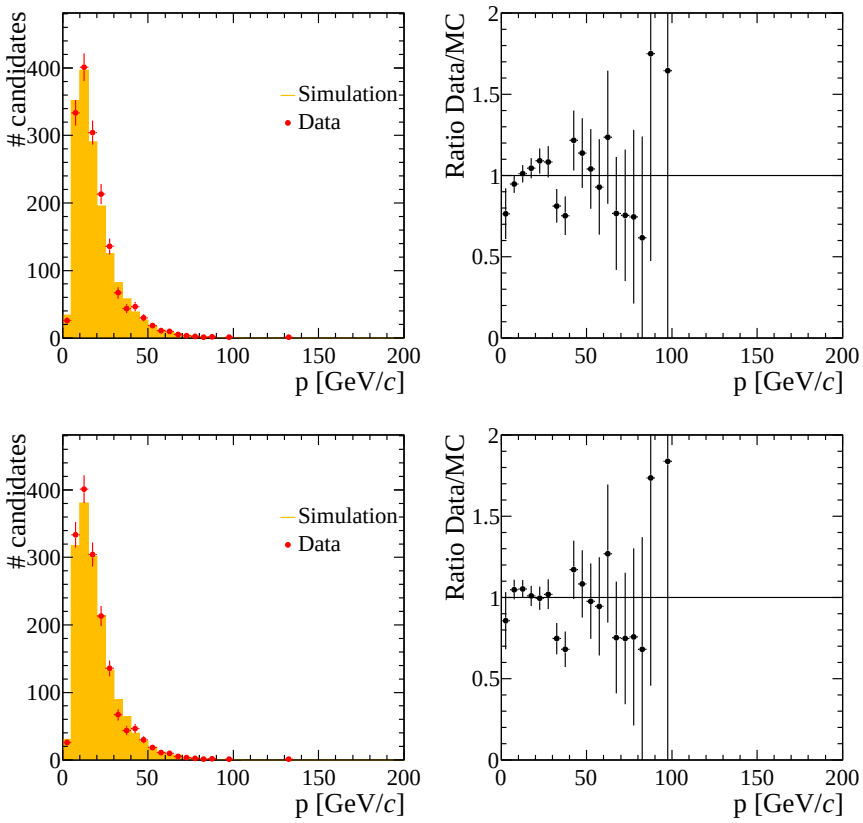

Figure C.5: Comparison of the minimum kaon momentum between data (red points) and simulation (solid yellow) before (above) and after (below) the reweighting procedure described in Sec. 5.3.1 is applied. The simulation is normalised to the number of candidates seen in data.

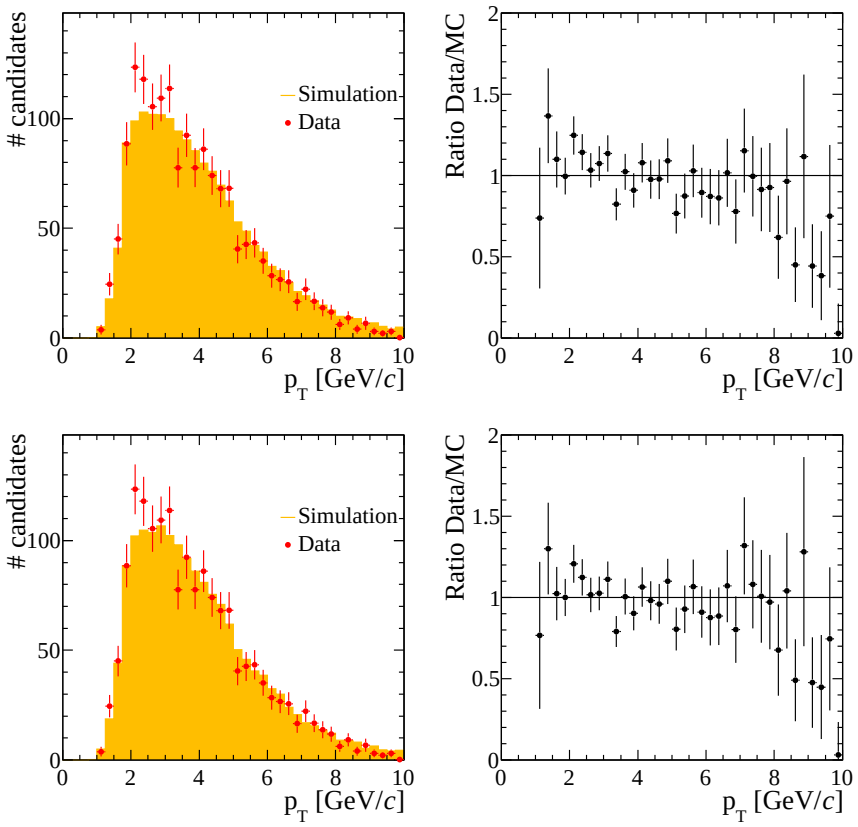

Figure C.6: Comparison of the maximum kaon transverse momentum between data (red points) and simulation (solid yellow) before (above) and after (below) the reweighting procedure described in Sec. 5.3.1 is applied. The simulation is normalised to the number of candidates seen in data.

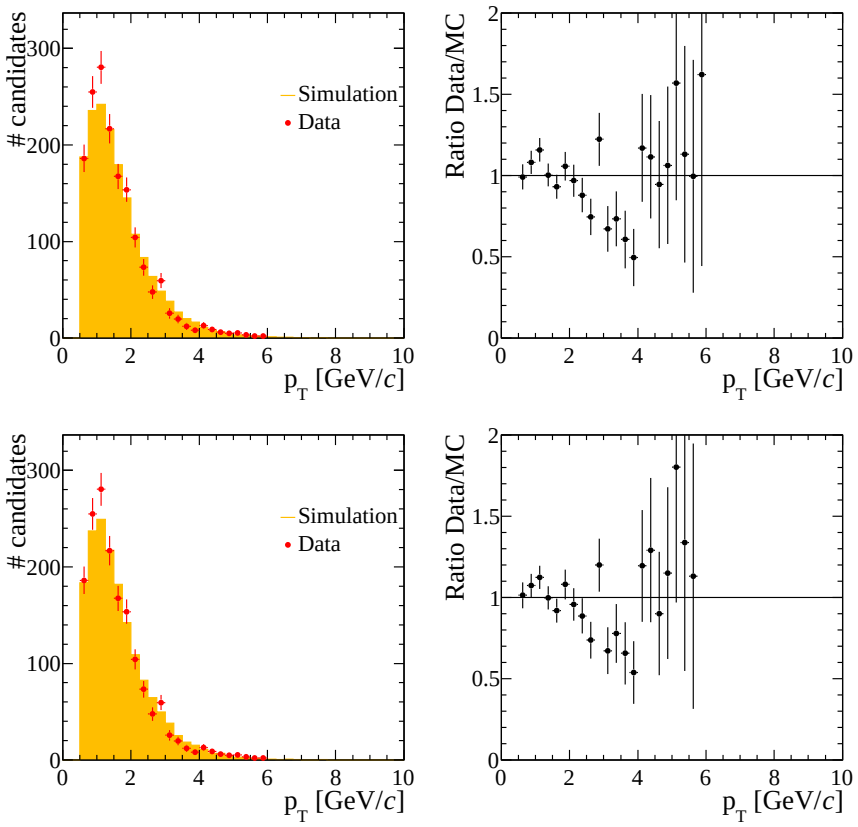

Figure C.7: Comparison of the minimum kaon transverse momentum between data (red points) and simulation (solid yellow) before (above) and after (below) the reweighting procedure described in Sec. 5.3.1 is applied. The simulation is normalised to the number of candidates seen in data.

C.2 Comparison between signal and control channel

The agreement between kinematic variables for the signal channel $B^0 \to \phi K^{*0}$ and control channel $B^0 \to J/\psi K^{*0}$ is studied in this section where the data have been separated into TOS and not-TOS samples. Figure 5.12 shows the combined distribution. Good agreement is observed for the not-TOS kaon and pion distributions while both the B^0 and TOS kaon and pion distributions show small differences. It is assumed these differences are covered by the systematic uncertainty assigned in Sec. 5.5.3.

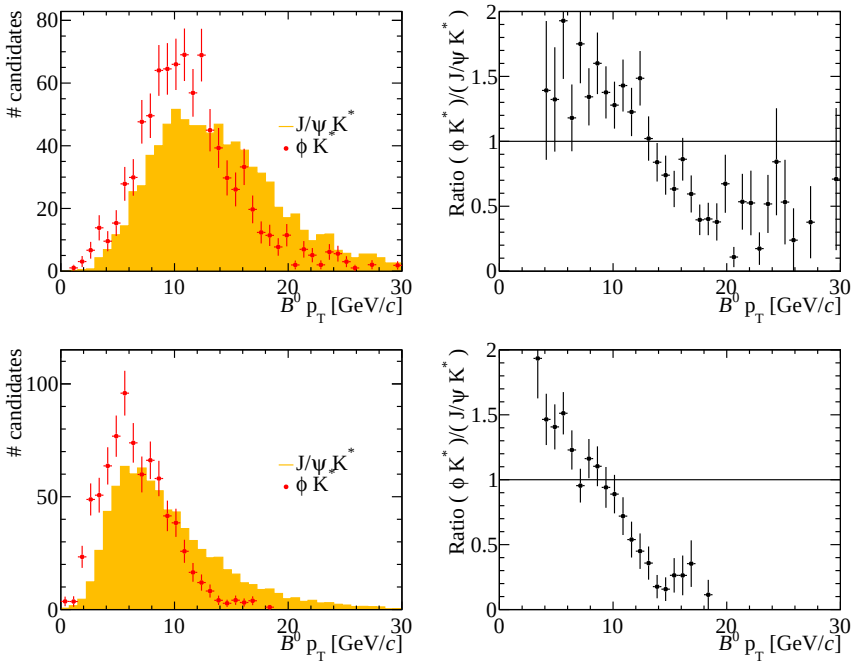

Figure C.8: Comparison of the B^0 momentum between $B^0 \to \phi K^{*0}$ (red points) and $B^0 \to J/\psi K^{*0}$ (solid yellow) for TOS (above) and not-TOS (below). The control channel is normalised to the number of candidates seen in signal data.

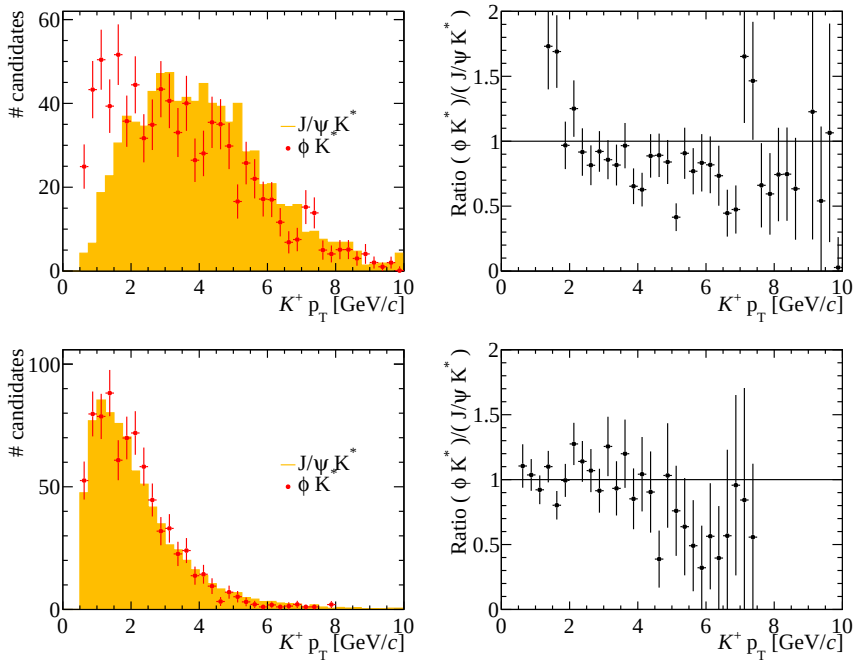

Figure C.9: Comparison of the kaon (from K^{*0}) momentum between $B^0 \to \phi K^{*0}$ (red points) and $B^0 \to J/\psi K^{*0}$ (solid yellow) for TOS (above) and not-TOS (below). The control channel is normalised to the number of candidates seen in signal data.

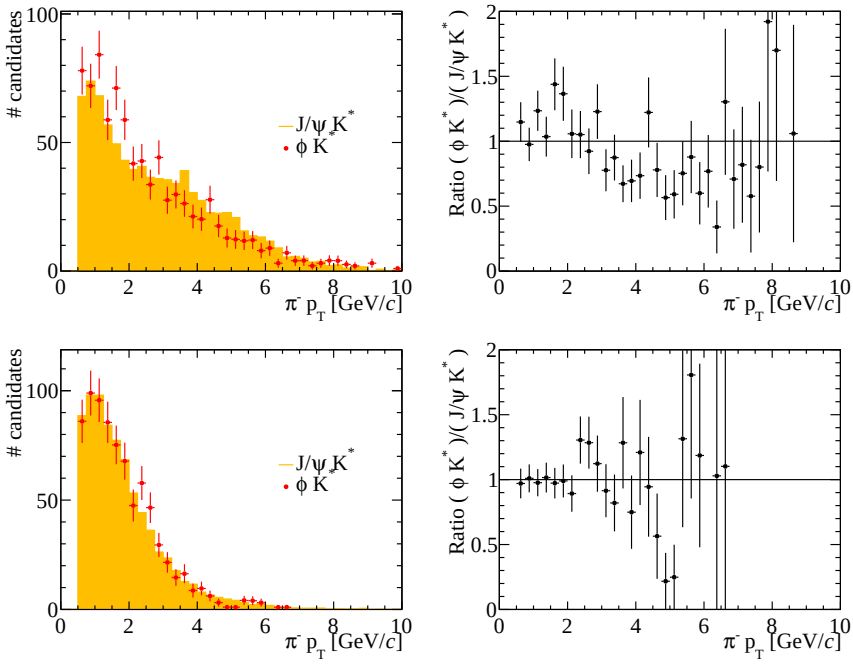

Figure C.10: Comparison of the pion (from K^{*0}) momentum between $B^0 \to \phi K^{*0}$ (red points) and $B^0 \to J/\psi K^{*0}$ (solid yellow) for TOS (above) and not-TOS (below). Th control channel is normalised to the number of candidates seen in signal data.

Bibliography

[1] WMAP, C. L. Bennett *et al.*, *Nine-year Wilkinson Microwave Anisotropy Probe (WMAP) observations: Final maps and results*, Astrophys. J. Suppl. **208** (2013) 20, arXiv:1212.5225.

[2] Planck collaboration, P. A. R. Ade *et al.*, *Planck 2013 results. XVI. Cosmological parameters*, arXiv:1303.5076.

[3] S. Weinberg, *The First Three Minutes: A Modern View of the Origin of the Universe*, Basic Books, 1993.

[4] A. D. Sakharov, *Violation of CP invariance, C asymmetry, and baryon asymmetry of the Universe*, Pisma Zh. Eksp. Teor. Fiz. **5** (1967) 32.

[5] P. A. M. Dirac, *The quantum theory of the electron*, Proc. Roy. Soc. Lond. **A117** (1928) 610.

[6] P. A. M. Dirac, *Quantized singularities in the electromagnetic field*, Proc. Roy. Soc. Lond. **A133** (1931) 60.

[7] C. D. Anderson, *The positive electron*, Phys. Rev. **43** (1933) 491.

[8] J. H. Christenson, J. W. Cronin, V. L. Fitch, and R. Turlay, *Evidence for the 2π decay of the K_2^0 meson*, Phys. Rev. Lett. **13** (1964) 138.

[9] A. G. Cohen, D. B. Kaplan, and A. E. Nelson, *Progress in electroweak baryogenesis*, Ann. Rev. Nucl. Part. Sci. **43** (1993) 27, arXiv:hep-ph/9302210.

[10] Particle Data Group, J. Beringer *et al.*, *Review of Particle Physics*, Phys. Rev. **D86** (2012) , and 2013 partial update for the 2014 edition.

[11] L3 collaboration, B. Adeva *et al.*, *Measurement of Z^0 decays to hadrons and a precise determination of the number of neutrino species*, Phys. Lett. **B237** (1990) 136.

[12] ALEPH collaboration, D. Decamp *et al.*, *A precise determination of the number of families with light neutrinos and of the Z^0 boson partial widths*, Phys. Lett. **B235** (1990) 399.

[13] Delphi collaboration, P. A. Aarnio *et al.*, *Measurement of the mass and width of the Z^0 particle from multi - hadronic final states produced in e^+e^- annihilations*, Phys. Lett. **B231** (1989) 539.

[14] W. N. Cottingham and D. A. Greenwood, *An Introduction to the Standard Model of Particle Physics*, Cambridge University Press, 1998.

[15] CMS collaboration, S. Chatrchyan *et al.*, *Observation of a new boson at a mass of 125 GeV with the CMS experiment at the LHC*, Phys. Lett. **B716** (2012) 30, `arXiv:1207.7235`.

[16] ATLAS collaboration, G. Aad *et al.*, *Observation of a new particle in the search for the Standard Model Higgs boson with the ATLAS detector at the LHC*, Phys. Lett. **B716** (2012) 1, `arXiv:1207.7214`.

[17] T. Aoyama, M. Hayakawa, T. Kinoshita, and M. Nio, *Tenth-order QED contribution to the electron $g-2$ and an improved value of the Fine Structure Constant*, Phys. Rev. Lett. **109** (2012) 111807, `arXiv:1205.5368`.

[18] R. Bouchendira *et al.*, *New determination of the Fine Structure Constant and test of the quantum electrodynamics*, Phys. Rev. Lett. **106** (2011) 080801, `arXiv:1012.3627`.

[19] D. Griffiths, *Introduction To Elementary Particle Physics*, John Wiley & Sons, Inc, 1987.

[20] Gargamelle Neutrino collaboration, F. J. Hasert *et al.*, *Observation of neutrino like interactions without muon or electron in the Gargamelle Neutrino experiment*, Phys. Lett. **B46** (1973) 138.

[21] UA1 collaboration, G. Arnison *et al.*, *Experimental observation of isolated large transverse energy electrons with associated missing energy at $\sqrt{s} = 540\,\text{GeV}$*, Phys. Lett. **B122** (1983) 103.

[22] UA2 collaboration, M. Banner *et al.*, *Observation of single isolated electrons of high transverse momentum in events with missing transverse energy at the CERN $\overline{p}p$ collider*, Phys. Lett. **B122** (1983) 476.

[23] D. H. Perkins, *Introduction To High Energy Physics*, Addison-Wesley Publishing Company, 1982.

[24] S. Bethke, *The 2009 World average of α_s*, Eur. Phys. J. **C64** (2009) 689, `arXiv:0908.1135`.

[25] N. Cabibbo, *Unitary symmetry and leptonic decays*, Phys. Rev. Lett. **10** (1963) 531.

[26] S. L. Glashow, J. Iliopoulos, and L. Maiani, *Weak interactions with lepton-hadron symmetry*, Phys. Rev. **D2** (1970) 1285.

[27] F. Halzen and A. D. Martin, *Quarks and Leptons: An Introductory Course in Modern Particle Physics*, Lecture Notes in Physics, John Wiley & Sons, Inc, 1984.

[28] M. Kobayashi and T. Maskawa, *CP violation in the renormalizable theory of weak interaction*, Prog. Theor. Phys. **49** (1973) 652.

[29] S. W. Herb *et al.*, *Observation of a dimuon resonance at 9.5* GeV *in 400* GeV *proton-nucleus collisions*, Phys. Rev. Lett. **39** (1977) 252.

[30] CDF collaboration, F. Abe *et al.*, *Observation of top quark production in $\bar{p}p$ collisions*, Phys. Rev. Lett. **74** (1995) 2626, arXiv:hep-ex/9503002.

[31] D0 collaboration, S. Abachi *et al.*, *Observation of the top quark*, Phys. Rev. Lett. **74** (1995) 2632, arXiv:hep-ex/9503003.

[32] E. Noether, *Invariant variation problems*, Gott. Nachr. **1918** (1918) 235, arXiv:physics/0503066.

[33] T. D. Lee and C.-N. Yang, *Question of parity conservation in weak interactions*, Phys. Rev. **104** (1956) 254.

[34] C. S. Wu *et al.*, *Experimental test of parity conservation in beta decay*, Phys. Rev. **105** (1957) 1413.

[35] M. Goldhaber, L. Grodzins, and A. W. Sunyar, *Helicity of neutrinos*, Phys. Rev. **109** (1958) 1015.

[36] L. D. Landau, *On the conservation laws for weak interactions*, Nucl. Phys. **3** (1957) 127.

[37] LHCb collaboration, R. Aaij *et al.*, *Evidence for CP violation in time-integrated $D^0 \to h^- h^+$ decay rates*, Phys. Rev. Lett. **108** (2012) 111602, arXiv:1112.0938.

[38] LHCb collaboration, R. Aaij *et al.*, *Measurements of indirect CP asymmetries in $D^0 \to K^- K^+$ and $D^0 \to \pi^- \pi^+$ decays*, Phys. Rev. Lett. **112** (2014) 041801, arXiv:1310.7201.

[39] M. Beyer, *CP Violation in Particle, Nuclear and Astrophysics*, Springer Berlin Heidelberg, 2002.

[40] LHCb collaboration, R. Aaij *et al.*, *First observation of CP violation in the decays of B_s^0 mesons*, Phys. Rev. Lett. **110** (2013) 221601, arXiv:1304.6173.

[41] LHCb collaboration, R. Aaij *et al.*, *Measurement of the flavour-specific CP-violating asymmetry a_{sl}^s in B_s^0 decays*, Phys. Lett. **B728** (2014) 607, arXiv:1308.1048.

[42] A. Lenz and U. Nierste, *Theoretical update of $B_s - \bar{B}_s$ mixing*, JHEP **0706** (2007) 072, arXiv:hep-ph/0612167.

[43] D0 collaboration, V. M. Abazov *et al.*, *Study of CP-violating charge asymmetries of single muons and like-sign dimuons in $p\overline{p}$ collisions*, Phys. Rev. **D89** (2014) 012002, arXiv:1310.0447.

[44] I. Adachi *et al.*, *Precise measurement of the CP violation parameter* $\sin 2\phi$ *in* $B^0 \to c\bar{c}K^0$ *decays*, Phys. Rev. Lett. **108** (2012) 171802, arXiv:1201.4643.

[45] BaBar collaboration, B. Aubert *et al.*, *Measurement of time-dependent CP asymmetry in* $B^0 \to c\bar{c}K^{*0}$ *decays*, Phys. Rev. **D79** (2009) 072009, arXiv:0902.1708.

[46] BaBar collaboration, B. Aubert *et al.*, *Measurements of CP-violating asymmetries in the decay* $B^0 \to K^+K^-K^0$, Phys. Rev. Lett. **99** (2007) 161802, arXiv:0706.3885.

[47] LHCb collaboration, R. Aaij *et al.*, *Measurement of CP violation and the* B_s^0 *meson decay width difference with* $B_s^0 \to J/\psi K^+K^-$ *and* $B_s^0 \to J/\psi\pi^+\pi^-$ *decays*, Phys. Rev. **D87** (2013) 112010, arXiv:1304.2600.

[48] J. Charles *et al.*, *Predictions of selected flavour observables within the Standard Model*, Phys. Rev. **D84** (2011) 033005, arXiv:1106.4041.

[49] S. Benson, *Searching for CP Violation in the* $B_s^0 \to \phi\phi$ *Decay at LHCb*, PhD thesis, University of Edinburgh, United Kingdom, 2014, CERN-THESIS-2014-087.

[50] M. Beneke *et al.*, *Branching fractions, polarisation and asymmetries of* $B \to VV$ *decays*, Nucl. Phys. **B774** (2007) 64, arXiv:hep-ph/0612290.

[51] M. Bartsch, G. Buchalla, and C. Kraus, $B \to V_L V_L$ *decays at next-to-leading order in QCD*, arXiv:0810.0249.

[52] H.-Y. Cheng and C.-K. Chua, *QCD factorization for charmless hadronic* B_s *decays revisited*, Phys. Rev. **D80** (2009) 114026, arXiv:0910.5237.

[53] L. Evans and P. Bryant, *LHC machine*, JINST **3** (2008) S08001.

[54] C. Lefévre, *Cern-di-0812015*, 2008.

[55] http://press.web.cern.ch/press-releases/2008/09/incident-lhc-sector-3-4.

[56] ATLAS collaboration, W. W. Armstrong *et al.*, *ATLAS: Technical proposal for a general-purpose pp experiment at the Large Hadron Collider at CERN*, 1994. http://atlas.web.cern.ch/Atlas/TP/PS/tp9.ps.Z.

[57] CMS collaboration, *CMS, the Compact Muon Solenoid: Technical proposal*, 1994. http://cds.cern.ch/record/290969.

[58] ALICE collaboration, J. Schukraft *et al.*, *ALICE: Technical proposal for a large ion collider experiment at the CERN LHC*, 1995. http://cds.cern.ch/record/293391.

[59] LHCb collaboration, A. Alves *et al.*, *The LHCb detector at the LHC*, JINST **3** (2008) S08005.

[60] LHCb collaboration, S. Amato *et al.*, *LHCb technical proposal*, 1998. `http://cds.cern.ch/record/622031`.

[61] S. Amato *et al.*, *LHCb magnet: Technical design report*, Technical Design Report LHCb, CERN, Geneva, 2000. `http://cds.cern.ch/record/424338`.

[62] LHCb Outer Tracker group, R. Arink *et al.*, *Performance of the LHCb Outer Tracker*, JINST **9** (2014) 01002, `arXiv:1311.3893`.

[63] *Optimization and calibration of the same-side kaon tagging algorithm using hadronic B_s^0 decays in 2011 data*, 2012. `http://cds.cern.ch/record/1484021`.

[64] LHCb collaboration, R. Aaij *et al.*, *Opposite-side flavour tagging of B mesons at the LHCb experiment*, Eur. Phys. J. **C72** (2012) 2022, `arXiv:1202.4979`.

[65] A.-N. et al, *LHCb reoptimized detector design and performance: Technical Design Report*, Technical Design Report LHCb, CERN, Geneva, 2003. `http://lhcb.web.cern.ch/lhcb/TDR/TDR9.pdf`.

[66] M. Adinolfi *et al.*, *Performance of the LHCb RICH detector at the LHC*, Eur. Phys. J. **C73** (2013) 2431, `arXiv:1211.6759`.

[67] LHCb collaboration, R. Aaij *et al.*, *Measurement of b-hadron branching fractions for two-body decays into charmless charged hadrons*, JHEP **1210** (2012) 037, `arXiv:1206.2794`.

[68] LHCb collaboration, *LHCb calorimeters: Technical design report*, 2000. `http://cds.cern.ch/record/494264`.

[69] F. Archilli *et al.*, *Performance of the muon identification at LHCb*, JINST **8** (2013) P10020, `arXiv:1306.0249`.

[70] R. Aaij *et al.*, *The LHCb trigger and its performance in 2011*, JINST **8** (2013) P04022, `arXiv:1211.3055`.

[71] G. Barrand *et al.*, *GAUDI - A software architecture and framework for building HEP data processing applications*, Comput. Phys. Commun. **140** (2001) 45.

[72] M. Clemencic *et al.*, *Recent developments in the LHCb software framework Gaudi*, J. Phys. Conf. Ser. **219** (2010) 042006.

[73] G. Corti *et al.*, *Software for the LHCb experiment*, IEEE Trans. Nucl. Sci. **53** (2006) 1323.

[74] T. Sjostrand, S. Mrenna, and P. Z. Skands, *PYTHIA 6.4 physics and manual*, JHEP **0605** (2006) 026, `arXiv:hep-ph/0603175`.

[75] I. Belyaev *et al.*, *Handling of the generation of primary events in* Gauss*, the LHCb simulation framework*, Nuclear Science Symposium Conference Record (NSS/MIC) **IEEE** (2010) 1155.

[76] D. J. Lange, *The EvtGen particle decay simulation package*, Nucl. Instrum. Meth. **A462** (2001) 152.

[77] P. Golonka and Z. Was, *PHOTOS Monte Carlo: a precision tool for QED corrections in Z and W decays*, Eur. Phys. J. **C45** (2006) 97, arXiv:hep-ph/0506026.

[78] Geant4 collaboration, J. Allison *et al.*, *Geant4 developments and applications*, IEEE Trans. Nucl. Sci. **53** (2006) 270; Geant4 collaboration, S. Agostinelli *et al.*, *Geant4: a simulation toolkit*, Nucl. Instrum. Meth. **A506** (2003) 250.

[79] M. Clemencic *et al.*, *The LHCb simulation application,* Gauss*: design, evolution and experience*, J. Phys. Conf. Ser. **331** (2011) 032023.

[80] M. Ciuchini *et al.*, *CP violating B decays in the standard model and supersymmetry*, Phys. Rev. Lett. **79** (1997) 978, arXiv:hep-ph/9704274.

[81] BaBar collaboration, B. Aubert *et al.*, *Measurement of the $B^0 \to \phi K_0^*$ decay amplitudes*, Phys. Rev. Lett. **93** (2004) 231804, arXiv:hep-ex/0408017.

[82] BaBar collaboration, B. Aubert *et al.*, *Vector-tensor and vector-vector decay amplitude analysis of $B^0 \to \phi K_0^*$*, Phys. Rev. Lett. **98** (2007) 051801, arXiv:hep-ex/0610073.

[83] BaBar collaboration, B. Aubert *et al.*, *Time-dependent and time-integrated angular analysis of $B \to \phi K_s^0 \pi^0$ and $B \to \phi K^+ \pi^-$*, Phys. Rev. **D78** (2008) 092008, arXiv:0808.3586.

[84] Belle collaboration, , *Measurement of Branching Fractions and Polarization in $B \to \phi K^*$ Decays*, Phys. Rev. Lett. **91** (2003) 201801, arXiv:hep-ex/0307014.

[85] Belle collaboration, , *Measurement of polarization and triple-product correlations in $B \to \phi K^*$ Decays*, Phys. Rev. Lett. **94** (2005) 221804, arXiv:hep-ex/0503013.

[86] Belle collaboration, M. Prim *et al.*, *Angular analysis of $B^0 \to \phi K^*$ decays and search for CP violation at Belle*, Phys. Rev. **D88** (2013) 072004, arXiv:1308.1830.

[87] J. Korner and G. R. Goldstein, *Quark and particle helicities in hadronic charmed particle decays*, Phys. Lett. **B89** (1979) 105.

[88] BaBar collaboration, B. Aubert *et al.*, *A study of $B^0 \to \rho^+ \rho^-$ decays and constraints on the CKM angle alpha*, Phys. Rev. **D76** (2007) 052007, arXiv:0705.2157.

[89] CLEO collaboration, S. E. Csorna *et al.*, *Measurements of the branching fractions and helicity amplitudes in $B \to D^* \rho$ decays*, Phys. Rev. **D67** (2003) 112002, arXiv:hep-ex/0301028.

[90] BaBar collaboration, J. Lees *et al.*, *B^0 meson decays to $\rho^0 K^{*0}$, $f_0 K^{*0}$, and $\rho^- K^{*+}$, including higher K^* resonances*, Phys. Rev. **D85** (2012) 072005, arXiv:1112.3896.

[91] BaBar collaboration, B. Aubert *et al.*, *Measurements of branching fractions, polarizations, and direct CP-violation asymmetries in $B \to \rho K^*$ and $B \to f_0(980) K^*$ decays*, Phys. Rev. Lett. **97** (2006) 201801, arXiv:hep-ex/0607057.

[92] A. Datta, M. Duraisamy, and D. London, *Searching for new physics with B-decay fake triple products*, Phys. Lett. **B701** (2011) 357, arXiv:1103.2442.

[93] Y.-D. Yang, R.-M. Wang, and G.-R. Lu, *Polarizations in decays $B_{(u,d)} \to VV$ and possible implications for R-parity violating SUSY*, Phys. Rev. **D72** (2005) 015009, arXiv:hep-ph/0411211.

[94] P. K. Das and K.-C. Yang, *Data for polarization in charmless $B \to \phi K^*$: A signal for new physics?*, Phys. Rev. **D71** (2005) 094002, arXiv:hep-ph/0412313.

[95] H.-Y. Cheng and K.-C. Yang, *Branching ratios and polarization in $B \to VV, VA, AA$ decays*, Phys. Rev. **D78** (2008) 094001, arXiv:0805.0329.

[96] P. Colangelo, F. De Fazio, and T. N. Pham, *The riddle of polarization in $B \to VV$ transitions*, Phys. Lett. **B597** (2004) 291, arXiv:hep-ph/0406162.

[97] M. Ladisa, V. Laporta, G. Nardulli, and P. Santorelli, *Final state interactions for $B \to VV$ charmless decays*, Phys. Rev. **D70** (2004) 114025, arXiv:hep-ph/0409286.

[98] H.-Y. Cheng, C.-K. Chua, and A. Soni, *Final state interactions in hadronic B decays*, Phys. Rev. **D71** (2005) 014030, arXiv:hep-ph/0409317.

[99] A. L. Kagan, *Polarization in $B \to VV$ decays*, Phys. Lett. **B601** (2004) 151, arXiv:hep-ph/0405134.

[100] G. Valencia, *Angular correlations in the decay $B \to VV$ and CP violation*, Phys. Rev. **D39** (1989) 3339.

[101] A. S. Dighe, I. Dunietz, H. J. Lipkin, and J. L. Rosner, *Angular distributions and lifetime differences in $B_s \to J/\psi\phi$ decays*, Phys. Lett. **B369** (1996) 144, arXiv:hep-ph/9511363.

[102] C.-W. Chiang and L. Wolfenstein, *Observables in the decays of B to two vector mesons*, Phys. Rev. **D61** (2000) 074031, arXiv:hep-ph/9911338.

[103] Kramer, G. and Palmer, W. F., *Branching ratios and CP asymmetries in the decay $B \to VV$*, Phys. Rev. **D45** (1992) 193.

[104] N. Sinha and R. Sinha, *Determination of the angle gamma using $B \to D^* V$ modes*, Phys. Rev. Lett. **80** (1998) 3706, arXiv:hep-ph/9712502.

[105] F. Von Hippel and C. Quigg, *Centrifugal-barrier effects in resonance partial decay widths, shapes, and production amplitudes*, Phys. Rev. **D5** (1972) 624.

[106] D. Aston *et al.*, *A study of $K^-\pi^+$ scattering in the reaction $K^-p \to K^-\pi^+n$ at 11* GeV/c, Nucl. Phys. **B296** (1988) 493.

[107] LHCb collaboration, Aaij, R. et al, *Analysis of the resonant components in $\overline{B}{}^0_s \to J/\psi\pi^+\pi^-$*, Phys. Rev. **D86** (2012) 052006, arXiv:1204.5643.

[108] S. M. Flatté, *On the nature of 0^+ mesons*, Phys. Lett. **B63** (1976) 228.

[109] B. Kayser, *Kinematically nontrivial CP violation in beauty decays*, Nucl. Phys. Proc. Suppl. **13** (1990) 487.

[110] A. Datta and D. London, *Triple-product correlations in $B \to V1V2$ decays and new physics*, Int. J. Mod. Phys. **A19** (2004) 2505, arXiv:hep-ph/0303159.

[111] M. Gronau and J. L. Rosner, *Triple product asymmetries in K, $D_{(}s)$ and $B_{(}s)$ decays*, Phys. Rev. **D84** (2011) 096013, arXiv:1107.1232.

[112] W. Bensalem and D. London, *T-violating triple product correlations in hadronic b decays*, Phys. Rev. **D64** (2001) 116003, arXiv:hep-ph/0005018.

[113] KTeV collaboration, E. Abouzaid *et al.*, *A measurement of the K^0 charge radius and a CP violating asymmetry together with a search for CP violating E1 direct photon emission in the rare decay $K_L \to \pi^+\pi^-e^+e^-$*, Phys. Rev. Lett. **96** (2006) 101801, arXiv:hep-ex/0508010.

[114] KTeV collaboration, A. Alavi-Harati *et al.*, *Observation of CP violation in $K_L \to \pi^+\pi^-e^+e^-$ decays*, Phys. Rev. Lett. **84** (2000) 408, arXiv:hep-ex/9908020.

[115] NA48 collaboration, A. Lai *et al.*, *Investigation of $K_{L,S} \to \pi^+\pi^-e^+e^-$ decays*, Eur. Phys. J. **C30** (2003) 33, http://cds.cern.ch/record/619617.

[116] P. Heiliger and L. Sehgal, *Direct and indirect CP violation in the decay $K_L \to \pi^+\pi^-e^+e^-$*, Phys. Rev. **D48** (1993) 4146.

[117] J. K. Elwood, M. B. Wise, and M. J. Savage, $K_L \to \pi^+\pi^-e^+e^-$, Phys. Rev. **D52** (1995) 5095, arXiv:hep-ph/9504288.

[118] J. K. Elwood, M. B. Wise, M. J. Savage, and J. W. Walden, *Final state interactions and CP violation in $K_L \to \pi^+\pi^-e^+e^-$*, Phys. Rev. **D53** (1996) 4078, arXiv:hep-ph/9506287.

[119] CLEO collaboration, R. A. Briere *et al.*, *Observation of $B \to \phi K$ and $B \to \phi K^*$*, Phys. Rev. Lett. **86** (2001) 3718, arXiv:hep-ex/0101032.

[120] LHCb collaboration, R. Aaij *et al.*, *Measurement of polarization amplitudes and CP asymmetries in $B^0 \to \phi K^*(892)^0$*, arXiv:1403.2888.

[121] V. V. Gligorov and M. Williams, *Efficient, reliable and fast high-level triggering using a bonsai boosted decision tree*, JINST **8** (2013) P02013, arXiv:1210.6861.

[122] M. Adinolfi *et al.*, *Performance of the LHCb RICH detector at the LHC*, Eur. Phys. J. **C73** (2013) 2431, arXiv:1211.6759.

[123] LHCb collaboration, R. Aaij *et al.*, *Observation of $B_c^+ \to J/\psi D_s^+$ and $B_c^+ \to J/\psi D_s^{*+}$ decays*, Phys. Rev. **D87** (2013) 112012, arXiv:1304.4530.

[124] D. Karlen, *Using projections and correlations to approximate probability distributions*, Comput. Phys. **12** (1998) 380, arXiv:physics/9805018.

[125] LHCb collaboration, R. Aaij *et al.*, *First observation of the decay $B_s^0 \to K^{*0}\overline{K}^{*0}$*, Phys. Lett. **B709** (2012) 50, arXiv:1111.4183.

[126] LHCb collaboration, R. Aaij *et al.*, *First observation of the decay $B_s^0 \to \phi\overline{K}^{*0}$*, JHEP **11** (2013) 092, arXiv:1306.2239.

[127] D. Martínez Santos, *Study of the very rare decay $B_s^0 \to \mu^+\mu^-$ in LHCb*, PhD thesis, Universidade de Santiago de Compostela, Spain, 2010, CERN-THESIS-2010-068.

[128] I. J. Myung, *Tutorial on maximum likelihood estimation*, Journal of Mathematical Psychology **47** (2003) 90 .

[129] M. Pivk and F. R. Le Diberder, *sPlot: a statistical tool to unfold data distributions*, Nucl. Instrum. Meth. **A555** (2005) 356, arXiv:physics/0402083.

[130] LHCb collaboration, R. Aaij *et al.*, *Measurement of the B^0–$\overline{B}^0$ oscillation frequency Δm_d with the decays $B^0 \to D^-\pi^+$ and $B^0 \to J/\psi K^{*0}$*, Phys. Lett. **B719** (2013) 318, arXiv:1210.6750.

[131] W. T. Eadie *et al.*, *Statistical Methods in Experimental Physics*, North Holland, 1971.

[132] T. Skwarnicki, *A study of the radiative cascade transitions between the upsilon-prime and upsilon resonances*, PhD thesis, Institute of Nuclear Physics, Krakow, 1986, DESY-F31-86-02.

[133] LHCb collaboration, R. Aaij *et al.*, *First measurement of the CP-violating phase in $B_s^0 \to \phi\phi$ decays*, Phys. Rev. Lett. **110** (2013) 241802, arXiv:1303.7125.

[134] LHCb collaboration, R. Aaij *et al.*, *Search for CP violation in $D^+ \to K^-K^+\pi^+$ decays*, Phys. Rev. **D84** (2011) 112008, arXiv:1110.3970.

[135] ARGUS collaboration, H. Albrecht *et al.*, *Measurement of the polarization in the decay $B \to J/\psi K^*$*, Phys. Lett. **B340** (1994) 217.

[136] W. Verkerke and D. P. Kirkby, *The RooFit toolkit for data modeling*, arXiv:physics/0306116, http://roofit.sourceforge.net.

[137] F. Azfar *et al.*, *Formulae for the Analysis of the Flavor-Tagged Decay $B_s^0 \to J/\psi\phi$*, JHEP **1011** (2010) 158, arXiv:1008.4283.

[138] R. A. Currie, *CP-Violation in Beautiful-Strange Oscillations at LHCb*, PhD thesis, University of Edinburgh, United Kingdom, 2013, CERN-THESIS-2014-104.

[139] M. Williams, *How good are your fits? Unbinned multivariate goodness-of-fit tests in high energy physics*, JINST **5** (2010) P09004, arXiv:1006.3019.

[140] A. Sparkes, *An Angular Analysis and Search for CP Violation in the Decay* $B^0 \to J/\psi K^{*0}$, PhD thesis, University of Edinburgh, United Kingdom, 2012, CERN-THESIS-2012-296.

[141] T. du Pree, *Search for a Strange Phase in Beautiful Oscillations*, PhD thesis, Nikhef, Netherlands, 2010, CERN-THESIS-2010-124.

[142] S. Nandi and A. Kundu, *New physics in* $b \to s\bar{s}s$ *decay: study of* $B \to V_1V_2$ *modes*, J. Phys. **G32** (2006) 835, arXiv:hep-ph/0510245.

[143] Heavy Flavor Averaging Group (HFAG), Y. Amhis *et al.*, *Averages of b-hadron, c-hadron, and* τ*-lepton properties as of summer 2014*, arXiv:1412.7515.

[144] M. Cacciari, M. Greco, and P. Nason, *The* $p_{\rm T}$ *spectrum in heavy flavor hadroproduction*, JHEP **9805** (1998) 007, arXiv:hep-ph/9803400.